Quasi-Free Scattering from Relativistic Neutron-Deficient Carbon Isotopes

Quasifreie Streuung relativistischer neutronenarmer Kohlenstoffisotope

Zur Erlangung des Grades eines Doktors der Naturwissenschaften (Dr. rer. nat.)
vom Fachbereich Physik genehmigte Dissertation von Matthias Holl M.Sc aus Frankfurt am Main
1. Gutachten: Prof. Dr. Joachim Enders
2. Gutachten: Prof. Dr. Thomas Aumann
Tag der Einreichung: 11.02.2014, Tag der Prüfung: 28.04.2014
Darmstadt 2014 — D 17

TECHNISCHE UNIVERSITÄT DARMSTADT

Fachbereich Physik
Institut für Kernphysik

Quasi-Free Scattering from Relativistic Neutron-Deficient Carbon Isotopes
Quasifreie Streuung relativistischer neutronenarmer Kohlenstoffisotope

Vom Fachbereich Physik genehmigte Dissertation von Matthias Holl M.Sc aus Frankfurt am Main

1. Gutachten: Prof. Dr. Joachim Enders
2. Gutachten: Prof. Dr. Thomas Aumann

Tag der Einreichung: 11.02.2014
Tag der Prüfung: 28.04.2014

Darmstadt — D 17

Abstract

Quasi-free scattering of the neutron-deficient carbon isotopes ^{10}C and ^{11}C has been studied in inverse kinematics at the R^{3}B-LAND setup at the GSI-Helmholtz Centre for Heavy Ion Research. In this experiment, a ^{40}Ar primary beam was incident on a beryllium production target at an energy of 490 *A*MeV, and the selected reaction residues were then transported through the fragment separator FRS to the experimental area.

The incoming beam was identified using the time-of-flight and energy loss, and the incoming angle of the beam was determined from the position on two silicon strip detectors in front of the reaction target. The target area was surrounded by the Crystal Ball NaI array used for γ- and proton detection and a box consisting of four silicon strip detectors. After passing through the ALADIN magnet, the outgoing fragments were identified and tracked using the position and energy information given by two additional silicon strip detectors, two fiber detectors, and a time-of-flight wall, and protons emitted in-flight were detected by drift chambers.

In order to obtain the cross section for quasi-free scattering on hydrogen, a CH_2-target and a carbon target were used, and the measurements with the carbon target were used to subtract both the contribution of the carbon and the background in the CH_2-measurements. The cross sections obtained with the carbon target for proton and neutron removal from ^{11}C and for neutron removal from ^{10}C are $\sigma_C = 21.6(8)$ mb, $\sigma_C = 34.8(23)$ mb, and $\sigma_C = 32.8(39)$ mb.

The work presented here is aimed at a quantitative understanding of spectroscopic factors, which appear to be quenched for deeply bound nuclei. The obtained quasi-free scattering cross sections for the reactions ^{11}C(p,2p)^{10}B, ^{11}C(p,pn)^{10}C, and ^{10}C(p,pn)^{9}C are $\sigma_H = 17.3(8)$ mb, $\sigma_H = 21.2(20)$ mb, and $\sigma_H = 19.7(28)$ mb, respectively. The associated quenching of spectroscopic factors, obtained from comparing the experimental cross sections with theoretical ones from DWIA-calculations is $R_s = 0.53(2)$, $R_s = 0.82(8)$, and $R_s = 1,04(15)$.

The momentum distributions for the fragments of all three reactions have been calculated from the measured incoming and outgoing angles and compared to DWIA-calculations. In all three cases there is good agreement between the measured distributions and calculations for a p-shell knockout. The γ-energy spectra measured in coincidence with ^{10}C and ^{10}B produced in quasi-free scattering reactions indicate a strong population of the low-lying excited states in both cases.

The cross section for the reaction ^{11}C(p,pα)^{7}Be has been determined to be $\sigma_H = 5.8(4)$ mb. Due to the small spatial separation of the decay products of the unbound ^{9}B on the silicon detectors and limited acceptance of the proton drift chambers, no reliable cross section could be determined for the reaction ^{10}C(p, 2p)^{9}B.

Furthermore, new front-end electronics for double-sided silicon strip detectors have been developed, and initial tests has been completed. The electronics is based on the combination of commercially available readout and triggering ASICs (VA and TA by Gamma-Medica) and ADC (Struck SIS3300) with a customized sequencing module, based on the VUPROM module developed at GSI. The design is flexible, and it is supposed to be used for DSSD prototype detectors built in connection with the ongoing detector development for nuclear structure experiments at the planned FAIR facility.

Zusammenfassung

Quasifreie Streuung der neutronenarmen Kohlenstoffisotope ^{10}C and ^{11}C wurde am R^{3}B-LAND-Aufbau am GSI-Helmholtzzentrum für Schwerionenforschung in inverser Kinematik untersucht. In dem Experiment traf ein ^{40}Ar-Primärstrahl mit einer Energie von 490 *A*MeV auf ein Beryllium-Produktionstarget und die ausgewählten Redaktionsprodukte wurden anschließend durch den Fragmentseparator FRS zum Experimentierbereich geleitet.

Der einlaufende Strahl wurde mit Hilfe von Flugzeit und Energieverlust identifiziert und der Einlaufwinkel des Strahls wurde aus der Position auf zwei Siliziumstreifendetektoren vor dem Reaktionstarget bestimmt. Der Targetbereich wurde vom Crystal Ball NaI-Array umgeben, welcher für γ- und Protonenmessungen verwendet wurde. Nachdem die Reaktionsfragmente durch das Magnetfeld des ALADIN Dipolmagneten geflogen waren, wurden sie unter Benutzung ihrer Positions- und Energieinformation von zwei weiteren Siliziumstreifendetektoren, zwei Fiberdetektoren und einer Flugzeitwand identifiziert und ihre Flugbahn rekonstruiert. Im Flug emittierte Protonen konnten mit Hilfe von Driftkammern gemessen werden.

Um den Wirkungsquerschnitt für quasifreie Streuung an Kohlenstoff zu bestimmen, wurden ein CH_2- und ein Kohlenstofftarget benutzt und die Messungen mit Kohlenstoff verwendet um sowohl den Kohlenstoffbeitrag als auch den Untergrund der CH_2-Messungen abzuziehen. Die Wirkungsquerschnitte mit Kohlenstofftarget für die Entfernung eines Protons bzw. Neutrons aus ^{11}C sowie eines Neutrons aus ^{10}C sind $\sigma_C = 21.6(8)$ mb, $\sigma_C = 34.8(23)$ mb und $\sigma_C = 32.8(39)$ mb.

Die hier vorgelegte Arbeit zielt auf ein qunatitatives Verständnis von spektroskopischen Faktoren ab, die bei stark gebundenen Kernen unterdrückt zu sein scheinen. Die erhaltenen Wirkungsquerschnitte für die Reaktioen ^{11}C(p,2p)^{10}B, ^{11}C(p,pn)^{10}C und ^{10}C(p,pn)^{9}C sind $\sigma_H = 17.3(8)$ mb, $\sigma_H = 21.2(20)$ mb und $\sigma_H = 19.7(28)$ mb. Die Unterdrückung der spektroskopischen Faktoren, die man aus dem Vergleich dieser Werte mit theoretischen, in DWIA errechneten Wirkungsquerschnitten erhält ist $R_s = 0.53(2)$, $R_s = 0.82(8)$ bzw. $R_s = 1,04(15)$.

Die Impulsverteilung der aus allen drei Reaktionen resultierenden Fragmenten wurden aus den einlaufenden und ausgehenden Winkeln berechnet und mit theoretischen Verteilungen aus DWIA-Rechnungen verglichen. In allen drei Fällen zeigen die gemessenen Verteilungen gute Übereinstimmungen mit Rechnungen für den Knockout eines Nukleons aus der p-Schale. Die in Koinzidenz mit in quasifreier Streuung produziertem ^{10}C and ^{10}B gemessenen γ-Energiespektren weisen auf eine starke Bevölkerung der niedrig liegenden angeregten Zustände hin.

Der gemessene Wirkungsquerschnitt für ^{11}C(p,pα)^{7}Be beträgt $\sigma_H = 5.8(4)$ mb. Aufgrund der geringen räumlichen Trennung der Zerfallsprodukte von ^{9}B auf den Siliziumstreifendetektoren und der beschränkten Akzeptanz der Protonendriftkammern konnte kein verlässlicher Wirkungsquerschnitt für die Reaktion ^{10}C(p, 2p)^{9}B bestimmt werden.

Weiterhin wurde eine neue Frontendelektronik für Siliziumstreifendetektoren entwickelt und erstmals getestet. Die Elektronik basiert auf der Kombination von kommerziell erhältlichen Auslese- und Trigger-ASICs (Typ VA und TA von Gamma-Medica) und ADC (Struck SIS3300) mit einem speziell angepassten Sequencermodul, basierend auf dem an der GSI entwickelten VUPROM. Das Design wurde flexibel gehalten, da die Elektronik für DSSD-Prototypen verwendet werden soll, die im Zusammenhang mit der Detektorentwicklung für die Kernstrukturexperimente an der geplanten FAIR-Anlage gebaut werden.

Contents

1 Introduction

Even over one hundred years after the discovery of the atomic nucleus, a microscopic theory of its structure based on the properties of the nuclear forces is still missing. The reasons for that are the complicated nature of the nuclear force and the fact that the nuclei are many-body problems, making ab-initio calculations very complex and simplifications for all but the lightest nuclei inevitable. There are two major groups of simplified models, collective and independent particle models.

In its simplest form, the nuclear shell model, developed in the late 1940s by Goeppert-Mayer and Jensen [1, 2], is an example of an independent particle model. The nucleons are assumed to move independently in the nuclear potential, consisting of a mean-field potential and a strong spin-orbit force. While this seems counter-intuitive for a collection of strongly interacting particles, it can be undertood using Pauli's exclusion principle.

The main experimental evidence for such a nuclear structure is the existence of the so-called magic numbers, i.e. nuclei with a proton or neutron number $N, Z = 2, 8, 20, 28, 50, 82, 126$ have been shown to be especially stable. Within the shell model, these magic numbers can be explained as fully occupied shells for either protons or neutrons. Also in this picture, every nucleus can be described as a combination of an inert core with closed shells, and a small number valence nucleons outside this core, mainly responsible for the characteristics of the nucleus.

Several modifications to this simple model have been made, e.g. including both residual interactions between the valence nucleons and excitations of the closed-shell core in the description. However, the comparison of theoretical shell occuppancies and experimentally observed spectroscopic strength still yields a mismatch which can be quantified by the "quenching" of a spectroscopic factor [3].

Much of the experimental data addressing this has been obtained using electron induced quasi-free scattering (e,e'p) [4]. Electron induced reactions have the advantage of high accuracy and little model dependence but suffer from low cross sections, due to the fact that the electrons interact with the nuclear matter only via the electromagnetic interaction[5]. One of the main results of these experiments is that the observed spectroscopic factor is on average reduced to 60-70% compared to shell model calculations[4].

Using the fragmentation of relativistic radioactive beams has allowed to extend the study of nuclear structure to exotic nuclei far off the valley of β-stability. However, without a electron collider available at present or in the near future [6], it is impossible to use electron scattering for the study of exotic nuclei. Instead, over the past two decades, knockout reactions using light nuclear targets (beryllium, carbon) have been developed into a powerful tool for studying the structure of exotic nuclei. Results from such experiments confirm the finding for the quenching of spectroscopic factors and in addition suggest a dependence of this quenching on the difference in binding energy between the

two types of nucleons [7]. However, recently the ability of knockout reactions using beryllium or carbon targets to obtain spectroscopic factors has been called into question due to the surface localization of these reactions. In addition, recent results from transfer reaction experiments do not observe a this dependence [8] and modern ab-initio calculations predict a less pronounced dependence [9].

To overcome this problem, the application of quasi-free proton scattering to exotic nuclei has been proposed. For stable nuclei, the development of quasi-free proton (p,2p) and electron (e,e'p) scattering has gone largely in parallel and their results have been complementary [5, 10]. Especially for the studies of deeply bound nuclear states, the possibilities offered by quasi-free scattering (QFS) are nearly unique. The lower accuracy of (p,2p) due to the larger distortion in the nuclear medium is partially offset by their much higher cross sections and the possibility of the study of neutron knockout [5].

At GSI, such studies can be done at the R^3B-LAND setup [11] which is capable of measuring both knockout and quasi-free reactions in kinematically complete measurements. An experiment studying, among other topics, the quasi-free scattering of light nuclei from one dripline to the other has been carried out in August 2010. The work presented here focuses on QFS of two carbon isotopes, the neutron-deficient ^{10}C and ^{11}C.

For several reasons, these two nuclei are good candidates to study single-particle properties of nuclei. They are light, making them accessible to ab-initio calculations. Also, while being direct neighbours in the nuclide chart, they show very different degrees of nuclear binding energy asymmetry. Finally, they have a relatively simple structure within the shell-model, while being candidates for more exotic structures such as α-cluster states as well.

Furthermore a benchmark experiment R^3B-LAND setup investigating the quasi-free scattering of the neighbouring stable isotope ^{12}C has been performed recently [12], and its results agree well with results of QFS in direct kinematics [13]. Comparing spectroscopic factors of the stable ^{12}C with the ones of the neutron-deficient carbon isotopes can provide further insight into the development of spectroscopic factors away from stability.

The main part of this work will be concerned with the analysis of this experiment. It will be organized as follows: In Chapter 2 the theoretical concepts will be briefly explained. In chapter 3 the experimental apparatus used will be described. The Chapters 4 and 5 will outline the calibration of the detectors introduced in Chapter 3 and introduce the concepts used in the analysis. The results of this analysis will then be presented and discussed in Chapter 6.

The study of quasi-free scattering will also be one of the main pillars of the nuclear structure experiments at the planned FAIR facilities [11]. At the moment, detector development for these experiments is ongoing and the first detector protoytpes are ready to be tested. This creates also a demand for new detector electronics. Not only for the final detectors have these to be developed, but also for the prototypes in various development phases. Chapter 7 will deal with the development of testing of new frontend electronics for double-sided silicon strip detectors.

2 Theoretical Background

2.1 The Independent Particle Model

The nuclear potential each nucleon experiences is due to its interactions with all other nucleons in the nucleus. Because of the short range of nuclear forces, it resembles the nuclear density distribution ρ and has the form

$$V(x_1) = V_0 \int d^3x_2 f(x_1 - x_2)\rho(x_2), \tag{2.1}$$

where V_0 is the central depth of the potential and f describes its shape. Assuming that f is sufficiently short-ranged, Eq. (2.1) can be simplified to

$$V(x_1) = V_0\rho(x_1) \int d^3x f(x). \tag{2.2}$$

Often the form of a Fermi distribution is used for f, leading to the spherically symmetric Woods-Saxon potential

$$V(r) = \frac{-V_0}{1 + \exp[\frac{r-R}{a}]}. \tag{2.3}$$

The two parameters of this potential R and a are the radius at which it has half the value of its central depth and its diffuseness. However, such a potential can only recreate the first few shell closures. To arrive at a correct description, the spin-orbit interaction has to be taken into account. A nucleon with angular momentum l and spin s will experience an additional potential

$$V_{LS} = C_{LS}(r) l \cdot s \tag{2.4}$$

which will lead to an energy splitting

$$\Delta E_{LS} = \left(l + \frac{1}{2}\right)\hbar^2 C_{LS}(r). \tag{2.5}$$

With a sufficiently large $C_{LS}(r)$ this leads to a considerable regrouping of the nuclear shells, which is shown in Fig. 2.1.

This simple model can well describe nuclei in vicinity of closed shells. To generalize to nuclei further away from the closed shells, several refinements are made. The two main simplifications, the independence of the particles and the spherical shape of the potential can be treated by including the residual

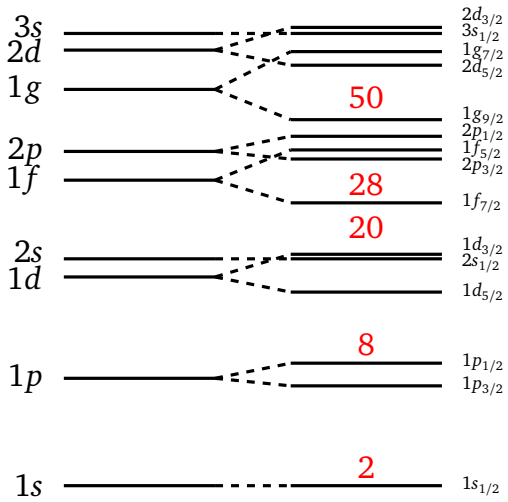

Figure 2.1: The energy splitting due to the spin-orbit interaction of the nucleons leads to a considerable regrouping of the nuclear shells, and therefore to the emergence of the magic numbers.

interaction between valence nucleons and deformation. In addition core excitations will play a role for excitation energies larger than 2 MeV.

2.2 Deviations from the IPM and Quenching of Spectroscopic Strength

The model presented in the previous section assumes the nucleons to move independently from one another inside the nucleus. However, both long- and short-range residual interactions between nucleons play an important role in the structure of nuclei modifying the occupancies of nuclear shells, especially close to the Fermi surface and leading to partially occupied orbits [9]. These correlations manifest themselves as a reduction of experimental cross sections obtained compared to theoretical calculations made under the assumption of fully occupied orbits. E.g. in (e,e'p) reactions on stable isotopes, a reduction to 60-70 % of the independent particle model value was found [4].

As a measure of these deviations, the overlap between the wavefunction of the initial and final state of a nuclear reaction can be used. In the case of the removal of a single nucleon from a nucleus with A nucleons this can be written as

$$\langle \Psi_{A-1}(\vec{r}) | \Psi_A(\vec{r}) \rangle = \sum_{j=I_A-I_{A-1}}^{I_A+I_{A-1}} c_j \psi_j(\vec{r}) \tag{2.6}$$

in terms of an expansion in single-particle states ψ_j with I_A, I_{A-1} being the angular momentum of the initial and residual nucleus, respectively. With the single-particle states normalized to unity, a spectroscopic factor is $S_j = |c_j|^2$ can be defined. In the isospin representation, the spectroscopic factor is often written as C^2S, C^2 being the square of the isospin coupling coefficient.

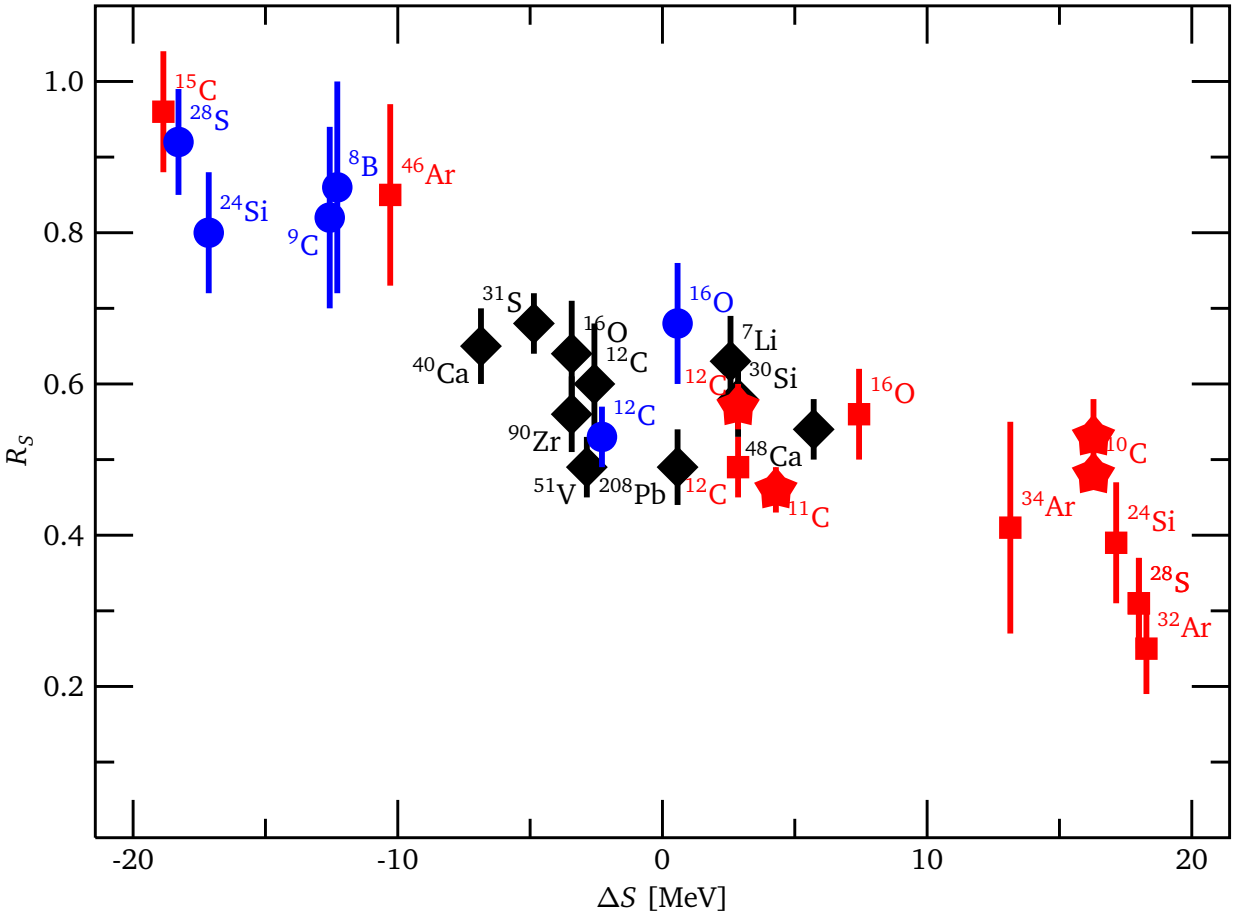

Figure 2.2: Reduction of spectroscopic factors as a function of the difference in nucleon binding energy ΔS. Shown are results for electron scattering (black diamonds), proton-knockout (blue circles), and neutron-knockout(red squares). The energy difference is $\Delta S = S_n - S_p$ for the removal of a neutron, and $\Delta S = S_p - S_n$ for the removal of a proton. Data for the neutron removal from ^{10,11}C (red stars) [14, 15] has been added to the results presented in Ref. [7]. One can see a dependency of R_S on ΔS [7].

Using the spectroscopic factor, the reaction cross section can be written in the factorised form

$$\sigma_{th} = \sum_j S_j \cdot \sigma_{sp}(nlj) \tag{2.7}$$

with the single-particle cross section $\sigma_{sp}(nlj)$. Equation (2.24) gives an example of a possible single-particle cross section.

Knockout reactions done in inverse kinematics with relativistic beams at intermediate energies have made it possible to expand the studies of this quenching to exotic nuclei [3, 7, 16]. It has also been argued that knockout reactions allow extracting spectroscopic factors on an absolute scale [17]. Figure 2.2 shows the reduction factor

$$R_S = \frac{\sigma_{exp}}{\sigma_{th}} = \frac{C^2 S_{exp}}{C^2 S_{th}} \tag{2.8}$$

plotted as a function of the difference in nucleon binding energy ΔS, i.e. in case of the removal of a neutron $\Delta S = S_n - S_p$, while for the removal of a proton $\Delta S = S_p - S_n$. The results obtained for electron scattering on stable isotopes has been combined with the ones obtained in nuclear knockout. The data has been taken from Gade et al. [7]. One can see a dependency of the quenching on ΔS [7].

The reason for this apparent dependency of the quenching on A/Z is an area of debate. The trend was not observed in several transfer reaction experiments [8], where the comparison of experimental and theroretical angular distributions calculated using the ADWA* model yielded almost constant reduction factors. Ab-initio calculations, which include short-range and partially also long-range correlations, give smaller spectroscopic factors than obtained in a classic shell model and also show some dependance on nuclear asymmetry, however it is not as pronounced as experimentally observed [9, 14]. Timofeyuk et al. have attributed quenching to a shortcoming of the shell-model descriptions, namely the truncation of the model space [18].

Due to their surface localization, the ability of knockout reactions to deduce spectroscopic factors has been called into question and it has been proposed that ANCs† are a better suited for the comparison to experimental data from knockout reactions [19]. In contrast to the spectroscopic factors, the ANCs are defined as the norm not of the entire overlap function, but only its tail, which will dominate in surface-peaked reactions.

2.3 Quasi-Free Scattering

In quasi-free scattering reactions, a proton of a typical energy of several hundred MeV is incident on a nucleus. At these energies, the de-Broglie wavelength $\lambda_{dB} = h/p$ becomes smaller than the average distance between two nucleons in the nucleus (≈ 2 fm). In this case, in a crude approximation, one can view each nucleon-nucleus collision as a series of independent nucleon-nucleon collisions. In this picture, quasi-free scattering corresponds to the case in which exactly one nucleon-nucleon collision occurs. The remaining nucleus is then not involved in the reaction, and the two particles interact as if they were free, therefore the name. Because the mean free path of a nucleon at these energies is comparable to the radius of a nucleus, such reactions are reasonably probable [5]. The two particles are then measured as a coincident, correlated pair.

Figure 2.3 shows a simplified schematic of a quasi-free scattering event. A proton with kinetic energy T_p and momentum $\vec{p}_p$ is incident on a nucleon which is bound in a nucleus. The nucleus is at rest, and the nucleon is moving inside the nucleus with kinetic energy T_N and momentum $\vec{p}_N$. After the collision both the scattered proton and the knocked-out nucleon leave the nucleus with kinetic energy $T_{p'}$, $T_{N'}$ and momentum $\vec{p}_{p'}$, $\vec{p}_{N'}$. The remaining nucleus receives a recoil momentum $\vec{p}_{A-1} = -\vec{p}_N$. Momentum conservation then gives

* Adiabatic Distorted Wave Approximation
† Asymptotic Normalization Coefficients

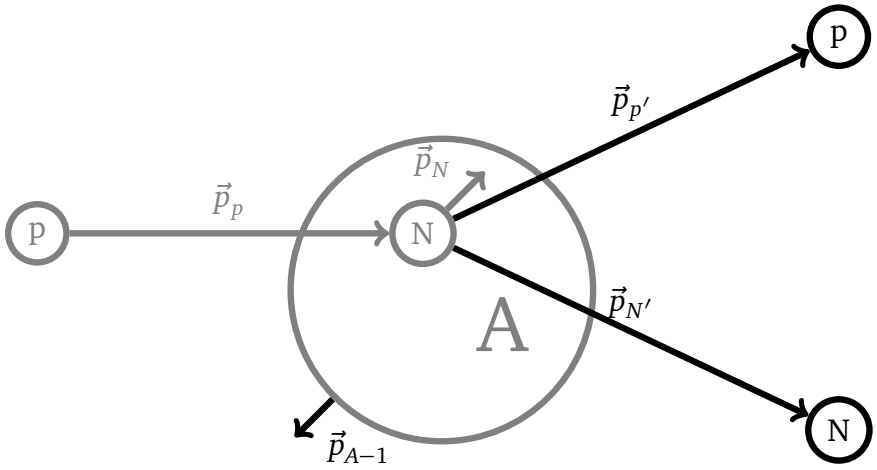

Figure 2.3: Schematic of a QFS reaction. The particles and their momenta before pN-collision are shown in grey, the ones after the collision in black. A proton with momentum $\vec{p}_p$ is incident on a nucleon which is bound in a nucleus at rest and moving inside the nucleus with momentum $\vec{p}_N$. After the collision both the scattered nucleons leave the nucleus with momentum $\vec{p}_{p'}$, $\vec{p}_{N'}$. The remaining nucleus receives a recoil momentum $\vec{p}_{A-1} = -\vec{p}_N$.

$$\vec{p}_p = \vec{p}_{p'} + \vec{p}_{N'} + \vec{p}_{A-1} \tag{2.9}$$

and energy conservation

$$E_p + M_A c^2 = E_{p'} + E_{N'} + E_{A-1} \tag{2.10}$$

From Eq. (2.10) one can calculate the binding energy of the removed nucleon as

$$B_N = S_N + E^*_{A-1} = T_p - \left(T_{p'} + T_{N'} + T_{A-1}\right) \tag{2.11}$$

Here, S_N is the binding energy of the least bound nucleon, and E^*_{A-1} is the excitation energy of the residual nucleus. This excitation energy greatly influences the outcome of the reaction. While for $E^*_{A-1} < S_N$ the nucleus will deexcite via γ-emission, in the case of $E^*_{A-1} > S_N$ a breakup of the residual nucleus is more likely.

Of course, the description of the reaction just presented is greatly simplified. Several modifications have to be taken into account to arrive at a correct description. Especially, the fact that the nucleons can undergo multiple collisions has to be taken into account. Even at energies of ≈ 400 MeV, where the nucleon-nucleon cross section has its minimum, such multiple collisions will not be negligible and cause an increase in background.

A commonly used theoretical framework for the description of quasi-free scattering is the distorted wave impulse approximation (DWIA) [20, 21]. In this approximation it is assumed, as in the previous section, that the quasi-free reaction is mainly due to a single interaction between the incident

and the knocked-out nucleon. Interaction with the surrounding medium, like multiple scattering or absorption due to excitation to other channels, are incorporated by using distorted waves to describe the wave functions of the incoming proton and scattered nucleons. These distorted waves are calculated from a complex mean nuclear potential and absorption effects are introduced by the imaginary part of this potential. In this section, a rough outline of the application of DWIA to quasi-free scattering is given, also including eikonal reaction theory. For a more detailed derivation and discussion of the formulas, see reference [22].

The general expression for the DWIA cross section is

$$\frac{d^3\sigma}{dT_N d\Omega'_p d\Omega_N} = K \frac{d\sigma_{pN}}{d\Omega} |F(Q)|^2 . \tag{2.12}$$

Here, $K \equiv K(k_p, k'_p, k_n, \theta_p, \theta_N)$ is a kinematic factor, depending on the momenta and angles of the nucleons and $F(Q)$ is the momentum transfer distribution. The differential quasifree pN cross section $\frac{d\sigma_{pN}}{d\Omega}$ is proportional to square the scattering matrix element $\left|\tau_{pN}\right|^2$, and is therefore conncected to the transition amplitude $T_{p,pN}$ via

$$T_{p,pN} = \sqrt{S(lj)} \left\langle \chi^{A-1}_{k'_p} \chi^{A-1}_{k_N} | \tau_{pN} | \chi^{A}_{k_p} \psi_{jlm} \right\rangle . \tag{2.13}$$

In this formula, ψ_{jlm} is the bound-state wave-function of the knocked-out nucleon and $\sqrt{S_{lj}}$ is the corresponding spectroscopic amplitude. The symbol $\chi^{(A)}_{k_p}$ denotes the wave function of the incoming proton, distorted by the potential of the A-nucleon nucleus before the knockout, and $\chi^{A-1}_{k'_p}$, and $\chi^{A-1}_{k_N}$ are the distorted wavefunctions of the scattered nucleons in presence of the $(A-1)$-nucleon nucleus after the reaction.

Using Eq. (2.13), one can show one important feature of quasi-free scattering cross sections by looking at the idealised situation described above which can be described in plane-wave impulse approximation (PWIA). Here, as in the example above, the assumption is that the nucleon-nucleon collision is the only violent interaction, and that otherwise the wavefunctions of the nucleons remains unaffected. One can then replace the distorted waves in Eq. (2.13) by plane waves and arrives at

$$T^{PWIA}_{p,pN} = \sqrt{S(lj)} \tau(k'_{pN}, k_{pN}; E) \int d^3 r e^{-iQr} \psi_{jlm(r)} \tag{2.14}$$

in which Q is the momentum transferred from the nucleus to the observed nucleons, corrected for the center-of-mass motion

$$Q = k'_p + k_N - \frac{A-1}{A} k_p . \tag{2.15}$$

Equation (2.14) shows that, at least in this approximation, the cross section of the quasifree reaction is proportional to the momentum distribution of the nucleons inside the target, a property which is also seen and exploited in other kinds of reactions, e.g. nuclear knockout reactions [3].

To arrive at a realistic description, however, the PWIA is not sufficient, since distortions and absorption due to interaction with nuclear matter have to be taken into account. To do so, DWIA is more suitable. It can be combined with the eikonal approximation, i.e. assuming that all involved particles fly straight paths between collisions, a assumption well justified for high-energy collisions. In this case, the plane waves used in PWIA get replaced by the distorted waves

$$\chi_i(r)^{in(out)} = \mathcal{S}_{in(out)}(b) e^{ik_i^{in(out)} r} \tag{2.16}$$

with the survival amplitude for the incoming and outgoing waves

$$\mathcal{S}_{in(out)}(b) = \exp\left[-\frac{i}{\hbar v}\int_{-\infty(b)}^{b(\infty)} dz' U_i^{in(out)}(r')\right]. \tag{2.17}$$

The effects of distortions and absorption are included in $\mathcal{S}$ by an appropriate optical potential $U_i^{in(out)}$. With these wave functions, the transition amplitude becomes

$$T_{p,pN}^{eikonal} = \sqrt{S(lj)}\tau(k'_{pN}, k_{pN}; E)\int d^3 r e^{-iQr}\mathcal{S}(b, \theta'_p, \theta_N)\psi_{jlm(r)} \tag{2.18}$$

where the shorthand

$$\mathcal{S}(b,\theta) = \mathcal{S}_{pA}(E_p, b)\mathcal{S}_{pA-1}(E_p, \theta_p, b)\mathcal{S}_{NA-1}(E_N, \theta_N, b) \tag{2.19}$$

has been used. On this basis, theoretical cross sections and momentum distributions can be derived. These derivations can be found in reference [22] and will not be given here, only the final results, used for comparison with the experimental data in Chapter 6 shall be listed in the following. In all of them the form

$$\psi_{jlm} = \frac{u_{lj}(r)}{r}\sum_{m_l, m_s}\langle l m_l s m_s | jm\rangle\, Y_{lm_l}(\hat{r})\chi_{m_s} \tag{2.20}$$

is used for the bound-state wave functions, where u_{lj} are the radial wavefunctions, which are calculated using a Woods-Saxon potential, $\langle l m_l s m_s | jm\rangle$ are the Clebsch-Gordan coefficients, and χ_{m_s} the spinors. $Y_{lm_l} = C_{lm}P_{lm}(b,z)e^{im\varphi}$ are the spherical harmonics, consisting of the associated Legendre polynomials $P_{lm}(\cos\vartheta) \equiv P_{lm}(b,z)$ and a normalization factor C_{lm}.

The total momentum distribution then becomes

$$\frac{d\sigma}{Q^2 dQ} = \frac{2}{\pi}\frac{S(lj)}{2j+1}\left\langle\frac{d\sigma_{pN}}{d\Omega}\right\rangle_Q \times \left|\int_0^\infty dr\, r\,\langle\mathcal{S}(r)\rangle_Q\, j_l(r) u_{lj}(r)\right|^2 . \tag{2.21}$$

$j_l(r)$ is the radial Bessel function. The differential cross section $\left\langle d\sigma_{pN}/d\Omega\right\rangle_Q$ has been averaged over all energies leading to a momentum transfer Q. A similar averaging has been done for $\langle\mathcal{S}(r)\rangle_Q$ for all angles leading to Q. Integration yields the longitudinal and transverse momentum distributions

$$\begin{aligned}\frac{d\sigma}{dQ_z} &= \frac{S(lj)}{2j+1}\sum_m\left\langle\frac{d\sigma_{pN}}{d\Omega}\right\rangle_{Q_z}|C_{lm}|^2 \\ &\times \int_0^\infty db\, b\left|\langle\mathcal{S}(b)\rangle_{Q_z}\right| \times \left|\int_{-\infty}^\infty dz e^{-iQ_z z}\frac{u_{lj}(r)}{r}P_{lm}(b,z)\right|^2 \qquad (2.22)\\ \frac{d\sigma}{Q_t dQ_t} &= \frac{S(lj)}{2j+1}\sum_m\left\langle\frac{d\sigma_{pN}}{d\Omega}\right\rangle_{Q_t}|C_{lm}|^2 \\ &\times \int_{-\infty}^\infty dz\left|\int_0^\infty db\,\langle\mathcal{S}(b)\rangle_{Q_t}\frac{u_{lj}(r)}{r}J_m(Q_t b)P_{lm}(b,z)\right|^2 . \qquad (2.23)\end{aligned}$$

In the transverse distribution, the Bessel function $J_m(Q_t b)$ is used. Finally, integrating either one of these distributions gives the total cross section

$$\sigma = 2\pi\frac{S(lj)}{2j+1}\sum_m\left\langle\frac{d\sigma_{pN}}{d\Omega}\right\rangle|C_{lm}|^2 \times \int_0^\infty db\, b\,|\langle\mathcal{S}(b)\rangle|^2\int_{-\infty}^\infty dz\left|\frac{u_{lj}(r)}{r}P_{lm}(b,z)\right|^2 \tag{2.24}$$

Using these calculations, it possible to illustrate the advantage of quasi-free scattering over knockout reactions using compound targets for probing the nuclear interior. This is shown in Figure 2.4 [22]. The removal probability for a nucleon is shown as a function of the distance from the center of mass of the nucleus for three different nuclei, ^{68}Ni, ^{11}Be, and ^{8}B. For each nucleus, the probability for a nucleon knockout using a carbon target at 500 AMeV (dashed line) and the removal probaibility in a QFS reaction with a proton target at the same energy (dotted line) are compared. Also shown in each case is the square of the radial part of the wavefunction $u(r)$. Especially for the lighter nuclei, the QFS reaction is able to probe the entire wave function of the nucleus, in contrast to the knockout with a compound target.

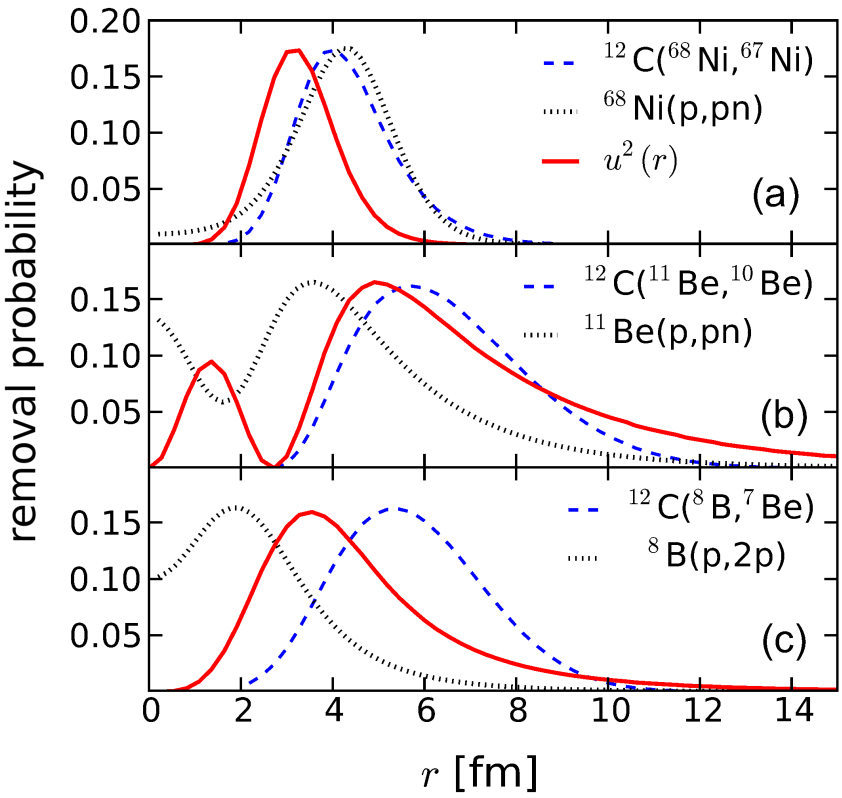

Figure 2.4: Comparison QFS and knockout [22].The removal probability for a nucleon is shown as a function of the distance from the center of mass of the nucleus for three different nuclei, ^{68}Ni, ^{11}Be, and ^{8}B. For each nucleus, the probability for a nucleon knockout using a carbon target at 500 AMeV (dashed line) and the removal probaibility in a QFS reaction with a proton target at the same energy (dotted line) are compared. Also shown in each case is the square of the radial part of the wavefunction $u(r)$. Especially for the lighter nuclei, the QFS reaction is able to probe the entire wave function of the nucleus, in contrast to the knockout with a compound target. Copyright ©2013 by the American Physical Society.

2.4 α-Clustering in Nuclei

One of the most notable deviations from the shell-model picture is the appearance of α-cluster states. While the existence of cluster states emerges from the existence of a mean-field, they can not be reproduced using the shell model [23, 24]. Although the phenomenon was first observed in even-even $N = Z$-nuclei (^{12}C,^{16}O), it became apparent that also other light nuclei (^{9}Be) have states which can be best described as several α-clusters and a small number of valence nucleons. Due to the similarites of such a system to the exchange of electrons between atoms in molecules, such states are also called nuclear molecules, and the valence nucleons can be seen as occupying molecular orbits in a multi-center system.

Two theoretical models frequently used for the description of cluster states are AMD* and FMD†. Both models are ab-initio models giving them e.g. the advantage that they use nucleons as degrees of

* Antisymmetrized Molecular Dynamics
† Fermionic Molecular Dynamics

freedom and do not presume the existence of clusters. This makes them suitable for the description of both cluster and shell-model states. In AMD [25], the nucleus is described as a A-nucleon wave-function, antisymmetrized via a Slater determinant of Gaussian wave packets φ_i,

$$\Phi(Z) = \frac{1}{\sqrt{A!}}\mathcal{A}(\varphi_1, \varphi_2, ...\varphi_A), \tag{2.25}$$

which is parametrized using the complex parameter Z. The energy of the system is then calculated by minimizing

$$E = \frac{\langle\Phi(Z)|H|\Phi(Z)\rangle}{\langle\Phi(Z)|\Phi(Z)\rangle}, \tag{2.26}$$

using an effective interaction. The approach in FMD is similar, however it uses the width of the Gaussians as an additional parameter making it more suitable to describe shell-model states as well [26].

One of the most important cluster states is the so-called Hoyle-state, the 0^+ excited state of ^{12}C, found at 7.65 MeV [24]. Its importance comes from its role in the creation of ^{12}C in stars, which is believed to happen via α-capture of the short-lived ^{8}Be. Even modern shell-model calculations (e.g. NCSM*) with large model spaces fail to describe its occurence, however AMD and FMD are able to do so and also predict its strong cluster characteristics. While initially predicited to have a chain-line structure, this can be excluded due to its 0^+ spin. The Hoyle-state has also gathered interest due to the possibility that it constitutes a Bose-Einstein condensate of α-particles, however, data from elastic electron scattering analyzed using FMD, shows that a configuration close to ^{8}Be+α is more likely [27].

A lot of the studies of nuclear molecules and their development with different neutron-proton asymmetry is done using beryllium isotopes, which can be described as two-center molecules with valence neutrons. The valence neutrons can occupy one of two orbits, the σ-orbit, asscociated with the sd-shell or the π-orbit. In case of the σ-orbit, the nucleons will lie between the two α-clusters, while in the case of the π-orbit they lie around them. The $N = Z$-nucleus ^{8}Be is unbound, however, the addition of a valence neutron in ^{9}Be leads to a bound nucleus. The valence neutron is found to mainly occupy the σ-orbit.

The next isotope in the chain ^{10}Be shows only weakly pronounced cluster-state characteristics in the ground state. However, around $E^* = 6$ MeV, close to the α-decay threshold, these become more dominant, similar to the occurence of the Hoyle-state in ^{12}C. There are for excited states in that region, which, using AMD, have been shown to have either σ^2 or $\sigma\pi$ characteristics.

Evidence for clustering has also been found in heavier Beryllium isotopes ($^{11-14}$Be). The trend has been observed that clustering is more pronounced in states with a large number of neutrons in the (sd)-shell. This can be understood due to the associaton of the (sd)-shell with the σ-orbit, i.e. neutrons between the two α-clusters, driving them apart due to the Pauli-principle. In contrast, states with a

* No-Core Shell Model

Table 2.1: Results of Knockout Experiments [14, 15]

Reaction	facility	E[AMeV]	σ [mb]	R_S
^{9}Be(^{12}C,^{11}C)X	GSI	1670	56±3	0.57(3)
^{9}Be(^{11}C,^{10}C)X	GSI	1670	25±2	0.46(3)
^{9}Be(^{10}C,^{9}C)X	GSI	1670	21±2	0.53(5)
^{9}Be(^{10}C,^{9}C)X	MSU	120	23±1	0.48(2)

large number of p-shell neutrons push the two clusters together, thereby causing a more spherical and shell-model-like structure.

The cluster-structure of neutron-deficient carbon-isotopes as a system of two α-clusters and valence nucleons has been less studied. Only recently, the existence of 2α+^{3}He(t)-cluster-states in highly excited states of ^{11}C and its mirror nucles ^{11}B has been suggested [28], marking the possibility of a triangular configuration as well as a linear one or a dilute gas-like state. Measuring the α-knockout probability in QFS may provide insight into the existence of a pre-formed α-particle inside the light carbon isotopes.

2.5 Previous Measurements

The experimental data for the study of carbon isotopes is vast, especially for the stable isotope ^{12}C. The neutron-deficient isotopes have also been studied on numerous occasions. No attempt will be made to give a broad overview over the results of these studies in this section. Instead, the results of a few experiments especially close to the one presented in this work will be highlighted.

An experiment studying the quenching of spectroscopic strength in $^{9-12}$C was carried out at the FRS* at GSI in 2008. The primary beam provided by the SIS consisted of ^{12}C at 1670 AMeV. Depending on the isotope to be studied it was either directly transported to the experimental area, located at focus S2 of the FRS, or or used to produce a secondary particle beam with beryllium production target. Incoming and outgiong particles were identified event-by-event using their charge and magnetic rigidity. The analysis is still ongoing, but preliminary cross sections and the corresponding reduction factors are given in Table 2.1 [15].

One of these reactions,^{9}Be(^{10}C,^{9}C)X has also been studied at MSU†, albeit at much lower energies of 120 AMeV. The ^{10}C beam was produced at the NSCL's‡ Coupled Cyclotron Facility through the fragmentation of a ^{16}O primary beam. The secondary beam was then separated and delivered to the experimental area by the A1900 fragment separator where it impinged on a ^{9}Be-target. Similar to the GSI experiment, the reaction products were identified using their charge and magnetic rigidity. The results of this experiment are also given in Tab. 2.1. Despite the very different beam energies of the two experiments, the cross sections agree very well. The reduction factors obtained in both experiments have also been included in Fig. 2.2, and seem to confirm the trend described by Gade et al. [7].

* FRagment Separator
† Michigan State University
‡ National Superconducting Laboratory

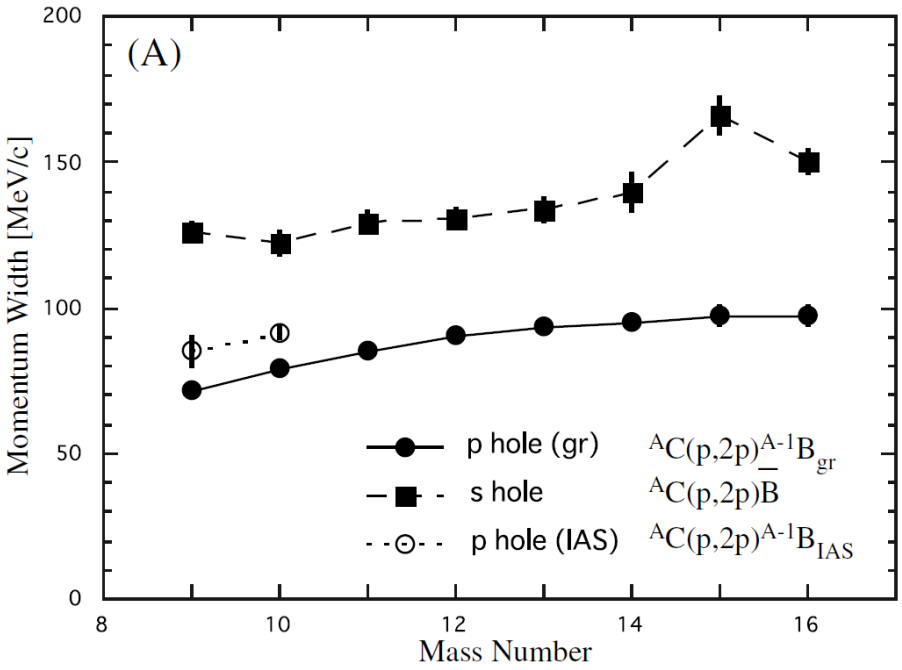

Figure 2.5: Momentum widths obtained by Kobayashi et al. [29]. A harmonic oscillator function was fitted tothe experimental momentum distributions. The occurence of a (p,2p)-event without the observation of a boron fragment was used as a signature of a s-shell knockout. Copyright ©2008 by Elsevier B.V.

So far, two experiments have employed quasi-free scattering in inverse kinematics to carbon nuclei. One of these experiments [29] was performed at the HIMAC* accelerator facility at the NIRS† in Japan. Primary ^{12}C and ^{18}O beams were accelerated to 350-400 *A*MeV and impinged on a Be production target. The secondary beams of ^{916}C at 250 *A*MeV were separated, and focused onto a solid-hydrogen reaction target. In addition to detecting and identifying the fragments produced in the (p,2p) reaction using a forward spectrometer, consisting of a dipole magnet , three sets of drift chambers for tracking, and plastic scintillator hodoscope, the two protons from the (p,2p) reaction were detected by two proton telescopes. The proton telescopes consisted of plastic scintillators for energy-loss, drift chambers for tracking, and NaI(Tl) for the total-energy measurement.

Proton separation energies S_p and the momenta of the knocked out proton were calculated from the measured four-momenta for knockout from both the p- and the s-shell. The occurence of a (p,2p)-event without the observation of a boron fragment was used as the signature of a s-shell knockout. Figure 2.5 shows the obtained momentum widths, calculated using harmonic oscillator wave functions, as a function of the mass number.

A benchmark experiment for quasi-free scattering in inverse kinematics at the R^{3}B-LAND setup was carried out in 2007. ^{12}C was chosen for this purpose, since its structure is well known and data from both electron scattering and proton knockout in normal kinematics is available. The used setup was very

* Heavy Ion Medical Accelerator in Chiba
† National Institute of Radiological Sciences

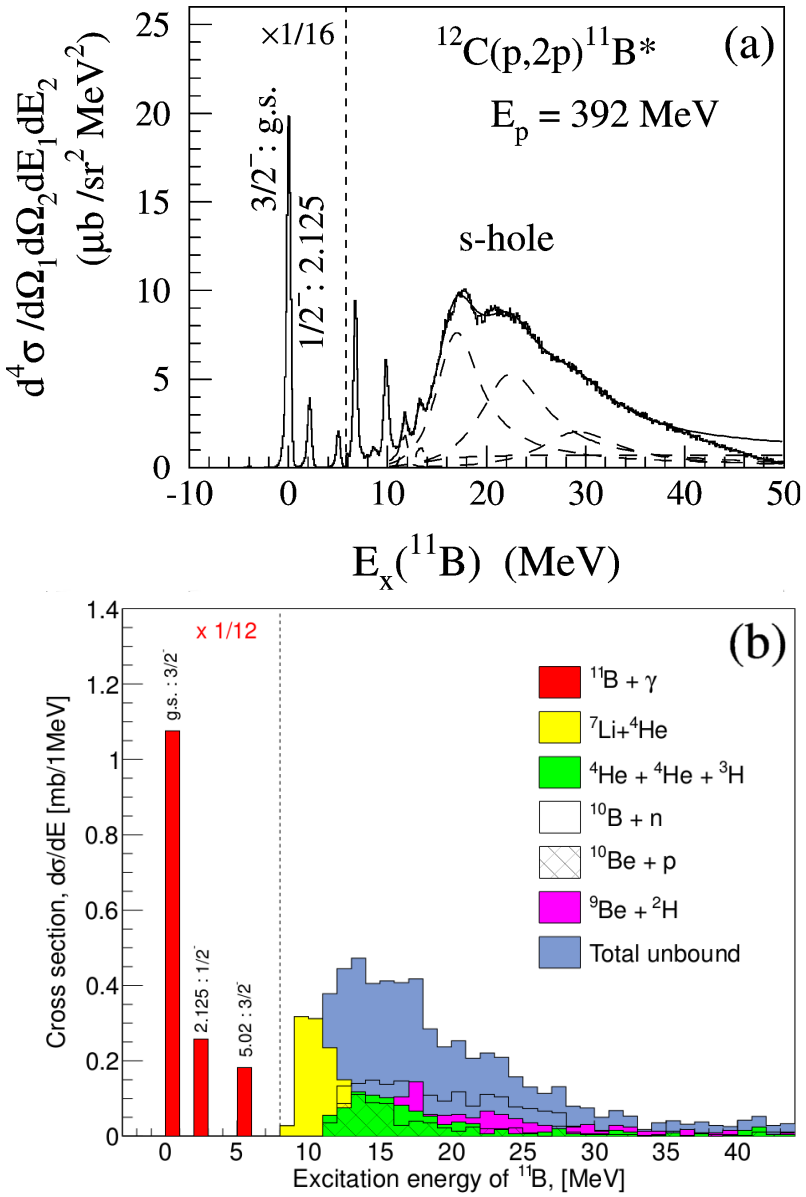

Figure 2.6: Exctitation spectrum of ^{11}B, after the reaction ^{12}C(p,2p)^{11}B (a) measured at RNCP Osaka in direct kinematics [13] and (b) measured at the R^{3}B-LAND setup in inverse kinematics [12]. Both spectra extend to excitation energies associated with the proton-knockout from the s-shell. Figure (a) adapted from [13] under Creative Commons, CC-BY-3.0.

similar to the one which will be described in the next chapter. A CH_2-target and a carbon target were used, and cross sections for both the carbon and the hydrogen-induced knockout leading to ^{11}B were calculated to be $\sigma_C = (46 \pm 4)$ mb and $\sigma_H = (18 \pm 3)$ mb, respectively.

The excitation spectrum of the ^{11}B fragments was reconstructed by combining the energy spectrum of the γ-rays emitted by surviving ^{11}B with the excitation energy obtained using the invariant mass method in the case of a subsequent breakup. The resulting energy spectrum is shown in Fig. 2.6, and is compared to the spectrum obtained in direct kinematics obtained at RNCP* in Osaka [13].

* Research Center for Nuclear Physics

In this experiment, which was especially aimed at the measurement of the s-shell knockout, a natural carbon target was bombarded with protons at an energy of 392 MeV. The two spectrometers Grand Raiden and LAS* were used to analyze the particles, and both the decay products of highly excited ^{11}B and the two protons from the (p,2p) reaction were measured using sixteen silicon telescopes. The excitation spectrum shown in Fig. 2.6(a) was calculated from the measured proton energy.

Both spectra extend to excitation energies associated with the proton-knockout from the s-shell, underlining the sensitivity of these kinds of reactions to deeply bound states, as well as their capabilities in both direct and inverse kinematics.

* Large Acceptance Spectrometer

3 Experimental Setup

Experiment S393 was performed in August 2010 at the R^3B^*-LAND† setup at GSI‡. Its aim was to study light nuclei ($Z \leqq 10$) of varying nucleon asymmetry in kinematically complete measurements of reactions at relativistic energies. Apart from measuring the quenching of single-particle strengths in these nuclei, also e.g. the evolution of α clusters and neutron shells in relation to nucleon asymmetry and several reactions relevant for the astrophysical r-process were under investigation.

In the following, the experimental apparatus used to perform the experiment will be described. After briefly reviewing the beam production and transport at GSI in the first two sections, the final section will give an overview over the detectors used at the R^3B-LAND setup during the experiment.

3.1 Beam Production and Beam Transport at GSI

The relativistic particle beam was provided by the SIS-18§ [31]. The 18 in the name depicts the maximum magnetic rigidity $B\rho = 18$ Tm of the synchrotron. The SIS-18 is fed by the UNILAC¶ which accelerates the ions produced in the ion sources up to an energy of 11.4 *A*MeV. Both UNILAC and SIS-18 are very versatile systems and can provide very different beams ranging from protons to uranium. Figure 3.1 shows an overview of the facilities at GSI. Both UNILAC and SIS are shown in the figure, as well as the experimental areas.

In the experiment discussed here, an $^{40}Ar^{11+}$ primary beam, accelerated to an energy of 490 *A*MeV was used. After its acceleration, the ions were transported to the FRS || which is shown in Fig. 3.2. The FRS is a high-resolution forward spectrometer used to analyse radioactive ion beams beams at relativistic energies [32]. It has four stages, each consisting of a 30° dipole magnet to deflect the ions, five quadrupole magnets to focus the beam and two sextupole magnets two correct for second-order aberrations. The beam coming from the SIS-18 was incident on a thick beryllium production target (4011 mg/cm^2) at the entrance of the FRS with an intensity of $6 \cdot 10^{10}$ ions per spill, one spill having the length of 2 s.

In the production target, a wide range of nuclei is produced in fragmentation reactions. To select the nuclei of interest, the fact that nuclei get deflected onto different paths in the magnetic field according to their magnetic rigidity is exploited. Assuming the reaction products are fully stripped ($Q = Z$), due to the Lorentz force $F_L = q\,v \times B$, the path of the ions and their mass-to-charge ratio A/Z are connected via

$$B\rho \propto \frac{A}{Z} \cdot \beta\gamma \tag{3.1}$$

* Reactions with Relativistic Radioactive Beams
† Large Area Neutron Detector
‡ Gesellschaft für SchwerIonenforschung: GSI-Helmholtzzentrum für Schwerionenforschung GmbH
§ SchwerIonenSynchrotron, Heavy Ion Synchrotron
¶ UNIversal Linear ACcelerator
|| FRagment Separator

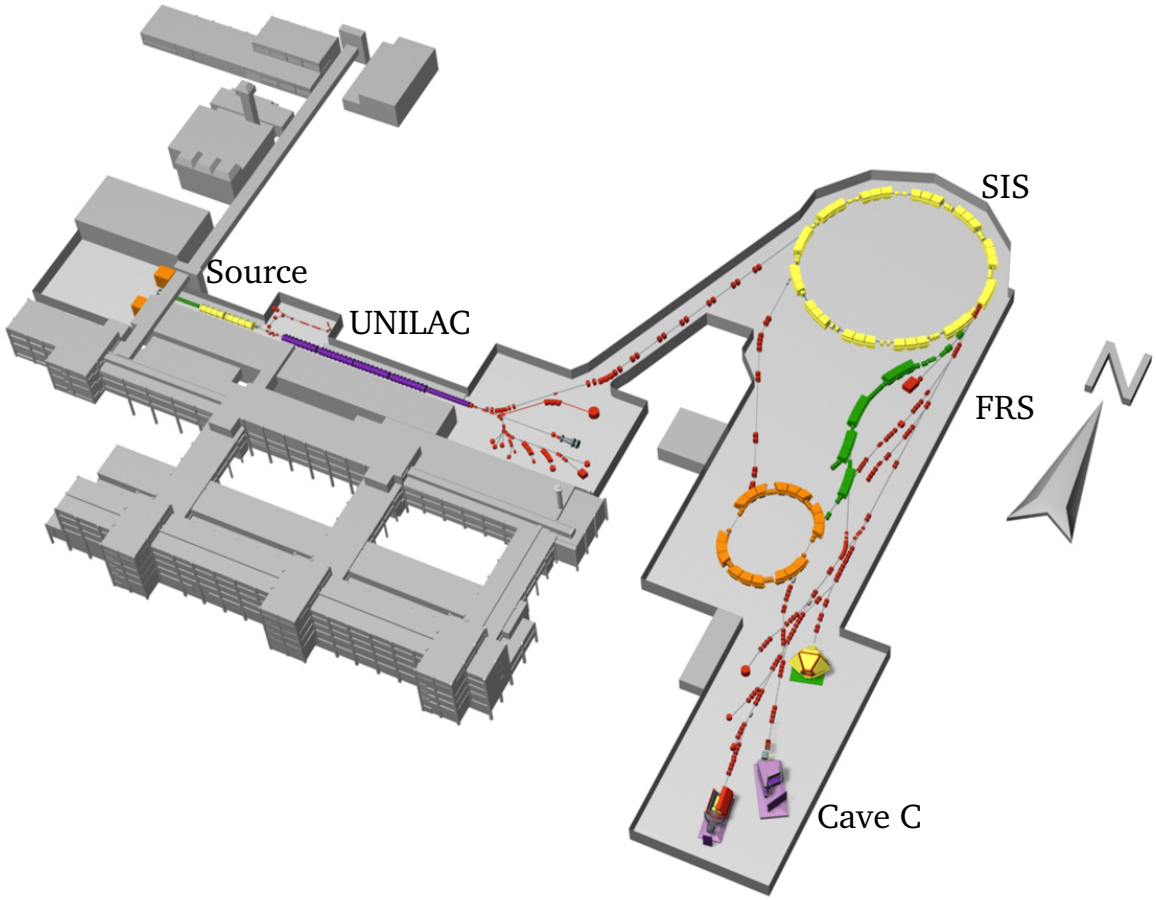

Figure 3.1: Overview of the facilities at GSI [30]. The ions procuded in the ion sources are first accelerated in the UNILAC, which accelerates them up to an energy of 11.4 AMeV and transports them to the SIS-18. In the present experiment, the SIS accelerated $^{40}Ar^{11+}$ primary beam to an energy of 490 AMeV. These ions were then incident on a production target at the entrance of the FRS, and the reaction products in the A/Z-range of interest were then transported to the R^{3}B-LAND setup located in Cave C.

Here, $B\rho$ is the magnetic rigidity of the FRS, $\beta = v/c$ the velocity v of the particle in units of the speed of light, c, and $\gamma = 1/\sqrt{1-\beta^2}$ is the Lorentz factor. It is possible to further improve the purity of the beam by inserting a wedge-shaped degrader at the second focus of the FRS. However, this was not done, due to the relatively low intensity of the secondary beams and since, because the broad scope of the experiment, it was desired to have as many different isotopes in the selected A/Z-range as possible reach the experimental setup.

Over the course of the experiment, six $B\rho$-settings of the FRS where used, allowing a study of the entire range of A/Z, ranging from ≈ 1.5 to ≈ 3.0. For the experimental runs analysed in this work, the FRS was tuned to a setting which selected only the most neutron-deficient isotopes ($A/Z \leqq 2$). These ions were transported to Cave C where the secondary target and the experimental setup were situated.

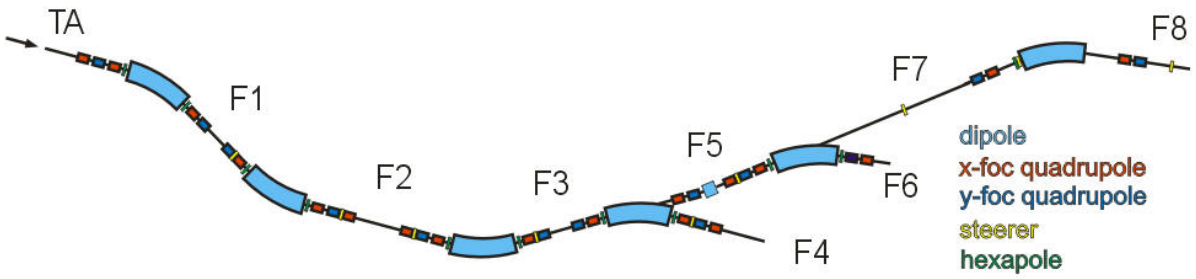

Figure 3.2: The fragment separator FRS, including the beamlines to the experimental areas.

3.2 The R3B-LAND Setup at Cave C

Figure 3.3 shows the R^3B-LAND setup as it was used in experiment S393. For simplicity, the proton branch is not shown. The setup provides the possibility to measure reactions with relativistic radioactive beams in complete kinematics.

3.2.1 Incoming Particle Identification

The incoming particles were identified by measuring their time-of-flight and their charge. For the time-of-flight measurement two plastic scintillators were used, one situated at the focal plane S8 of the FRS and one situated at the entrance of Cave C. The detector at the entrance of Cave C, called POS, has an active area of 5×5 cm^2 and is read out with photomultiplier tubes at each side of the detector. Apart from the time measurement, it is also used to generate the main trigger of the experiment.

For the charge measurement, a position-senstive pin diode (PSP) is used. The PSP is a square plate of high-resistivity n-type silicon with a thickness of 300 μm and an active area of (4.5×4.5) cm^2. It is read out from a single contact on the cathode, and on the four corners on the anode side. The energy deposited in the detector by a particle with charge Z is described by the Bethe-Bloch formula

$$\frac{dE}{dx} = \frac{4\pi e^4 Z^2}{m_e c^2 \beta^2} nz \left[\ln \frac{2m_e c^2 \beta^2}{I} - \ln\left(1-\beta^2\right) - \beta^2 \right], \tag{3.2}$$

in which e is the elementary charge, m_e the mass of an electron, and n,z, and I are number density, charge, and mean excitation potential of the detector material. Hence, a measurement of the energy loss in the detector yields the charge.

The PSP can also be used to obtain two-dimensional position information of the passing particles. For this, the energy signal from the four anodes are read out separately and then used to calculate the position of the particle. However, due to the superior position resolution of the Silicon Strip Detectors surrounding the target (see Sec. 3.2.2), the position information from the PSP was not used in the present analysis.

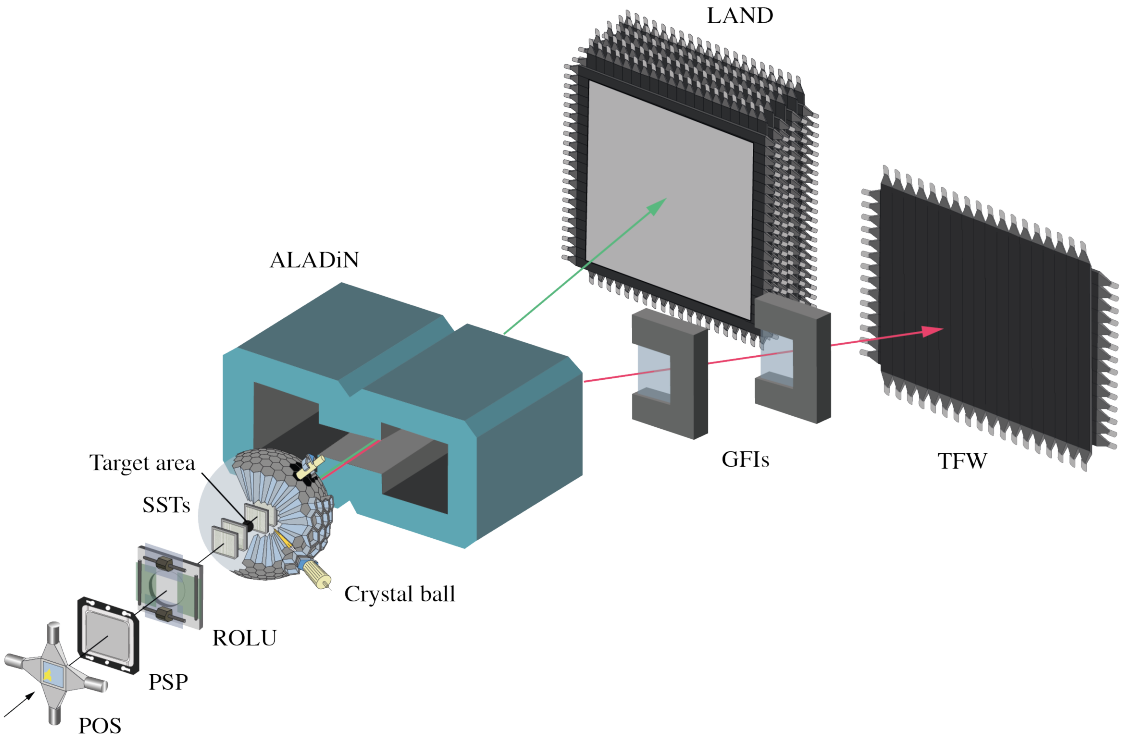

Figure 3.3: The experimental setup at Cave C (schematic). With this setup it is possible to measure reactions with relativistic radioactive beams in complete kinematics. The target area consists of the target and its support structure, eight double-sided silicon strip detectors (SSTs) and the Crystal Ball γ-detector. The proton branch of the setup, consisting of two drift chambers and a second time-of-flight wall, is not shown for simplicity. Image taken from [33].

Also in front of the target, the ROLU (abbreviation for the German "Rechts-Oben-Links-Unten") detector was inserted. ROLU consists of four movable plastic scintillators and can be used to restrict the beam size. This is achieved by using signals coming from one of the scintillators to veto the trigger coming from POS.

3.2.2 The Target Area

The central part of the setup is the reaction target. During the experiment, eight targets of the size of (3 × 3) cm^2 were mounted on a wheel. A ninth target position was left empty for backgorund measurements. Depending on the reaction under investigation, the different targets could be moved in the beamline by a step motor. In the case of the quasi-free scattering reactions analysed in this work, only two targets were used, a polyethylene (CH_2) target with an area density of 922 mg/cm^2, and a carbon (C) target of 935 mg/cm^2. Due to time constraints, the experimental runs with the carbon target were used both to subtract the C-contribution in CH_2 and as background measurements and no additional background measurements with an empty target frame were done. Figure 3.4 shows a picture of the target area.

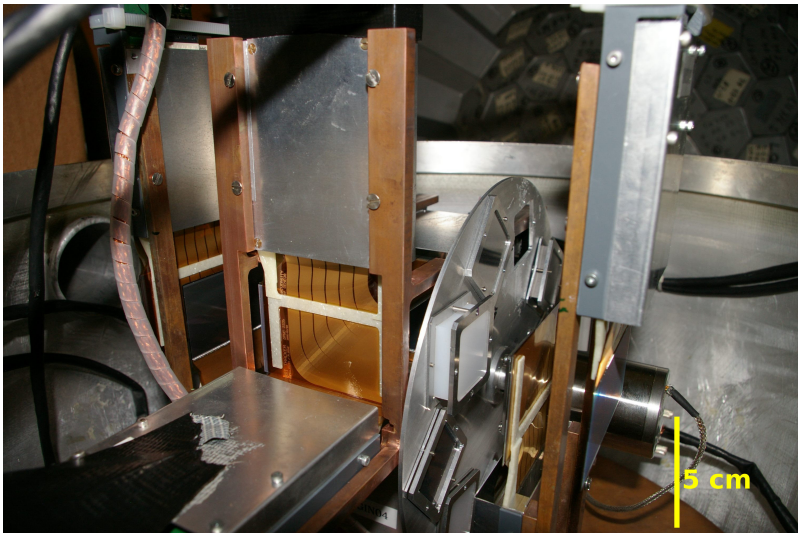

Figure 3.4: Photograpgh of the target area. The beam direction is from right to left. The target wheel with the different targets mounted on it can be seen in the middle. In front of it, two DSSDs are visible, and the support structure of the box DSSDs can be seen behind it.

Apart from the target wheel, the support structures of the Double-Sided Silicon Strip Detectors (DSSD) can be seen in Fig. 3.4. In total, eight DSSDs were used in the experiment, which were mounted in close proximity to the target. Figure 3.5 shows the geometry in which the detectors were arranged. Two detectors were placed in front of the target, two behind it. They served for the measurement of the incoming and outgoing trajectories of the beam, respectively. The first detector behind the target was in addition used for charge identification of the reaction fragments. The remaining four DSSDs formed a box surrounding the target. The aim of this box of detectors was to measure both the knocked out and scattered protons, however, due to severe problems with these detectors and their bonding to the electronics, they were not used in the analysis presented in this work.

A description of the basic principles of particle detection with silicon strip detectors can be found in Chapter 7.1. The DSSD design used in the R^3B setup is based on detectors developed by the AMS * collaboration [34]. Each of the detectors has a size of 7.2×4.1 cm^2, and is 300 μm thick. The pitch size on the junction (S-) side is 27.5 μm and every fourth strip is read out, leaving the rest of the strips floating, resulting in 640 readout channels. The charge collection of the floating strips is achieved by capacitive coupling of the strips, thus improving the position resolution significantly over the readout pitch of 110 μm. On the ohmic (K-) side the pitch is 104 μm with each of the 384 strips being read out.

The DSSDs are read out using 64-channel VA-preamplifier-shaper ASICs † produced by Gamma-Medica [35]. Figure 3.6 shows a detector connected to one frontend board housing 16 VA-chips. The output of the ASICs is sent to the SIDEREM ‡, which takes care of digitizing and filtering the data. A detailed description of both the SIDEREM and the VA ASIC family can be found in Chapter 7.

* Alpha Magnet Spectrometer
† Application-Specific Integrated Circuit
‡ SIlicon DEtector REadout Module

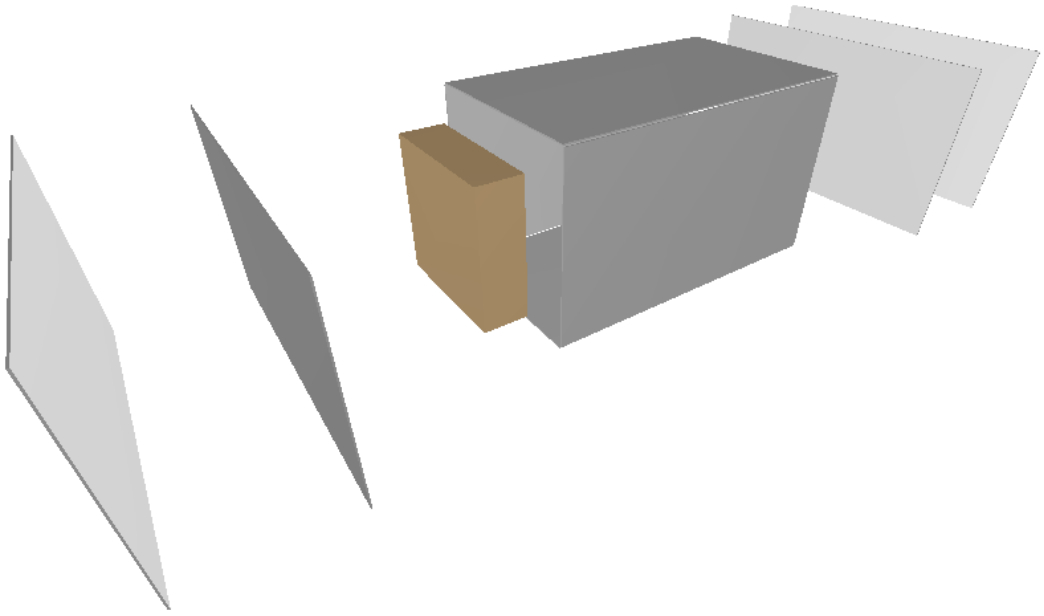

Figure 3.5: The geometry of the DSSDs surrounding the target. A pair of detectors was placed in front of the target, another pair behind it. The remaining four DSSDs formed a box around the target. The beam direction in the picture is from left to right.

The target chamber was surrounded by the Crystal Ball, a 4π array consisting of 162 sodium iodide crystals [36], which was used for the detection of γ-rays emitted by the deexciting fragment as well as scattered protons and neutrons. The detector has an inner radius of 25 cm, and each of the Na(Tl)-crystals is 20 cm long. To reach maximum angular coverage, the crystals come in four different shapes, a pentagon and four different hexagons, each covering a solid angle of 77 msr.

The scintillation light produced by incident γ rays or particles is converted to electric signals by photomultiplier tubes (PMTs). While most of the PMTs are used to read out the signals of γ-rays only, the readout of 64 of the crystals in the forward hemisphere has been modified in order to to measure signals from protons as well. This is achieved by an additional readout branch in front of the last amplification stage of the PMTs. The resulting gain for these signals is by a factor of 15 lower than the one for the γ-branch. While the γ-branch is equipped with electronics for both timing and energy signals, only the energy is read out from the proton branch.

3.2.3 Outgoing Particle Detection and Identification

After leaving the target area, the reaction products passed through the magnetic field of the ALADIN* dipole magnet. Similarly to the dipoles in the FRS, the magnetic field of ALADIN causes the flight path of fragments and protons to bend, while neutrons are not affected. The heavy fragments are bent towards the fragment arm of the setup, consisting of two fiber detectors used for position and therefore mass measurements and a time-of-flight wall.

* A LArge DIpole magNet

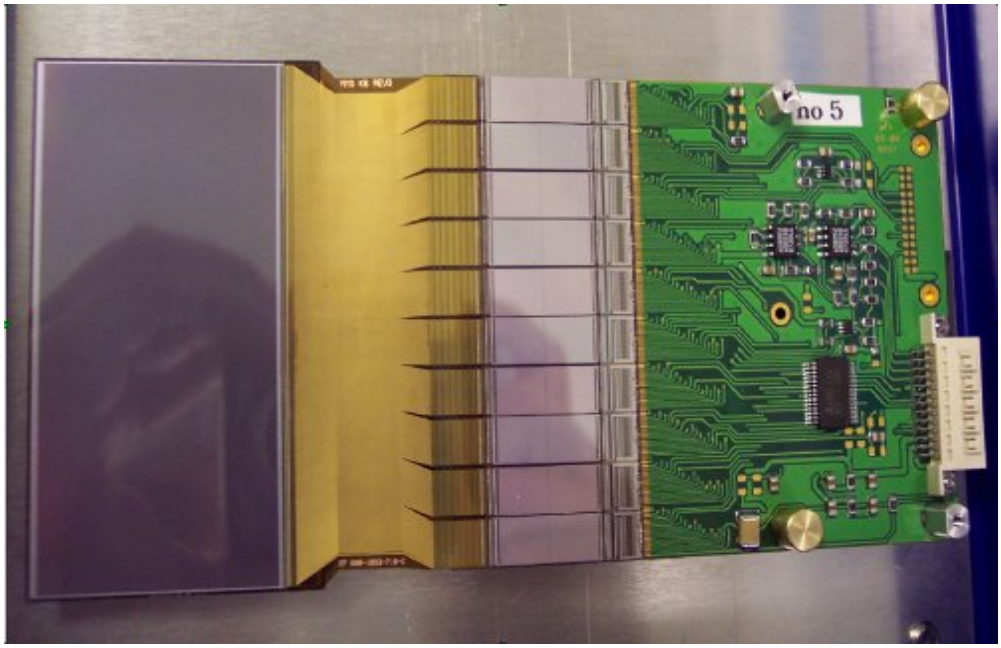

Figure 3.6: A DSSD connected to a frontend electronics board. The detector, has a size of 7.2×4.1 cm^2.

A schematic of one of the two fiber detectors [37] (GFI*) is shown in Fig. 3.7a. Each GFI consists of 480 parallel scintillating fibers with a square cross section of 1×1 mm^2. Each of the fibers is coated with optical cladding, a material of lower refractive index than the fibers used to guide the light. In total, the detectors cover an area of 50×50 cm^2. Each fiber is connected at one end to the photocathode of a position-sensitive photomultiplier (PSPM) using a specially designed mask. A schematic of this mask is shown in Fig. 3.7b. The fibers are placed on the cathode in a meandering structure, as indicated by the dotted lines in the figure. The anode consists of a grid of 18 wires in one direction and 16 wires orthogonal to that. By measuring the charge in the different wires, it is possible to deduce which fiber sent light to the photocathode and therefore where the detector was hit. The Timing- PMT shown in figure 3.7a was not read out during the experiment.

Behind the two fiber detectors, the time-of-flight-wall (TFW) was situated. The TFW consists of 32 plastic scintillator paddles, 18 horizontal and 14 vertical, arranged in two layers. Each paddle is 0.5 cm thick and 10 cm wide, the vertical ones are 147 cm long and the horizontal ones 189 cm. Each paddle is read out using a PMT at each far end. This allows independent position, time and energy loss measurements from both layers. While the time and position measurements are used to determine velocity and flight path of the fragments, the energy-loss is used for the charge identification using the Bethe-Bloch formula, Eq. (3.2).

The setup also offers the possibility to detect fast neutrons and protons which are emitted from a deexciting fragment. The neutrons, unaffected by the magnetic field, fly straight into LAND [38]. LAND serves as a time-of-flight spectrometer with an efficiency above 94 % for neutrons with energies of 400 MeV or higher.

* from German “Großer Fiberdetektor”

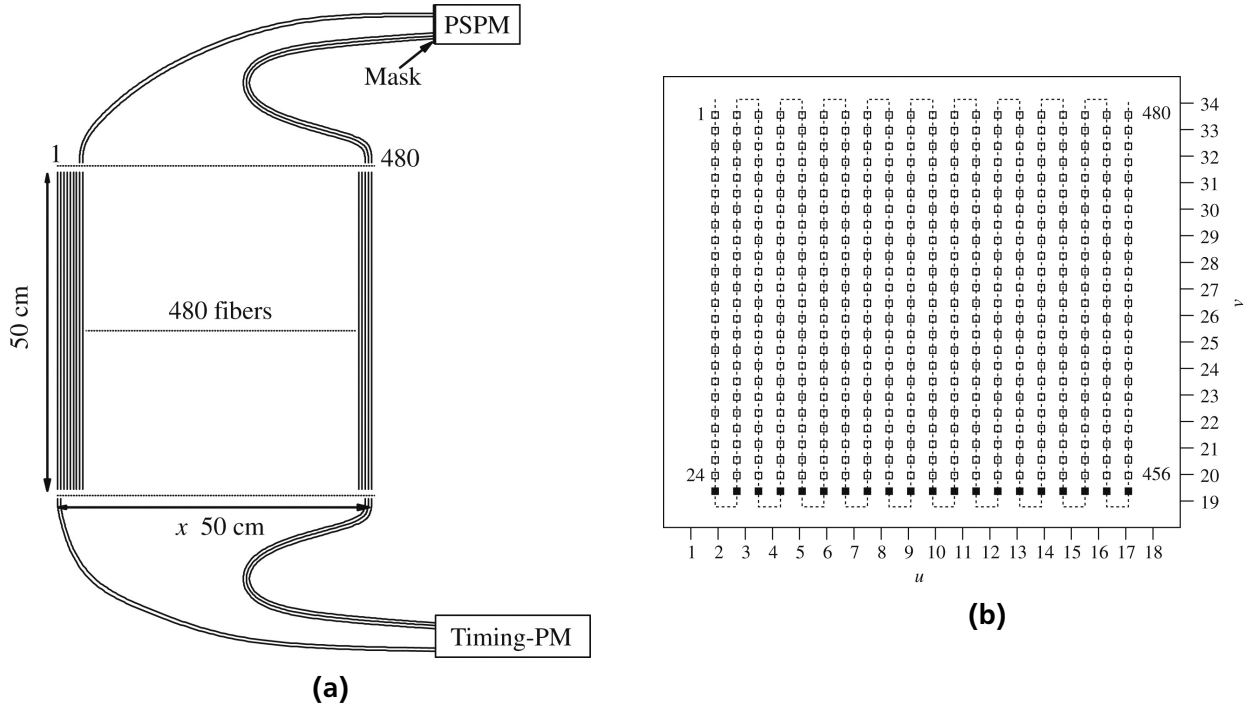

Figure 3.7: Schematic of a fiber detectors and the mask used to connect the fibers to its position-sensitive photomultipliers [37]. Copyright ©1998 by Elsevier B.V.

The protons are bent in the magnetic field towards the proton branch of the setup which consists of two proton drift chambers (PDCs) and a time-of-flight wall (DTF*). The PDCs are wire chambers, filled with a gas mixture of argon and CO_2. They have an active area of 100×80 cm^2 and consist of two perpendicular layers of wires. A proton passing the detector ionizes the gas. The produced electron avalanches drift to the nearest read-out wires, which makes it possible to track the proton path through the detector.

In the analysis presented in this work, LAND and the PDCs were not used, and the DTF was only used for triggering. Because of this, no further details will be given. Further information on the usage of these detectors can be found e.g. in Refs. [39, 40, 41].

3.2.4 The MBS Data Acquisition System

During the experiment data was stored event-wise using the Multi-Branch System (MBS) developed at GSI [42]. The data acquisition (DAQ) takes care of converting the analog electrical signals coming from the detectors into digital values which can be stored in so-called list-mode data files (LMDs). Since the setup consists of many subsystems, i.e. detectors, and the dead time of the system should be reduced to a minimum, data reduction is critical. Therefore, the DAQ has to be able to distinguish events of interest from the rest prior to the digitization.

* German:“Dicke ToF-Wand”

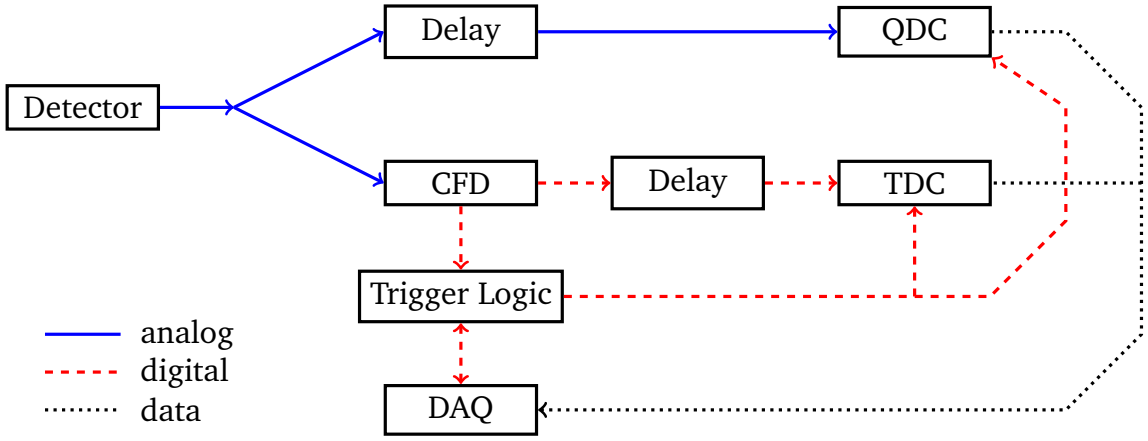

Figure 3.8: Readout of the readout of a scintillating detector. The signal coming from the detector is split into an energy and a timing branch. The CFD delivers two outgoing signals, one to a TDC and one to the trigger module. The trigger module forwards it to the DAQ, where the readout decision is made. If the event is accepted, a master trigger is sent from the main DAQ, and both the timing signal from the TDC and the energy signal, from the QDC are read out.

Figure 3.8 illustrates a typical readout of a scintillating detector via a PMT. The signal coming from the detector is split into an energy and a timing branch. The timing signal is fed into a constant fraction discriminator (CFD). The CFD delivers two outgoing signals, one is sent to a time-to-digital converter (TDC) and the other one to the trigger module. Via the trigger module, the signal is sent to the main data acquisition, were the decision wether this event should be recorded or not is made. If the event is to be recorded, a master trigger is sent from the main DAQ to all subsystems, and both the timing signal from the TDC and the energy signal, which previously had been delayed before being sent to a QDC are read out.

Most detectors in the setup are read out in this manner. Exceptions are e.g. the DSSDs, whose electronics are incapable of delivering a fast timing signal and which therefore can not send a trigger to the DAQ.

The DAQ decision on recording an event depends on the dead time of the system, the triggers coming from different detectors and the downscale factor. While in previous experiments different modules were needed to combine the triggers coming from the detectors and to perform dead-time blocking and downscaling, in experiment S393 this was done by a VULOM [*]. The VULOM is a FPGA-based module which can be programmed using the hardware description language VHDL to fulfill various tasks. In this case it was configured as trigger logic module (TRLO). The TRLO combines the triggers coming from different detectors to trigger patterns (TPATs), which are written to the event stream together with the detector data.

The trigger patterns are summarised in Table 3.1. In the first two columns, trigger pattern and trigger name are given. The next nine columns show, whether a detector was required (+) or used as a veto (-) for a certain trigger pattern. The final column gives the downscale factor. Since reaction rates are usually very low and the data rate is limited, trigger patterns which are not associated with a certain

[*] VME Universal LOgic Module

Table 3.1: Overview of the on-spill triggers used during the experiment. The sign ∧ in the matrix denotes, that the detector was used to generate the trigger, the sign ¬ that a signal from the detector was used as a veto.

TPAT	Name	POS	ROLU	S8	TFW	XB	DTF	Pixel	LAND	Downscale
1	Good Beam	∧	¬							128
2	Fragment	∧	¬		∧					16
4	S8			∧						1024
8	XB Sum	∧	¬		∧	∧				1
16	Proton	∧	¬		∧		∧			1
32	Pileup	∧	¬							1
64	Pixel		¬					∧		1
128	Neutron	∧	¬		∧				∧	1

kind of reaction are downscaled. E.g. the “Good Beam” trigger, denoting that the beam hit the target has a downscale factor of 128, meaning that only every 128th event fulfilling these conditions is recorded, if no further trigger condition than POS was fulfilled.

The most important triggers for the analysis described in this work are the “Fragment” trigger, used for the measurement of the unreacted beam, and the “XB sum” trigger used for measuring high energy events, i.e. nucleons, in the Crystal Ball. Only on-spill triggers, used for data taking with the particle beam are listed in table 3.1. Several off-spill triggers are used as well, including such triggers necessary for the calibration of the Crystal Ball and LAND using cosmic muons, and the TCAL and CLOCK triggers which are used by the calibration routines of the same name described in Sec. 4.1. The CLOCK trigger is sent regularly while there is no beam and used to determine the pedestals of the QDC by sampling the data coming from them without physics data. The TPAT trigger, on the other hand, is sent to a time calibration module. This module chooses a random time period, sends the duration of this time period to the DAQ to be stored in the LMD, and sends gates of this duration to all TDCs. The comparison of the real duration and the one measured by the TDCs can be used during the analysis to calibrate the data from the TDCs.

4 Data Calibration

4.1 The Analysis Package Land02

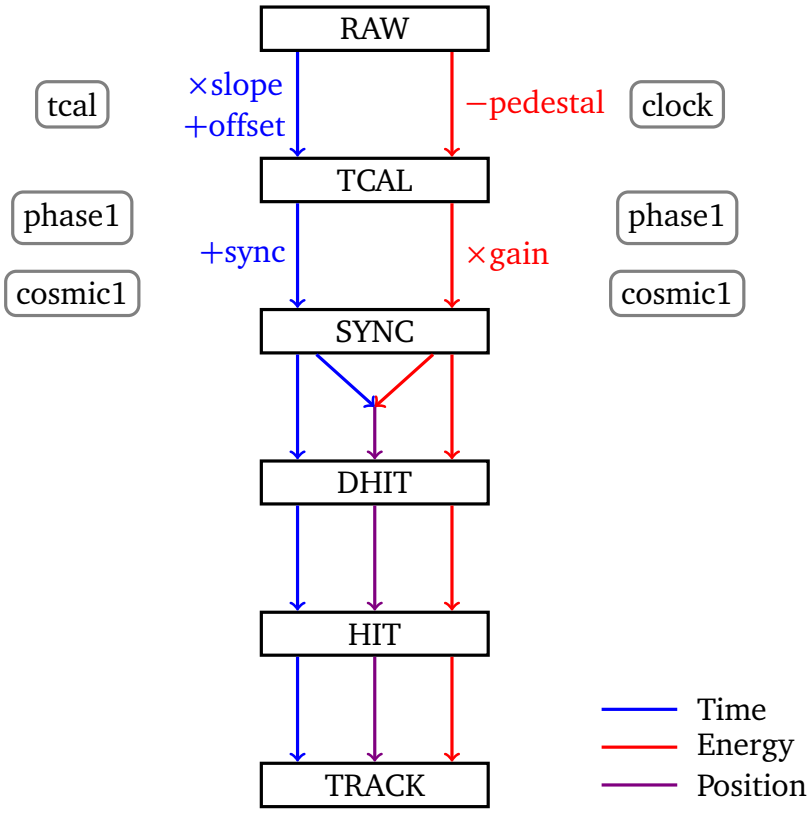

Figure 4.1: Schematics depicting the different data levels of the land02 software package and different routines for the automatic determination of calibration parameters.

For the analysis, the land02 software package [43] was used to bring the lmd-files created by the data acquisition into a format which could then be analysed using ROOT [44]. This data treatment is called unpacking. During unpacking calibration parameters are applied as well. Figure 4.1 gives an overview of the land02 software with the different data levels and the routines to determine the different calibration parameters. The mentioned data levels are briefly explained in the following:

RAW: On this level, the data is stored as collected from the DAQ, as integer numbers giving values in channels of the TDCs, QDCs, etc.

TCAL: This level is an intermediate step during the timing and energy calibration. A slope and an offset have been applied to the timing channels which are now calibrated to ns. For energy channels, the pedestals have been subtracted.

SYNC: This is the second step of the time and energy calibration: Offsets have been added to the times, in order to set them to a common zero. The energies are usually converted to MeV by applying gain factors.

DHIT: The DHIT level contains values in detector-specific coordinates describing hits. Information from several detector channels is combined, giving e.g. the total energy loss in a detector and hit positions. Also, from this level on, most values have an associated error.

HIT: The hits are now described in a generic manner. Positions are given in cm in a detector internal coordinate system with the origin at the center of the detector.

TRACK: For the incoming particle identification, the TRACK level is available. In this level, data from different detectors is combined to calculate characteristics of the incoming nuclei necessary for their identification, i.e. their charge, A/Z, or velocity.

In addition in figure 4.1, the different routines used to calibrate the data are indicated. These routines are used to automatically determine the different gain factors and offsets used to convert the data to physical quantities.

clock: This routine determines the pedestals of the QDCs in the setup using events without detector signals. These signals were measured using the CLOCK trigger mentioned in Sec. 3.2.4

tcal: This routine performs the calibration of the timing signals of the different detectors, the resulting values are given in ns. The calibration makes use of signals acquired with the TCAL trigger.

phase1 and cosmic1: These routines synchronize the signals coming from different channels of the same detector and add gain factors and offset parameters.

Also, scripts are available which measure and correct for the time dependency of each of the calibration parameters. While these calibrations are done almost automatically by land02 and require only little user input, for a number of detectors it is necessary to apply additional manual corrections. In the following, examples for these manual calibrations will be highlighted for three detectors, with emphasis on the calibration of the in-beam silicon strip detectors.

4.2 Fiber Detector Calibration

As described in Sec. 3.2.3, the fiber detectors are read out using a position-sensitive photomultiplier to which the mask holding the fibers is connected. In order to get the correct hit position, the detector has to be calibrated, assigning each signal to the correct fiber. This is done using data collected during sweep runs, i.e. runs without a reaction target, during which the current running through ALADIN is varied in order to hit the entire detector with the beam at one point.

The position on the photocathode, i.e. the firing fiber, can be determined from the centroid of the measured charge distributions. However, due to the position-dependent gain of the PSPM, the signals have to be gain-matched first [45]. This is performed by fitting a function of the form

$$f(x) = \exp[f_0 + c_0(x - x_0)^2], x \in u, v \tag{4.1}$$

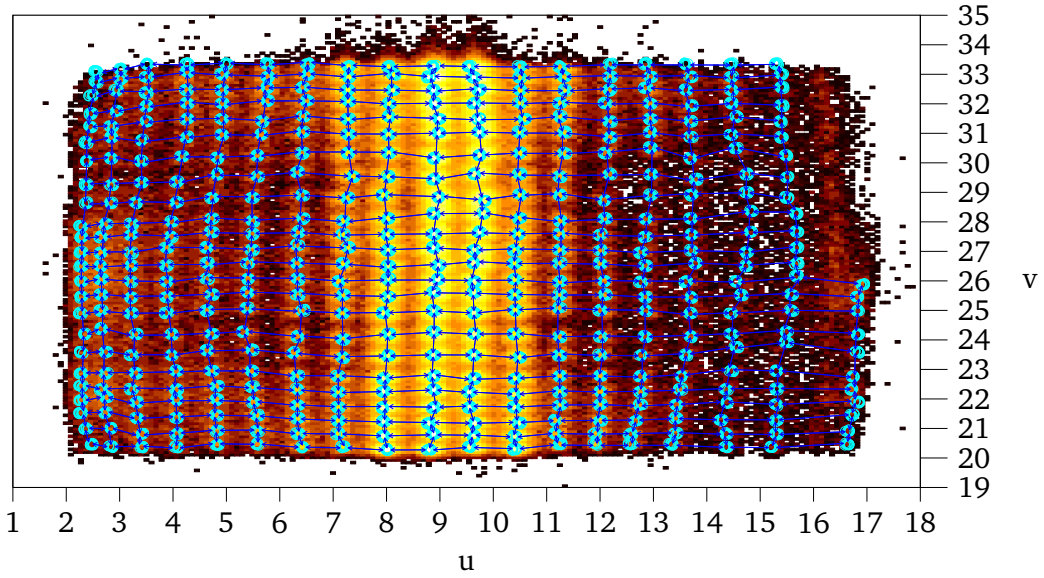

Figure 4.2: Calibration of the fiber mask of a fiber detector. The (u,v)-position on the photo cathode is plotted and a Gaussian is fitted to each cluster. From the determined cluster position and the distance between neighbouring clusters a grid is constructed, which also shown in the figure.

to the measured charge distributions in u- and v-direction and solving the equation system given by the residues, i.e. the difference between the fitted and measured charge values, using the least-square method.

After the gainmatching, the fiber mask is calibrated by plotting the (u,v)-position of a large number of hits and fitting a Gaussian to each cluster, as is shown in Fig. 4.2. From the determined cluster position and the distance between neighbouring clusters a grid is constructed, which is also shown in the figure. This grid can be used to assign a probability w_i that a signal originated from a certain fiber i. Finally, the postion of a hit can be calculated using

$$x = \frac{\sum_i w_i x_i}{\sum_i w_i}. \tag{4.2}$$

4.3 Crystal Ball Calibration

The γ-branch of the Crystal Ball was calibrated using a ^{22}Na and a ^{60}Co source. The photons emitted by these sources have well defined energies of 0.511 MeV and 1.275 MeV (^{22}Na) and 1.173 and 1.333 MeV (^{60}Co) which can be used to calculate the energy offset and gain of each crystal by determining the peak positions with Gaussian fits and using the formula

$$E_i(\text{ch}) = g_i \cdot (E_\gamma(\text{MeV}) - o_i). \tag{4.3}$$

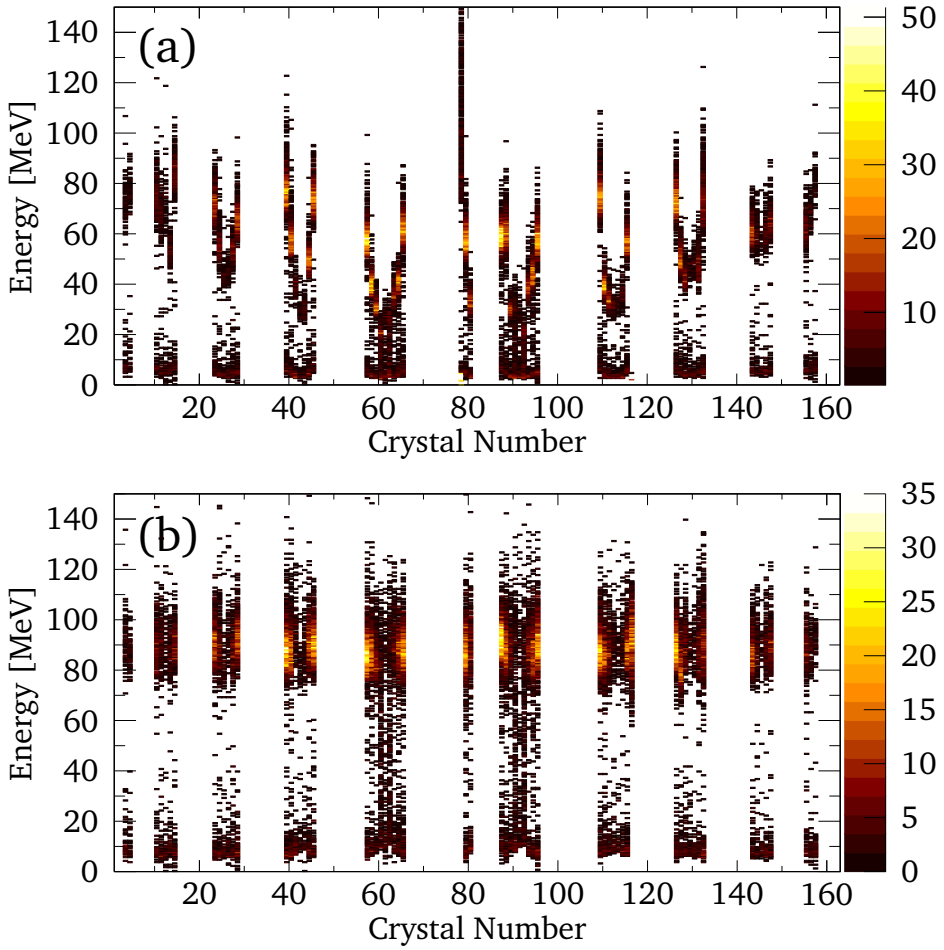

Figure 4.3: Energy spectra as a function of crystal number for the proton branch of the Crystal Ball stemming from cosmic muons which centrally hit the detector. The empty bins belong to crystals without a proton readout. (a) Before gain-matching. (b) After gainmatching.

Here E_i is the measured energy of crystal i in ADC channels, E_γ is the known energy of the photon from the source, and g_i and o_i are gain and offset values for this crystal.

The energies measured with the proton branch differ by two orders of magnitude from the γ-energies, and the gain of the proton branch is only a factor of ≈ 15 lower. Using the same calibration for protons and photons is not advisable, since small uncertainties in the determination of the gain using the sources leads to large deviations at proton energies. This makes an additional calibration step necessary [41].

The gain of the different crystals is matched using cosmic muons. While these muons are minimum ionizing and their different paths through the detector lead to a continuous energy spectrum, they can be used for energy calibration if one looks at particles which travelled trough the Crystal Ball centrally. In this case, only two opposite crystals have an energy signal, and the muons can be assumed to have travelled through the entire length of the detector. Their energy loss inside the crystals is then well defined with a mean value of 92 MeV which has been previously determined using Geant3 simulations [41]. Figure 4.3(a) shows the energies of these muons as a function of the crystal number. For this plot events taken with the off-spill Crystal Ball trigger and requiring hits in opposite crystals of the detector

were selected. The energy distribution of each crystal was then fitted using a Gaussian function and the gain $g_{p,i}$ determined by

$$g_{p,i} = \frac{\mu_i}{92\ \text{MeV}}, \tag{4.4}$$

with μ_i being the mean value of the Gaussian fit. The result of this gain matching is shown in Fig. 4.3(b).

4.4 DSSD Calibration

The calibration of the in-beam silicon-strip detectors consists of several steps which in combination increase the energy and position resolution of the detectors. First, the entire reconstruction of hits in one of these detectors will be sketched.

The first step is the determination of each strip's pedestal and noise, i.e. the width (σ) of the pedestal, using the clock routine mentioned in Sec. 4.1. After the calibration parameters have been applied, the unpacking routine will compare the energy of each strip to the determined noise of this strip. Since the strips of the DSSDs are capacitively coupled, a particle hitting the detector will typically induce a signal not only in a single but in several neighbouring strips. Because of this, the unpacking routine will try to sort the energies from single strips into clusters coming from a hit from a particle. A signal larger than $3 \cdot \sigma$ indicates a particle hit in this strip. The routine will now add the energy of adjacent strips to the total energy of the cluster until the routine finds a strip with a signal smaller than $1 \cdot \sigma$. The derived total cluster energy becomes

$$E = \sum_{i=l}^{m} e_i, \tag{4.5}$$

where e_i is the energy signal of each strip, l is the first, and m the last strip of the cluster. The hit position is determined by calculating the center-of-gravity of this cluster

$$x = \frac{1}{E} \sum_{i=l}^{m} e_i \cdot x_i, \tag{4.6}$$

with the strip position x_i. Several issues become apparent:

1. Broken or noisy strips will disturb the cluster finding, causing either too many or too few strips to be associated with the same particle hit.
2. Different gains of the individual strips will decrease the energy resolution and in addition distort the position determination.
3. Similarly, since the charge collection for each signal depends on the exact position of the hit within a strip, both energy and position have to be corrected for that.

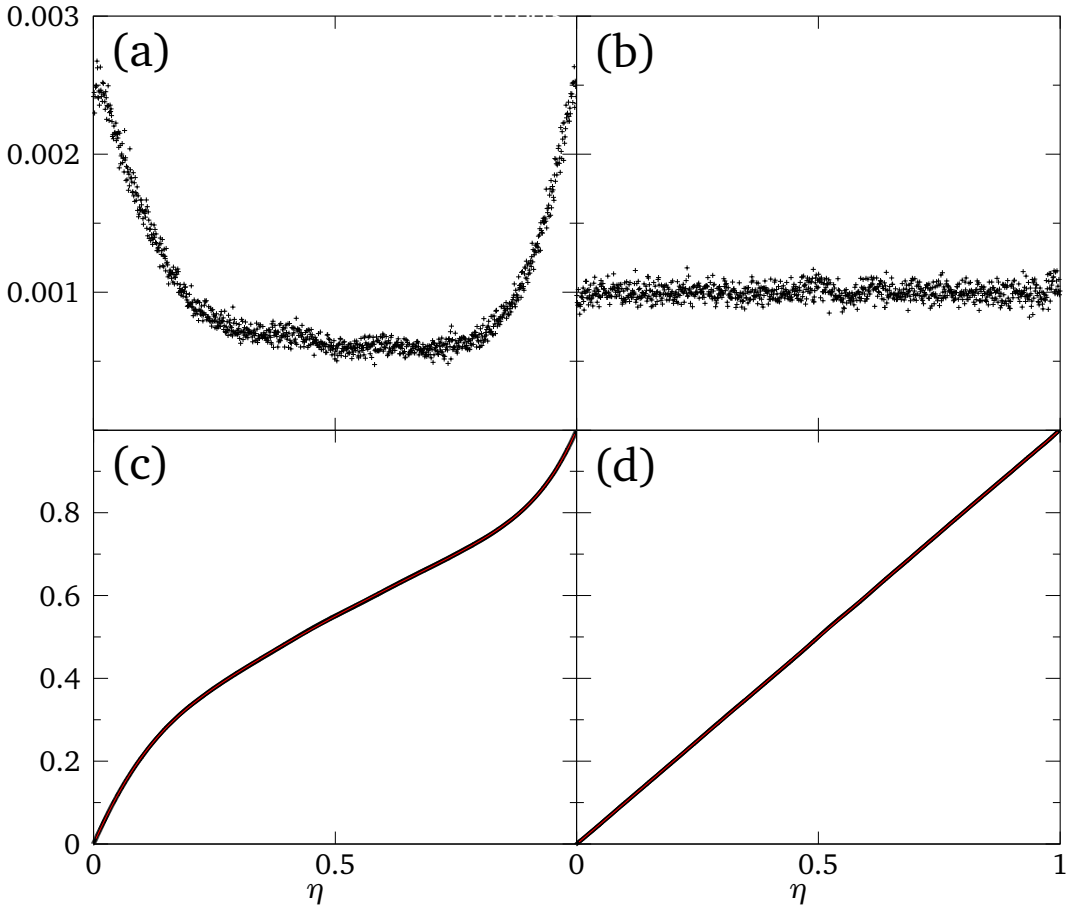

Figure 4.4: Correction of the DSSD position for the dependency on the interstrip position of the hit. As an example, carbon hits on the K-side of the detector directly in front of the target (SST 2) are shown. Figure (a) shows the number of hits plotted over the interstrip parameter η, (c) shows the integral. Figures (b) and (d) show the same distributions after the correction.

To address the first issue, it is possible to mark broken strips in the calibration file, causing the algortihm to ignore them. In addition, the missing energy from the excluded strips was estimated by averaging the energy of the two neighbouring strips. Assuming that strip b is broken, the corrected energy becomes

$$E' = E + \frac{1}{2}(e_{b-1} + e_{b+1}). \tag{4.7}$$

This turned out to be a sufficient correction unless the broken strip was the central strip of the cluster. This special case will be discussed later on.

The variation of the charge collection over the strip pitch affects both the position resolution, since hits will seem to originate closer to the strip edges than they actually do, and the energy resolution, because the energy signal will vary depending on the hit position inside the strip. In order to describe and correct these effects, a parameter called η was introduced [46] which is defined as the non-integer part of the hit position, i.e. it describes the position of a hit inside a strip

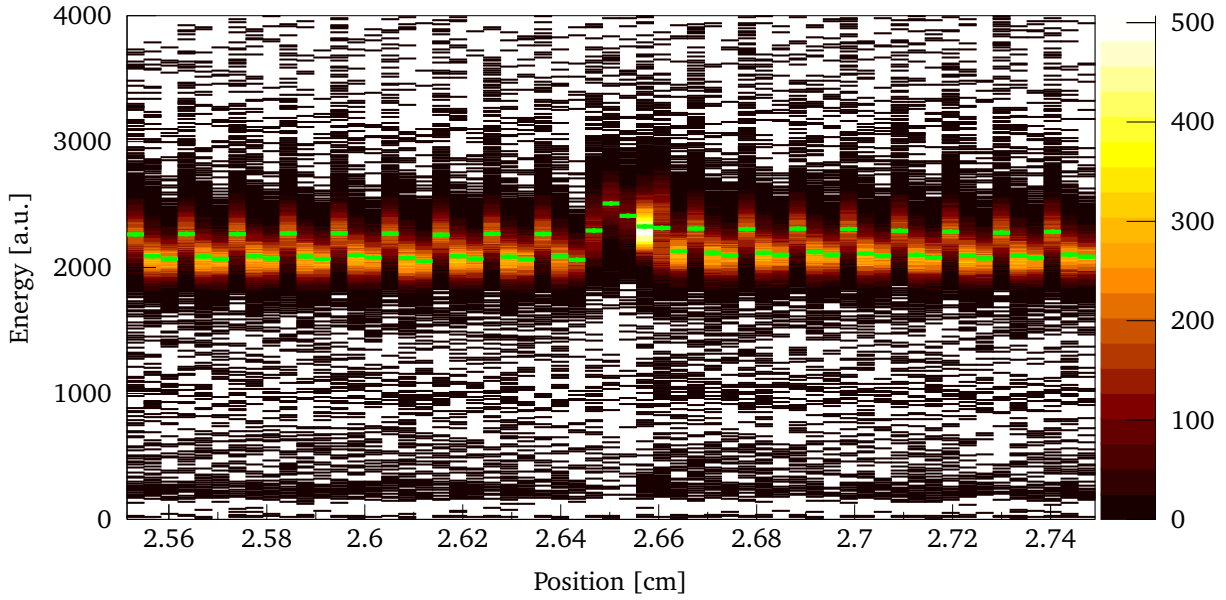

Figure 4.5: Illustration of the gain-matching routine. Shown is a part of the K-side of SST2. Each strip is divided into three bins, and a Gaussian is fitted to each of the bin. The mean values of the Gaussians are indicated in green.

$$\eta = x_0 - int(x_0). \tag{4.8}$$

Since the correction methods for both the η-energy dependence and the different strip gains require the exact hit position, the η-position correction was done first. The dependence on the position of the hit within the readout gap can be corrected by using the integral of the η-distribution of the total number of hits. The corrected position then becomes

$$x = x_0 + \int_0^{\eta} f(\eta) d\eta \tag{4.9}$$

Figure 4.4 shows the result from this correction. As an example, the K-side of SST2, directly in front of the target is chosen. Incoming carbon isotopes have been selected, and only hits with a cluster size of at least 3 strips have been taken into account. This condition on the cluster size reduces the influence of high-energy proton hits, since protons usually deposit all their energy in one or two strips. The Figures 4.4(a) and (c) show the η-distribution and its integral before the correction. In Figures 4.4(b) and (d) the same plots are shown after the correction has been applied. The dependence on η has disappeared and the distribution is almost homogeneous.

To correct for the varying gains of different readout strips, the energy is plotted against the hit position, as shown in Fig. 4.5, again for incoming carbon on the K-side of detector 2. The distribution is divided in bins (3 bins per strip), and a Gaussian function is fit to each bin. The inverse of the mean of the Gaussian can then be used as a correction factor for the energy.

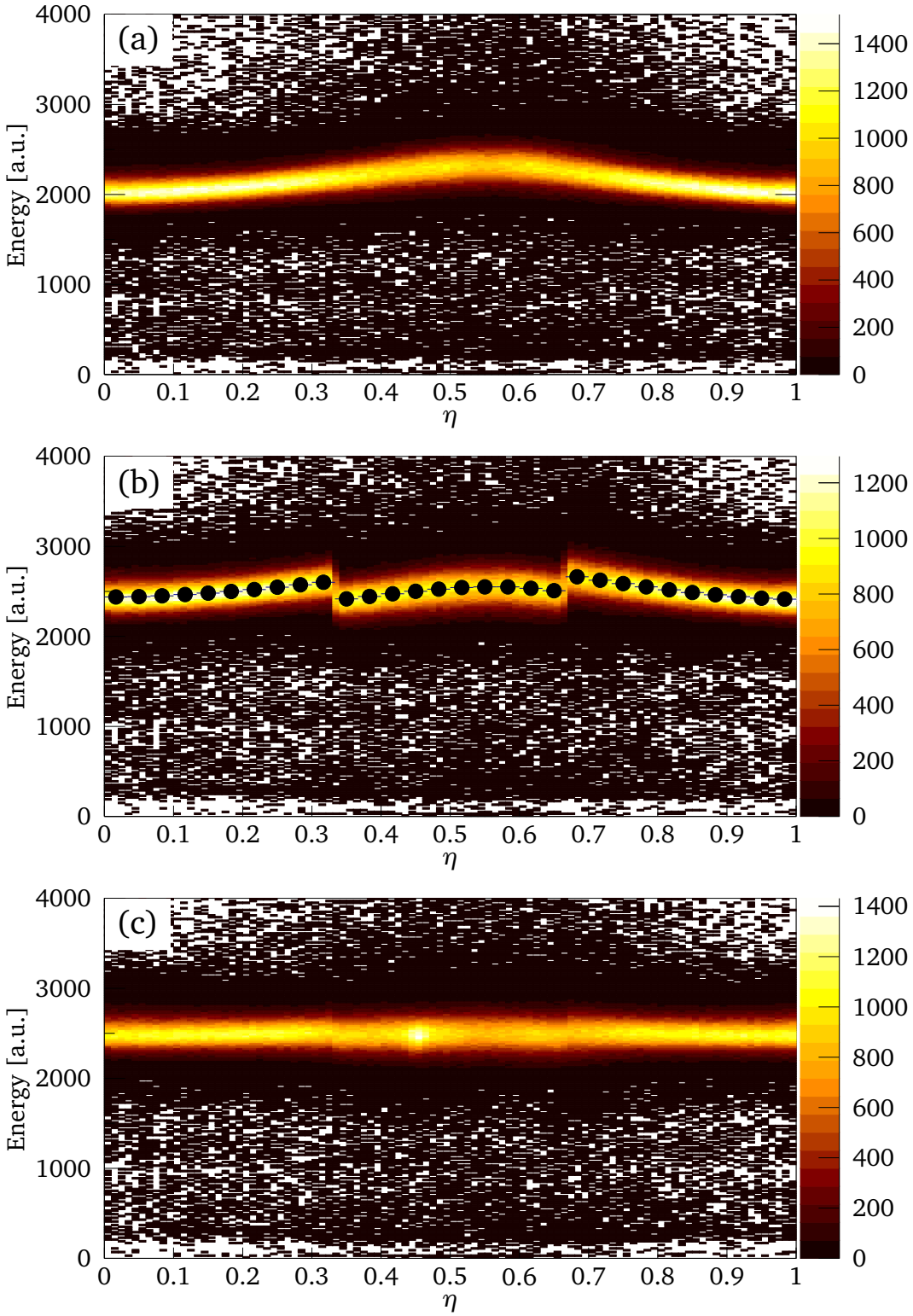

Figure 4.6: Correction of the η-dependency of the hit energy in the DSSDs. (a) Before the correction. (b) Output from the correction routine. The mean of the Gaussian fitted to each bin is indicated in the plot. The steps in the distribution stem from the division of each strip into 3 bins during the gainmatching. (c) After the correction.

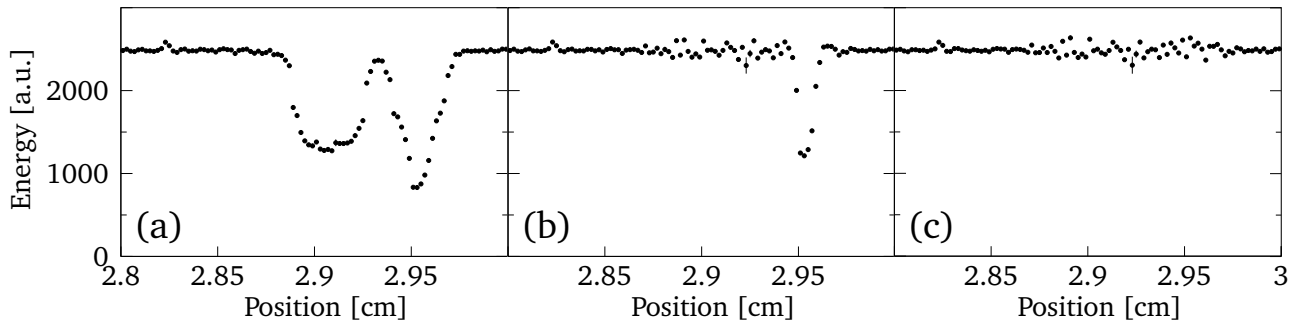

Figure 4.7: Example of the DSSD deadstrip correction. Shown is the energy profile over the position for two broken strips in close vicinity on the K-side of detector 2 (a) without any missing energy added, (b) with the average energy added according to Eq. (4.7) (c) with the energy correction according to Eq. (4.10).

A very similar technique was used to correct for the η-dependency of the energy, which is illustrated in Figure 4.6(a), once again for the K-side of detector 2 and incoming carbon. The energy is plotted against η as depicted in Fig. 4.6(b). The steps in the distribution come from the division into three bins per detector strip in the calibration step before. Again, the distribution is then divided into bins, a Gaussian function is fitted to each bin, and the inverse of the mean of the Gaussian is used as a correction factor. The corrected energy distribution is shown in Fig. 4.6(c).

A similar approach was taken in order to further reconstruct the energy of clusters whose central strip is broken. While calculating the center of gravity x_0 of the cluster, a parameter η' was defined as

$$\eta' = \begin{cases} |x_0 - int(x_b)| & \text{if } |x_0 - int(x_b)| \leqq 1, \\ 1, & \text{if } |x_0 - int(x_b)| > 1, \end{cases}$$

where x_b is the position of the broken strip, and the energy corrected according to

$$E'' = E' + 2 \cdot (e_{b-1} + e_{b-1}) \cdot (1 - \eta'), \tag{4.10}$$

adding more energy, the more centrally the broken strip was hit. The factor 2 was found empirically. In combination with the gain-matching described earlier, this correction gave satisfactory results for all detectors. Figure 4.7 shows an example: Shown is the energy profile over the position for two broken strips in close vicinity on the K-side of detector 2. While in the case of the broken strip on the left a part of its energy is collected by its neighbour, for the strip on the right this is not the case. In all three pictures both strips were marked as broken. However, on the left side no attempt was made to correct for the missing energy. In the picture in the middle only the average energy of the neighbouring strips is added, which proves to be sufficient for one of the two strips. Finally, the complete correction (Eq. (4.10)) is applied which leads to the reconstruction of the full energy in both cases.

The result of these energy corrections is highlighted in Fig. 4.8. Plotted are both the uncorrected and corrected energy for the K-side of SST3, located directly behind the target, which was also used for the

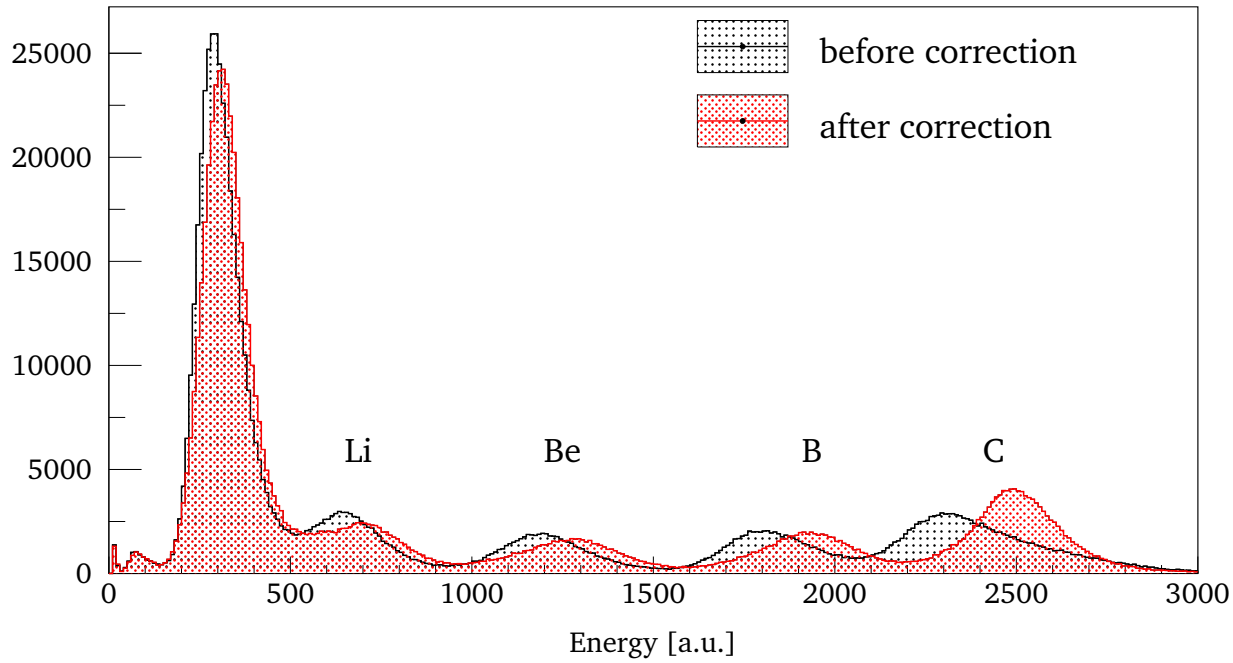

Figure 4.8: Comparison of the energy resolution of SST3 before and after all corrections have been applied. Incoming carbon has been selected in combination with the Crystal Ball reaction trigger (TPAT=8).

outgoing fragment identification described in Chapter 6. Again, incoming carbon has been selected, this time in combination with the Crystal Ball reaction trigger (TPAT=8), meaning that a nuclear reaction is likely to have occurred. The energy resolution for carbon is improved from $\approx$ 10 % to 5 % (σ/E). Since all energy corrections are charge dependent, the energy resolution for lower Z are less improved, e.g. staying at about 7 % for boron.

5 Analysis

In order to obtain results on these specific reaction channels, a complete identification of all reaction products is necessary. The detectors used for this have already been treated in chapters 3 and 4. In the first section of this chapter, it will be presented, how this information is used to identify the incoming carbon isotopes and the remaing fragments after the reaction.

The following sections will be used to introduce the analysis techniques used to investigate the experimental observables. There are three observables under investigation to deduce information about the internal structure of the nuclei: the momentum of the remaining fragment after the reaction, the energy of gamma rays emitted when the fragment deexcites after the reaction, and the reaction cross section, from which spectroscopic factors can be calculated. While the first of these quantities can be analysed using only the information obtained during the experiment, the analysis of the other two observables relies strongly on simulations of the detector response, which will also be explained.

5.1 Reaction Channel Identification

The first step is the incoming particle identification. A mix of different isotopes is delivered to the setup by the FRS, and only the carbon isotopes, which are supposed to be analysed, have to be selected. To do so, their charge, calculated from the energy loss in the in the PSP at the beginning of the setup ($\Delta E \propto Z^2$, see Sec. 3.2.1) and the mass-to-charge ratio (A/Z) is used. This ratio can be obtained from the magnetic rigidity of the FRS and the measured time-of-flight between the scintillators at S8 at the exit of the FRS and at the entrance of Cave C. Rearranging Eq. (3.1) yields

$$\frac{A}{Z} = \frac{B\rho}{\beta\gamma}. \tag{5.1}$$

Figure 5.1 shows the charge of the nuclei as a function their $\frac{A}{Z}$. One can clearly identify most light, neutron-deficient isotopes, from the proton-dripline to the valley of stability, up to a charge $Z = 9$. Although the $\frac{A}{Z}$-profile of the individual isotopes is complicated, the isotopes under investigation were selected using ellipitcal cuts. The two isotopes subject of this work, ^{11}C and ^{10}C, are indicated in the picture.

Similar to the incoming nuclei, the ougoing fragments are identified by their charge and mass. In this case, the charge is determined in several detectors, the two DSSDs behind the target and the TFW. This allows to not only to separate nuclei of different charges, but also to disentangle charge changing reactions in the target from breakup after the target. Figure 5.2 shows an example of the outgoing fragment charge identification. The energy loss in the TFW is shown as a function of the energy loss in the K-side of SST3, directly behind the target. The incoming isotope in this case was carbon, and the Crystal Ball reaction trigger (TPAT=8) was demanded, meaning that a knockout of a nucleon is likely

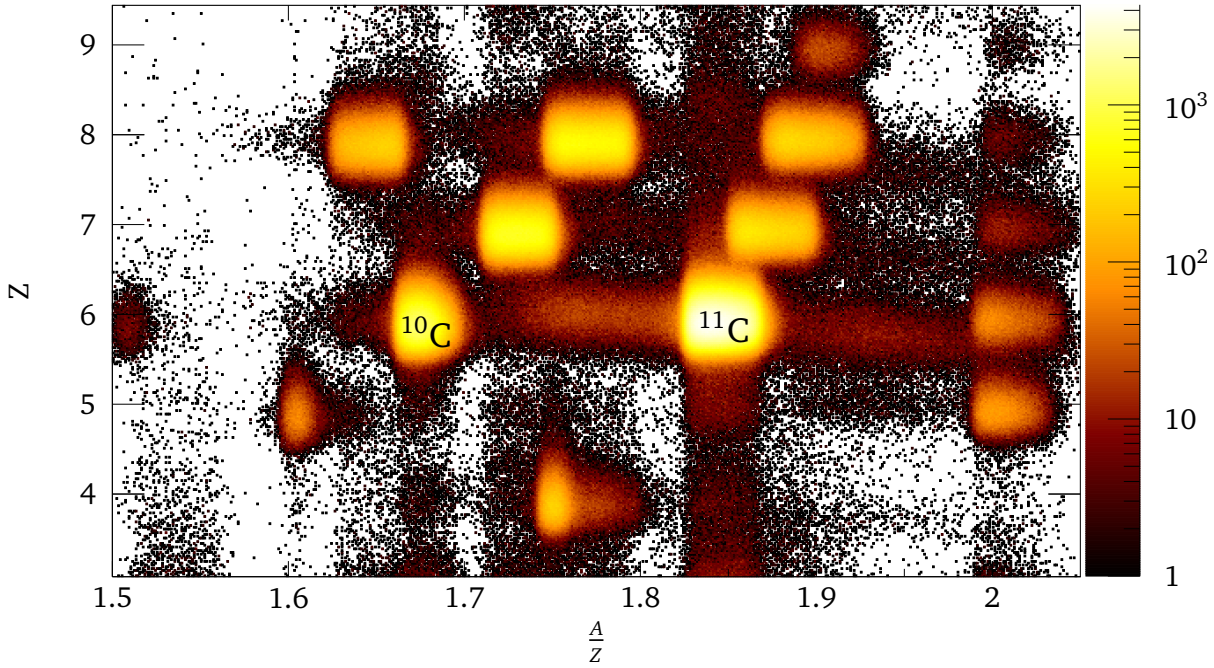

Figure 5.1: Identification plot for the incoming nuclei. The charge of the nuclei is plotted against their mass-to-charge ratio. The two isotopes subject of this work, ^{11}C and ^{10}C are indicated in the figure.

to have occurred. The different resulting elements are marked in the figure. On the diagonal one can see reaction products for which no (charge-changing) breakup occurred after the initial reaction. The fragments were selected by fitting Gaussian functions to the peaks in both the SST3 and TFW energy spectra, and taking all events within a distance of $2 \cdot \sigma$ from the mean.

With their charge identified, the mass of the outgoing particles as well as their momentum are determined via a tracking algorithm [47]. Once again use is made of the fact that charged particles are deflected in a magnetic field according to eq. 3.1. The tracker uses the measured positions from the DSSDs in front of the magnet and the fiber detectors behind it, together with the time-of-flight measured by the ToF-wall to calculate the path which the particles took through the magnetic field of ALADIN.

In this analysis, the 'forward tracking mode' was used, meaning that the particle positions and angles are taken from the DSSDs and the path is then tracked forward through the magnetic field of ALADIN. The $B\rho$ of the particles is then determined in an iterative process, guessing an initial $B\rho$ and then varying it until the measured and calculated positions on the fibre detectors and the time-of-flight match.

The information on ALADIN's magnetic field is taken from field maps, 3D matrices containing information about the magnetic field strength at any given point in the magnet. These field maps have been determined in the past for several currents running through ALADIN, and they are interpolated to get the exact value at the current used during the experiment.

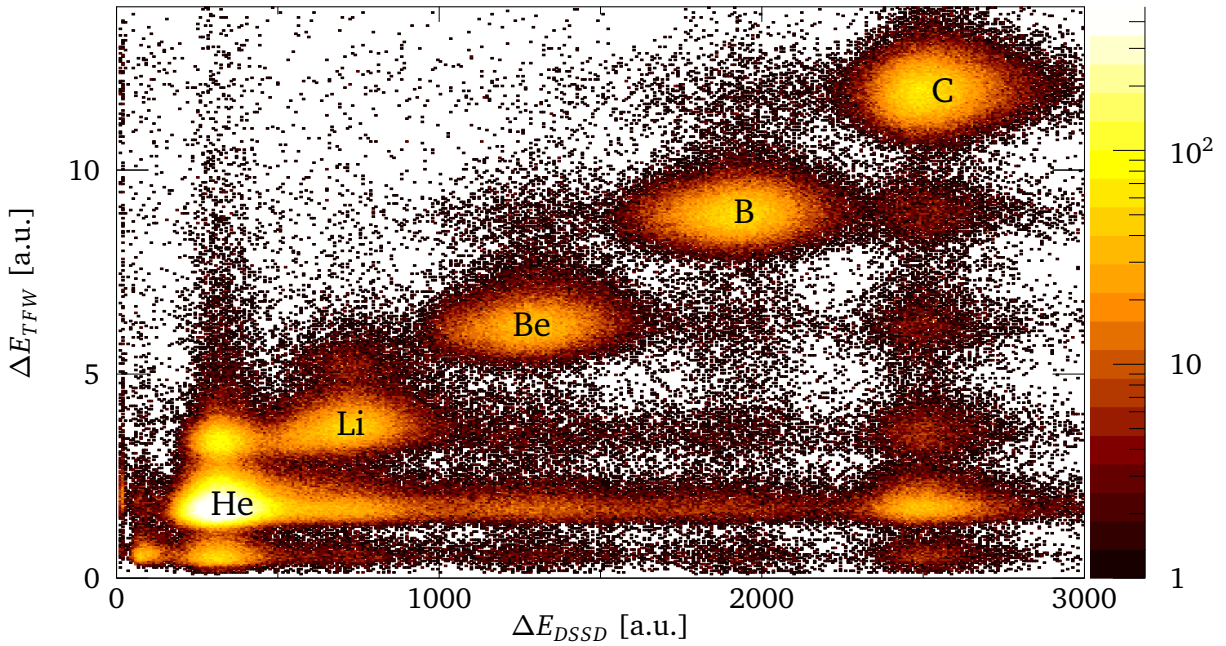

Figure 5.2: Charge identification of the fragments behind the target. The energy loss in the TFW is plotted against the energy loss on the K-Side of SST3. On the diagonal one can see reaction products for which no charge-changing breakup occurred after the initial reaction.

It is also important to know the exact position of the tracking detectors. Two methods were used to calibrate the detector positions. The rough adjustment was done using photogrammetric measurements. In a second step, the exact position was then calibrated using unreacted beam data. Since the $B\rho$ in this case is well known, this data can be used to determine the right corrections to the detector positions determined in the previous step. Another way to check the detector positions is to determine at the residuals of the position distributions, i.e., the difference between measured and calculated postions. If the detector positions are correct, the distribution of these residuals should peak at 0. In a similar way, a correction of the time-of-flight is determined by comparing the β of the unreacted beam before and after the target. For a correctly calibrated tracker, these two values are identical.

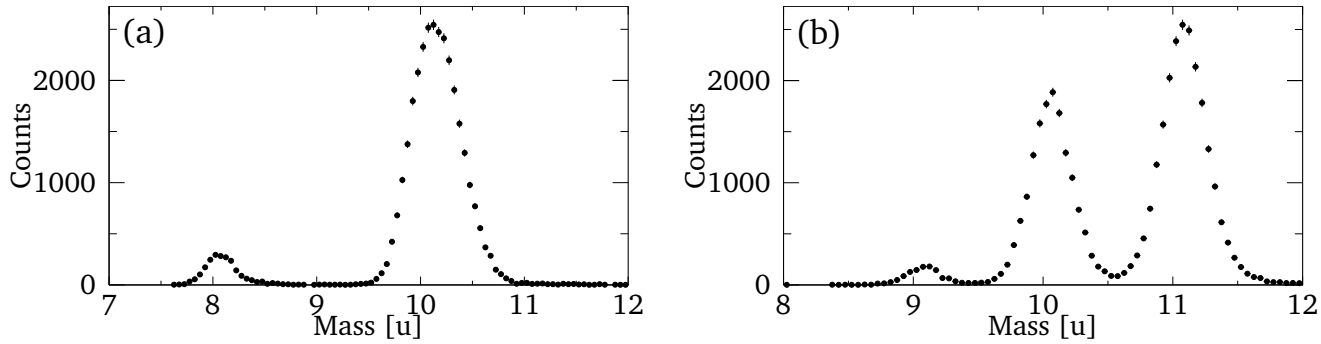

Figure 5.3: Mass spectrum for incoming ^{11}C, measured in coincidence the Crystal Ball trigger, (a) for outgoing boron ($Z = 5$), (b) for outgoing carbon ($Z = 6$). The knockout products of mass $A = 10$ can be clearly identified in both cases.

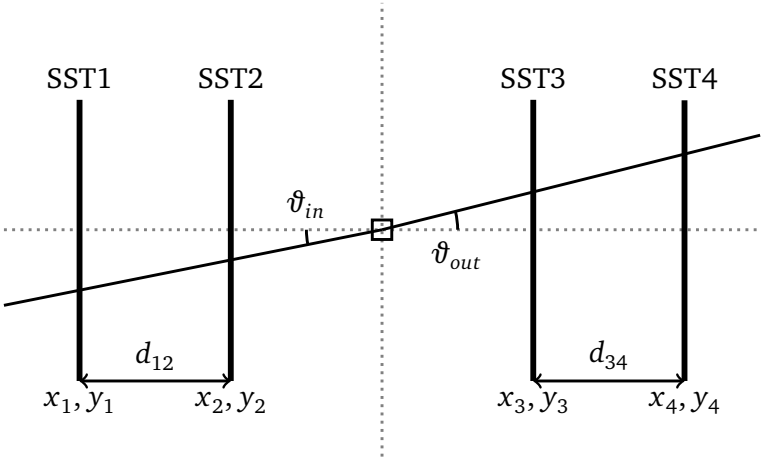

Figure 5.4: Illustration of the calculation of incoming and outgoing angle of the beam from the positions measured by the DSSDs.

Figure 5.3 shows the resulting mass spectra in coincidence with the detection of two nucleons in the Crystal Ball for two reactions, the quasi-free proton and neutron knockout from ^{11}C. Using these spectra, the reaction products were selected by fitting a Gaussian function to the peaks and taking an environment of $\pm 2 \cdot \sigma$ around the mean value. The obtained mass resolution is 1.8%, sufficient at these low masses.

5.2 Momentum Distributions

After determining the mass of the fragment, the tracker calculates the momentum p_{lab} of the fragments in the laboratory frame using

$$p_{lab} = \beta\gamma m \tag{5.2}$$

However, to deduce information about the internal structure of the nucleus, one needs to investigate the momentum in the center-of-mass frame, moving with the velocity v_0 of the beam. Since only the longitudinal component of the momentum changes when going to the center-of-mass frame, the two components have to be determined.

To calculate the transverse component of the momentum, the angles measured with the DSSDs in front of and behind the target are used. Figure 5.4 shows schematically of the in-beam DSSDs and the angles, which, in case of the x-direction, can be calculated using

$$\tan\vartheta_{in,x} = \frac{x_2 - x_1}{d_{12}}, \tag{5.3}$$

$$\tan\vartheta_{out,x} = \frac{x_4 - x_3}{d_{34}}, \tag{5.4}$$

$$\vartheta_{scatt,x} = \vartheta_{out,x} - \vartheta_{in,x} \equiv \vartheta_x, \tag{5.5}$$

with x_{1-4} being the x-positions measured by the DSSDs, and $d_{12,34}$ being the distance between the detectors in front of and behind the target. The calculation for the y-direction is done in the same way. The scattering angle $\vartheta_{scatt} \equiv \vartheta$ is the change of direction of the particle due to scattering in the target. With this angle, both components of the transverse momentum and therefore also the total transverse momentum can be calculated via

$$p_{x(y)} = p_{lab} \cdot \cos\vartheta_{x(y)}, \tag{5.6}$$

$$p_t = \sqrt{p_x^2 + p_y^2}. \tag{5.7}$$

From there, the calculation of the longitudinal momentum in the laboratory $p_{z,lab}$ is straightforward ($p_{z,lab} = \sqrt{p_{lab}^2 - p_t^2}$). The longitudinal and total momentum in the center-of-mass frame are calculated using

$$p_{z,cm} = \gamma_0(p_{z,lab} - \beta_0\gamma m), \tag{5.8}$$

$$p_{cm} = \sqrt{p_t^2 + p_{z,cm}^2} \tag{5.9}$$

where β_0 and γ_0 correspond to the velocity of the incoming beam, and γ to the speed of the fragment after the reaction.

5.3 Addback and Doppler Correction

The final step in the reaction identification is to decide whether a knockout was quasi-free or not. As described in Chapter 2, a strong indication of a quasi-free event is the detection of two coincident nucleons scattered to large angles. As mentioned before, such particles will be detected inside the Crystal Ball.

It is therefore important to disentangle the energy deposited in the Crystal Ball by nucleons or α-particles from the one deposited by photons. However, neither of these particles are likely to deposit their entire energy inside a single crystal, but rather in a cluster of neighbouring crystals. This can be either because the incoming particle itself travels through several crystals, or because secondary particles created through the interaction with the detector material carry some part of the energy to a neighbouring crystal. Therefore, in order to reconstruct the entire energy of each particle, an addback algorithm is used.

The algorithm works on an event-by-event basis by sorting each crystal with both an energy and a timing signal into a list according to the measured energy. It then starts with the first crystal in the list, i.e. the one with the highest deposited energy and determines whether the corresponding particle was a photon or a proton. If the crystal has a finite energy in the γ-branch, the cluster will be assigned to a photon, otherwise, if the γ-energy is in the overflow, and the proton-branch energy is finite, it will be assigned to a proton. The algortihm will then go to the list, add the energy of each crystal neighbouring

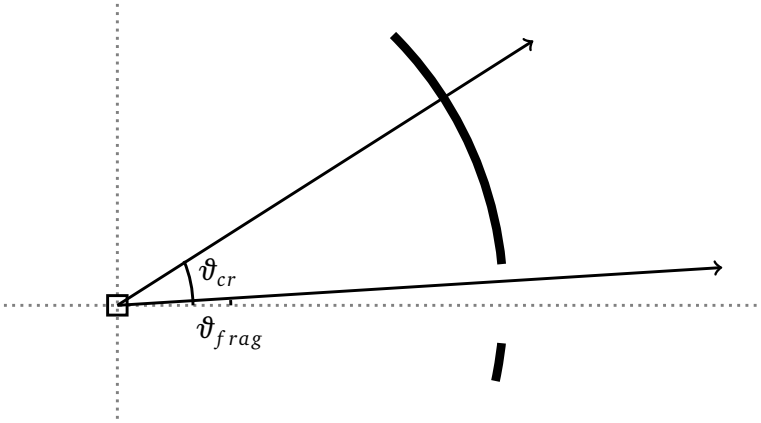

Figure 5.5: Illustration of the angles involved in the Doppler correction of the γ-rays emitted by the deexciting fragment. The angle of the fragment path in relation to the z-axis, ϑ_{frag} is usually much smaller than ϑ_{cr}, and can be neglected.

the initial one to the cluster energy, and remove that crystal from the list. Afterwards, it will again start at the top of the list of remaining crystals, creating a new cluster.

Two factors limit the accuracy of this approach. The first one is the assumption that the central crystal of the cluster is always the one in which the most energy was deposited, and that only direct neighbours contribute to the total energy. The second one is the uncertainty of the interaction of neutrons inside the detector. Since neutrons will deposit their energy mainly via nuclear interactions, it is possible that they don't saturate the γ-branch of a crystal, and therefore are wrongly indentified as photons.

Since the deexciting fragment travels at relativistic speeds when they emit the γ-rays, their energies have to be Doppler-corrected using the formula

$$E_{cm} = E_{lab}\gamma(1-\beta\cos(\vartheta_{cr}-\vartheta_{frag})). \tag{5.10}$$

The angles are explained in Figure 5.5. Here, ϑ_{frag} is the angle the fragment travels in relation to the z-axis, while ϑ_{cr} is the angle of the central crystal of the γ-cluster. Since usually $\vartheta_{frag} << \vartheta_{cr}$, Equation (5.10) can be simplified to

$$E_{cm} = E_{lab}\gamma(1-\beta\cos\vartheta_{cr}). \tag{5.11}$$

5.4 Simulation of QFS Events

The analysis of quasi-free scattering events relies strongly on simulations of the response of the Crystal Ball to both nucleons and γ-rays. These simulations are used to determine the efficiency of the detector and to disentangle the experimental γ-spectra.

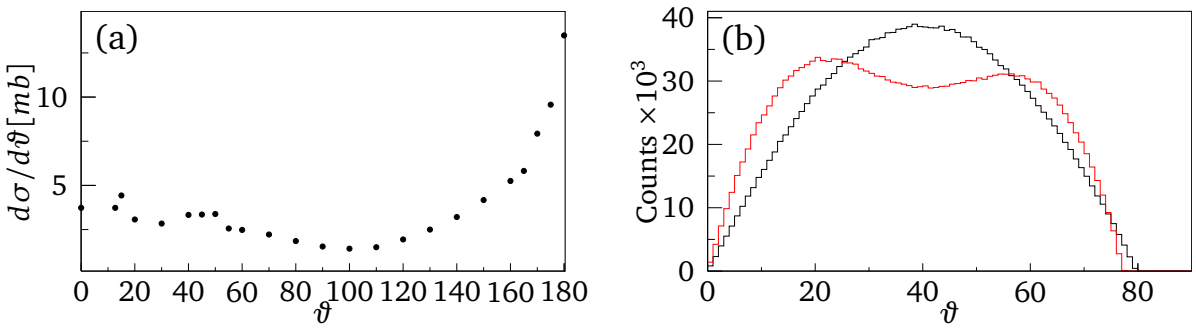

Figure 5.6: While for the (p,2p)-reaction a homogeneous distribution of protons is assumed, in case of the (p,pn) reaction the angular distribution was parametrized according to the experimental elastic p-n cross section, shown in figure (a) [48, 49]. (b) resulting polar angle distributions for (p,2p) (black) and (p,pn) (red) are compared.

The events used in these simulations were generated by a modified version of the QFS event generator developed by L. Chulkov and rewritten in C++ by V. Panin [12]. It generates events according to the basic principles outlined in Sec. 2.3. The program needs the beam energy and the mass of incoming and outgoing nucleus as input. Also, the momentum distribution of the outgoing fragment has to be given, which can be taken from theoretical calculations, e.g. ones as outlined in sec. 2.3 or, if such calculations are not available, assumed to be a Gaussian in which case the width has to be given.

In case of the (p,2p) and (p,pα) reactions, an isotropic distribution of the protons and α particles was assumed. In case of the (p,pn) reaction the angular distribution was parametrized according to the experimental elastic p-n cross section, seen in Figure 5.6(a) [48, 49]. In Figure 5.6(b) the resulting angular distributions for the (p,2p) and the (p,pn) reaction are compared.

A shortcoming of this event generator is that it does not include the effects of absorption of the scattered nucleons in the nuclear medium. In the case of low momentum transfer, the nucleons will have low kinetic energy, and the nucleon-nucleon cross section σ_{NN} will be high, leading to a high absorption probability. Low momentum transfer corresponds to the cases in which one nucleon will be scattered to low and the other one to high angles. Neglecting this effect leads to an underestimation of the detection efficiency and acceptance, since it leads to the assumption of a larger number of particles emitted under angles without coverage by the Crystal Ball. As becomes clear from Fig. 5.6(b), the detection efficiency will be more severely underestimated for the (p,pn)-reaction. Because of this, during the discussion of cross sections for these reactions in Chapter 6, values obtained assuming an isotropic distribution of neutrons and protons will also be given for comparison.

The generated events were written to ASCII files. These files were used as input for a second step of the event generation in which γ-transitions were added using another routine written by V. Panin. The routine added the different γ-cascades with probabilities according to their branching ratio. The γ-rays were assumed to be emitted isotropically in the rest frame of the fragment.

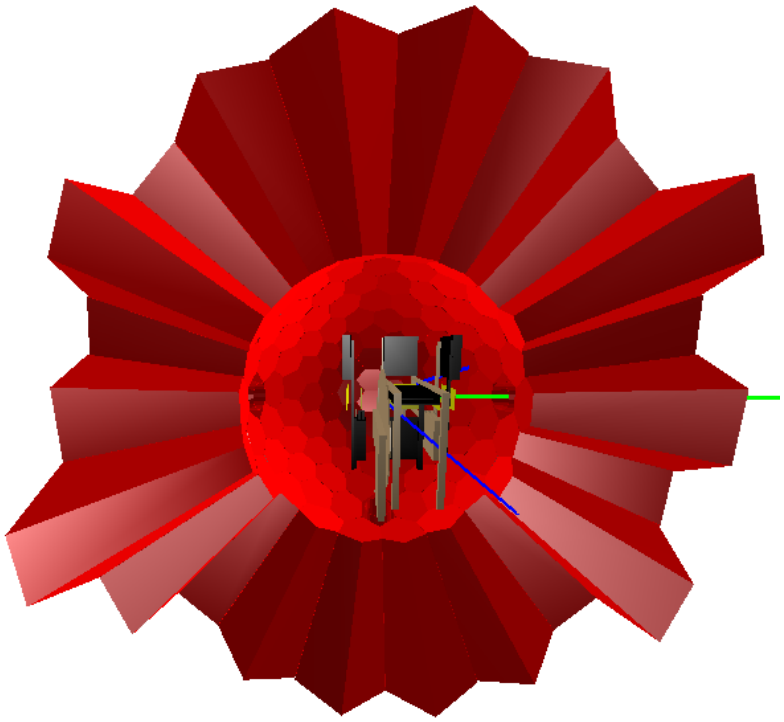

Figure 5.7: Typical (p,2p)-event simulated in r3broot. The crystals in the right hemispher ot the Crystal Ball as well as the vacuum chamber have been removed to show the interior, including the target wheel and the DSSDs with their electronics and holding structures. The two protons can be seen as blue tracks, the reaction fragment as green track.

The interaction of the particles with the Crystal Ball was then simulated using R3Broot, a simulation software package developed at GSI [50] based on root [44] and GEANT [51]. The model used in the simulations did not only include the target and Crystal Ball itself, but the entire target area including the target wheel and the DSSDs with their electronics and holding structures, etc. Figure 5.7 shows a typical (p,2p)-event in these simultations. The output of these simulations was then digitized and randomized to match the experimental resolution and written to root files before the same addback-routine as for the experimental data was used.

The Crystal Ball efficiency for the detection of quasi-free scattering was defined as the percentage of simulated QFS events for which the addback yielded nucleon multiplicity of two,

$$\epsilon_{XB} = \frac{N_{mul=2}}{N_{tot}}. \tag{5.12}$$

The obtained values vary from reaction to reaction not only because of the lower detection probability of neutrons inside the Crystal Ball but also since, due to the different characteristics of each crystal, they depend on the angular distributions of the QFS particles and therefore on the internal momentum. The exact values will therefore be given during the discussion of each reaction in Chapter 6.

5.5 Breakup Fragment Identification and Invariant Mass Technique

If the excitation energy of the fragment after the reaction is greater than the particle emission threshold, breakup will occur. This is likely to be the case after removal of a deeply bound nucleon. Since the isotopes unders study in this work are neutron-deficient, mainly the emission of protons or α-particles will play a role.

Since the used version of the tracking algorithm is not capable to track multiple light fragments, only the DSSD directly behind the target was used for the identification of the breakup fragments. Due to their fine segmentation, the DSSDs are the best suited detectors for distinguish multiple coincident fragments. The particle selection was done by creating energy spectra for the clusters of highest, second highest, etc energy on the K-side of SST3 and fitting Gaussians to the peaks corresponding to the breakup fragments. As usual, clusters with an energy difference of less than 2σ from the mean were considered.

The efficiency of this form of identification method for fragments with $Z > 1$ was estimated by comparing the number of detected particles on the K-side of SST3 and the TFW. The efficiency of SST3 can be calculated using,

$$\epsilon_{SST} = \frac{N_{SST3 \wedge TFW}}{N_{TFW}}, \tag{5.13}$$

where N_{TFW} is the number of events for which both fragments were detected and identified on the TFW, i.e. those events in which the two fragments hit differeten scintillator paddles, and $N_{SST3 \wedge TFW}$ is the number of nuclei identified by both detectors.

Since the detection of protons in the proton arm suffered from severe acceptance cuts, as is illustrated by the plot of the hit-distribution in x-direction of PDC1 in Fig. 5.8, SST3 was also used for proton identification. Using the subset of protons which hit the drift chambers, the proton efficiency was calculated using

$$\epsilon_p = \frac{N_{SST3 \wedge (PDC1 \wedge PDC2)}}{N_{PDC1 \wedge PDC2}}, \tag{5.14}$$

in which $N_{PDC1 \wedge PDC2}$ is the number of events with correlated hits in both drift chambers. For the emission of two protons, the efficiency to detect both was assumed to be $\epsilon_{2p} = \epsilon_p^2$. The values for both the fragment and the proton efficiency depend on the reaction, varying mainly with the number of fragments to be detected. In cases were this identification was used, it will be given in Ch. 6.

The excitation energy of the fragment before the breakup can be determined using the (Lorentz-) invariant mass M, which is defined as the square of the particles four momentum P

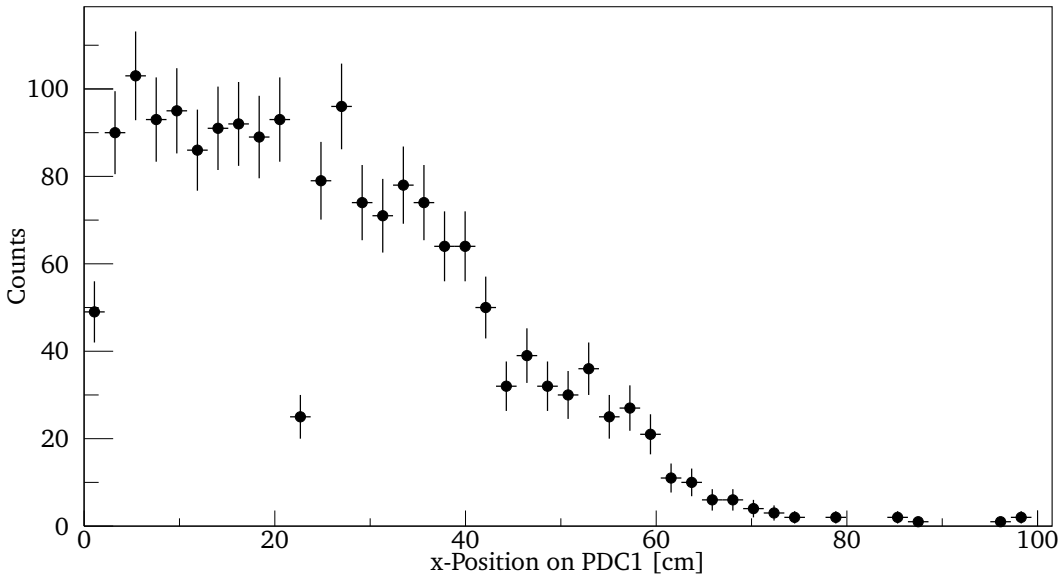

Figure 5.8: Acceptance cuts in proton arm. Shown is the x-position of the first proton drift-chamber for the case of proton emission from ^{9}Be.

$$M = P^2 = E^2 - p^2 = \left(\sum_i^N E_i\right)^2 - \left(\sum_i^N p_i\right)^2, \tag{5.15}$$

for an N-particle system. The convention $c = 1$ has been used. Using the relations $E_i = \gamma_i m_i$ and $p_i = \gamma_i \beta_i m_i$, the two sums in Eq. (5.15) can be Taylor-expanded, resulting in

$$E^2 = \sum_i^N \gamma_i^2 m_i^2 + \sum_{i \neq j}^N \gamma_i \gamma_j m_i m_j \tag{5.16}$$

$$p^2 = \sum_i^N \gamma_i^2 \beta_i^2 m_i^2 + \sum_{i \neq j}^N \gamma_i \gamma_j \beta_i \beta_j m_i m_j \cos\vartheta_{ij}, \tag{5.17}$$

with ϑ_{ij} being the opening angle between the fragments. At the same time, the invariant mass of the fragment before the breakup in its rest frame is its rest mass plus its excitation energy, $M = m_0 + E^*$. Requiring that the invariant mass of the system does not change during the breakup yields an expression for the excitation energy

$$E^* = \sqrt{\sum_i^N m_i^2 + \sum_{i \neq j}^N \gamma_i \gamma_j m_i m_k (1 - \beta_i \beta_j \cos\vartheta_{ij})} - m_0. \tag{5.18}$$

Table 5.1: Summary of the characteristics of the two targets used and the number of incoming carbon isotopes for each target. The combined uncertainty of ρ_T and d_T is assumed to be 2 %.

Target	ρ_t [g/cm^3]	d_t [mm]	A_T [g/mol]	^{11}C	^{10}C
Polyethylene	0.94	9.81	14.027	$7.6 \cdot 10^6$	$1.6 \cdot 10^6$
Carbon	1.84	5.08	12.011	$1.9 \cdot 10^6$	$4.1 \cdot 10^5$

Equation (5.18) uses the assumption that all participants of the breakup are produced in their ground state. To be more accurate, the energy of the γ-rays emitted by the reaction products can also be included. However, this was not done in the analysis presented here.

5.6 Calculating Cross Sections

The experimental cross section can be calculated using

$$\sigma = \frac{N_r/\epsilon_r}{N_t \cdot N_i/\epsilon_i}. \tag{5.19}$$

Here N_r is the number of reaction products, selected as described in the previous sections. N_i the number of nuclei incident on the target, which, due to the low reaction probability, can be approximated by the number of unreacted nuclei measured, i.e. carbon measured with the fragment trigger (TPAT=2) to include the acceptance of the fragment arm. The number of scattering centers in the target, N_t amounts to

$$N_t = \frac{\rho_T \cdot d_T \cdot N_A}{A_T}, \tag{5.20}$$

where ρ_T, d_T, and A_T are density, thickness and atomic mass of the target, while $N_A = 6.022 \cdot 10^{23}$ mol^{-1} is Avogadro's constant. Table 5.1 summarizes the characteristics of the two targets used in this analysis. The combined uncertainty of ρ_T and d_T is assumed to be 2 %. Also given in the table are the number of unreacted ^{10}C and ^{11}C nuclei measured with each target. These values have already been corrected for the downscaling of the fragment trigger (see Sec. 3.2.4).

In Eq. (5.19), $\epsilon_i \equiv \epsilon_{ID,i}$ is the detection efficiency for the unreacted beam, i.e. the probability to correctly identify it, while $\epsilon_r = \epsilon_{ID,r} \cdot \epsilon_{XB}$ is the detection probability of a quasi-free scattering reaction, meaning that the reaction fragment was correctly identified and both nucleons were detected in the Crystal Ball. Since for $Z \geqq 3$, the efficiency of charge identification and tracking is assumed to be close to 100 % and nearly identical for similar charges, $\epsilon_{ID,i} = \epsilon_{ID,r}$, in cases without breakup, only the Crystal Ball efficiency contributes, and Eq. (5.19) can also be written as

$$\sigma = \frac{N_r}{N_t \cdot N_i \cdot \epsilon_{XB}}. \tag{5.21}$$

The uncertainty of the cross section can be calculated using the quadratic sum of the errors associated with the variables,

$$\delta_\sigma = \sqrt{\delta_{N_r}^2 + \delta_{N_i}^2 + \delta_{N_t}^2 + \delta_{\epsilon_{XB}}^2}. \tag{5.22}$$

Except, for δ_{N_t}, only statistical uncertainties will be considered in Ch. 6. In order to arrive at the quasi-free scattering cross section, i.e. scattering on hydrogen, two sets of experimental data are investigated, one using the polyethylene (CH_2) target and one using the carbon target. The data using the carbon target is used as background measurement, not only to suppress the influence of the carbon atoms in the CH_2 target, but also the contributions from reactions not originating in the target. The hydrogen cross section is half of the difference between the cross sections measured with CH_2 and carbon,

$$\sigma_H = \frac{1}{2}\sigma_{H_2} = \frac{1}{2}(\sigma_{CH_2} - \sigma_C), \tag{5.23}$$

with an associated uncertainty

$$\delta_H = \frac{1}{2}\sqrt{\delta_{CH_2}^2 + \delta_C^2}. \tag{5.24}$$

Alternatively, the cross section for hydrogen can be obtained directly by Eq. (5.21), calculating the number of reactions on hydrogen using

$$N_{r,H} = \frac{1}{2} \cdot \left(N_{r,CH_2} - \frac{N_{i,CH_2}}{N_{T,C}} \frac{N_{T,CH_2}}{N_{i,C}} N_{r,C} \right). \tag{5.25}$$

6 Results

In this chapter, the results of the analysis of the following reactions will be presented

$$^{11}\mathrm{C(p,pn)}^{10}\mathrm{C}$$
$$^{11}\mathrm{C(p,2p)}^{10}\mathrm{B}$$
$$^{11}\mathrm{C(p,p}\alpha)^{7}\mathrm{Be}$$
$$^{10}\mathrm{C(p,pn)}^{9}\mathrm{C}$$
$$^{10}\mathrm{C(p,2p)}^{9}\mathrm{B}$$

In general, the results shown in the following were obtained following the analysis outline presented in chapter 5. Cases in which a different approach was taken will be specifically mentioned.

6.1 $^{11}\mathrm{C(p,pn)}^{10}\mathrm{C}$

From the point of view of a simple shell-model approach, the highest populated shell in the ground state of $^{11}_{6}\mathrm{C}_5$ is the p-shell with four protons and three neutrons. The binding energy of a proton or neutron in this shell is $S_p = 8.7$ MeV and $S_n = 13.1$ MeV, respectively. The isotopes investigated in this experiment were selected using the method described in section 5.1. They were incident on the target with an energy of $E \approx 325$ AMeV in the middle of the target, corresponding to a velocity $\beta \approx 0.67$.

The first reaction to be discussed is the quasi-free neutron knockout from this isotope. The Crystal Ball efficiency including acceptance in this case was determined to be $\epsilon = 11.1(3)$ %. With this value, and using Eq. (5.21), the cross sections for the CH_2 and carbon target were calculated to be $\sigma_{CH2} = 77.2(32)$ mb and $\sigma_C = 34.8(23)$ mb, respectively. Equation (5.24) yielded the QFS cross section, $\sigma_H = 21.2(20)$ mb.

Theoretical calculations of the kind described in Ref. [22] have been performed for a knockout of a neutron from the p-shell, yielding a theoretical cross section of $\sigma_{th} = 25.8$ mb [52]. Dividing this by the assumed number of neutrons in the p-shell gives the single-particle cross section $\sigma_{sp} = 8.6$ mb. Using these values, both the spectroscopic factor and the reduction factor can be calculated to be $C^2S = 2.47(23)$ and $R_s = 0.82(8)$.

In order to estimate the uncertainties due to the neglection of absorption effects in the kinematics code, the Crystal Ball efficiency was also determined under the assumption of an isotropic distribution of protons and neutrons. In this case, it is found to be $\epsilon = 14.4(4)$ %. The cross sections then become $\sigma_{CH2} = 59.5(23)$ mb, $\sigma_C = 26.8(17)$ mb, and $\sigma_H = 16.3(14)$ mb, the spectroscopic factor $C^2S = 1.89(15)$, and the reduction factor $R_s = 0.63(5)$.

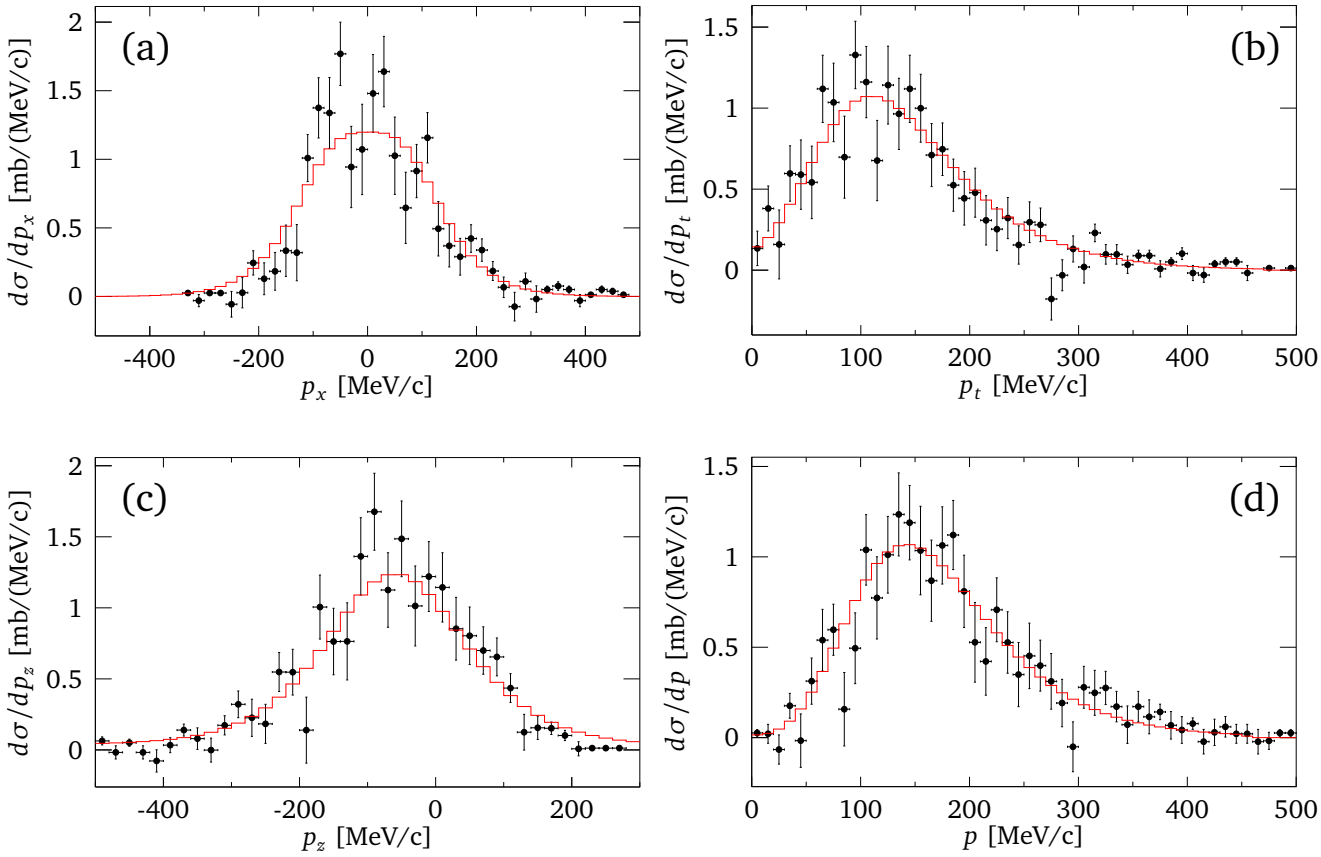

Figure 6.1: Momentum distributions obtained as described in section 5.2 for ^{10}C measured in coincidence with the detection of two nucleons in the Crystal Ball. (a) x-component of transverse momentum. (b) Transverse momentum. (c) Longitudinal momentum. (d) Total momentum. The experimental distributions are compared to theoretical ones calculated as described in Ref. [22] for a knockout from the p-shell. All distributions have been scaled so that their integral corresponds to the obtained experimental QFS cross section.

Figure 6.1 shows different momentum distributions obtained as described in section 5.2 for the ^{10}C reaction fragments in coincidence with the detection of two nucleons in the Crystal Ball. The experimental distributions are compared to theoretical ones calculated according to Eqs. (2.21) and (2.22) [22]. All distributions have been scaled so that their integral corresponds to the obtained experimental QFS cross section, and the theroretical distributions have been rebinned and convoluted with the experimental resolution, i.e. the momentum profile of the unreacted ^{11}C beam, as illustrated in Figure 6.2 for the y-component of the transverse momentum. Also, since the theoretical calculations do not reproduce the shift to lower longitudinal momenta, this distribution has been shifted in Fig. 6.1(c), so that the centroids of the two distributions match.

Experiment and theory agree very well, with the exception of a slight deviation for higher longitudinal momentum. This agreement implies that the p-shell knockout dominates the overall cross section for bound final states in ^{10}C, as is naively expected, however a contribution of the knockout from the s-shell cannot be excluded, due to its possibly similar width..

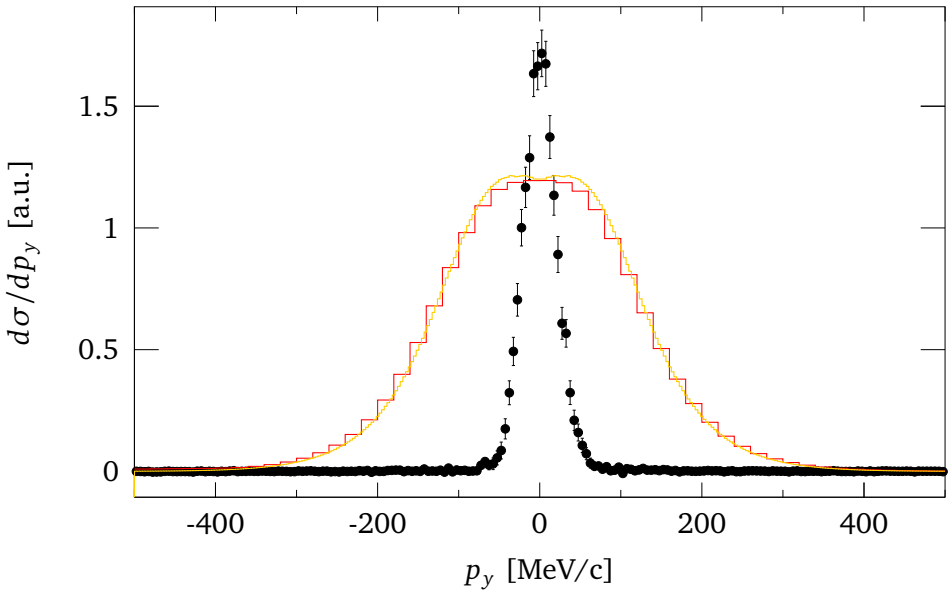

Figure 6.2: To take the detector response into account, the theroretical distributions (orange) were re-binned and convoluted with the experimental resolution, i.e. the momentum profile of the unreacted ^{11}C beam (black dots). The resulting distribution is shown in red.

Analyzing the γ-energy spectrum measured in coincidence with the reactions can give information about the excitation of the ^{10}C fragments after the reaction. ^{10}C has a single bound excited state at 3.35 MeV, as for higher excitation energies, (two-)proton emission will be more likely.

Figure 6.3 shows the energy spectrum, which has been corrected by subtracting the background due to reaction on carbon according to Eq. (5.25). In order to get the relative population of the excited state to the ground state, the simulated spectra for both states have been fitted to the experimental one.

Two measures were necessary to account for a mismatch between experiment and simulation. Both bin width and offset of the simulated spectra were taken as additional fit parameters. Also, since the simulations were found to underestimate the background at high energies an additional exponential background was added, whose height and exponent were also fitted. The result of the fit using six fit parameters had a reduced χ^2 of $\chi^2_{red} = 1.15$. After the fit, the population of the excited state n^* can be obtained using

$$N_r^* = N_{\gamma,int}\frac{N_{r,sim}}{N_{\gamma,sim}} \tag{6.1}$$

$$n^* = \frac{N_r^*}{N_r}, \tag{6.2}$$

with N_{int} being the integral of the fitted spectrum for the excited state, $N_{r,sim}$ the number of simulated events for this excited state, and $N_{\gamma,sim}$ the corresponding number of simulated γ-rays. It was found to be $n^* = 67(9)$ %, the cross section for knockout to this excited state is therefore $\sigma^* = 14.2(23)$ mb.

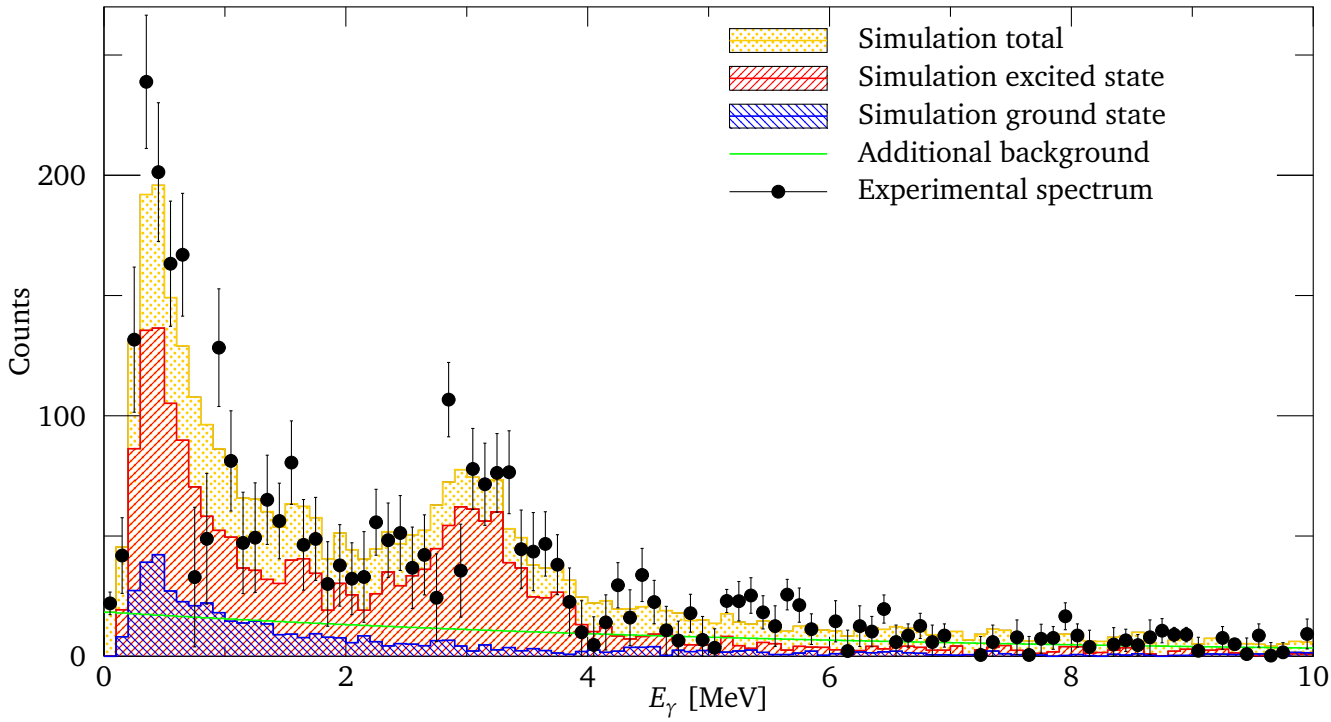

Figure 6.3: Analysis of the γ-energy spectrum measured in coincidence with ^{11}C(p,pn)^{10}C. Simulated spectra for both the ground and the excited state are fitted to the experimental one. An additional exponential background is assumed, and offset and bin width of the simulated spectra are fitted to account for a possible mismatch between experiment and simulation. The contribution of the excited state to the overall cross section is found to be 67(9) %

The one- and two-proton emission as well as the α-emission from^{10}C occur at similar excitation energies (3.8 MeV, 4.0 MeV, 5.1 MeV). However, all these breakups result in unbound nuclei (^{8}Be, ^{9}B, ^{6}Be). They are all detected as two α-particles in coincidence with two protons and were analysed together according to Sec. 5.5. The efficiency of the silicon detectors to detect the α-particles and the protons was $\epsilon_\alpha = 57(4)$ % and $\epsilon_p = 49(4)$ %, respectively. The resulting cross sections are $\sigma_{CH2} = 31.0(35)$, $\sigma_C = 11.9(25)$, and $\sigma_H = 9.6(21)$. However, it should be noted that, since the breakup of the intermediate nuclei can occur at excitation energies close to 0, the angle between the α-particles, and therefore their spatial separation on the SSTs, can be very small, so small that they cannot be identified as single particles. This issue will be discussed in more detail in connection to the proton removal from ^{10}C in section 6.5.

The case of the neutron emission of an excited ^{10}C fragment has also been invesigated. This was done by gating on identified ^{9}C in the fragment arm and demanding the LAND trigger for the detection of a neutron. However, after subtracting the carbon background ($\sigma_C = 0.61(25)$ mb) from the CH_2 measurement ($\sigma_{CH2} = 0.60(14)$ mb), no measured events remain. The upper limit for the QFS reaction amounts to $\sigma < 0.28$ mb.

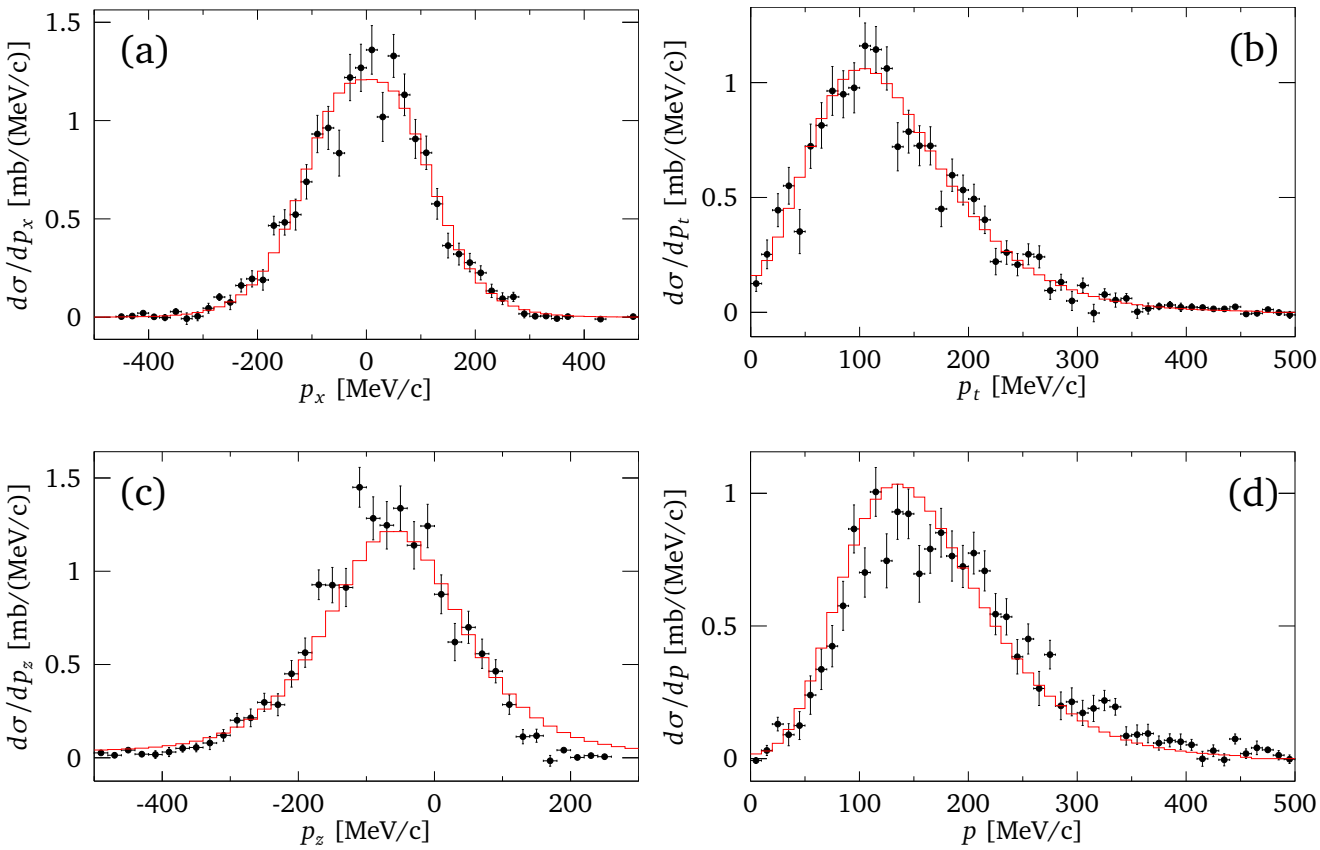

Figure 6.4: Momentum distributions for the ^{10}B reaction fragments in coincidence with the detection of two nucleons in the Crystal Ball, again compared to calculations for a p-shell knockout. (a) x-component of transverse momentum. (b) Transverse momentum. (c) Longitudinal momentum. (d) Total momentum.

6.2 ^{11}C(p, 2p)^{10}B

The next investigated reaction is the proton knockout from ^{11}C. In this case, the Crystal Ball efficiency is $\epsilon = 55.8(7)$ %, leading to cross sections of $\sigma_{CH2} = 56.3(15)$ mb and $\sigma_C = 21.6(8)$ mb and $\sigma_H = 17.3(8)$ mb, again using Eqs. (5.21) and (5.24). The theoretical cross section in this case is $\sigma_{th} = 32.0$ mb [52], the single-particle cross section, obtained by dividing by the number of protons in the p-shell, $\sigma_{sp} = 8.0$ mb. This leads to a spectroscopic factor of $C^2S = 2.16(10)$ and a reduction factor of $R_s = 0.53(2)$.

Figure 6.4 shows the different momentum distributions for the ^{10}B reaction fragments in coincidence with two nucleons. Again the experimental distributions are compared to theoretical calculations for a knockout from the p-shell and found to agree well. The deviation for higher longitudinal momenta appears stronger for this reaction. Again, while the knockout from the s-shell cannot be excluded, the good agreement between experiment and calculation implies that it only plays a minor role for the bound states of ^{10}B.

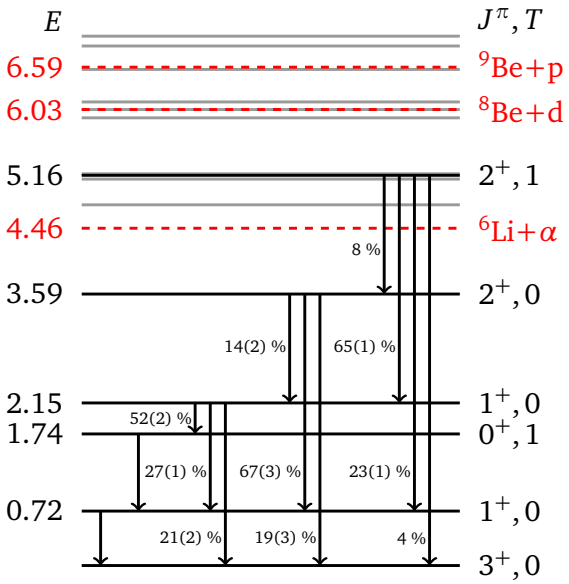

Figure 6.5: Energy levels, γ-branching ratios, and particle emission thresholds of ^{10}B [53].

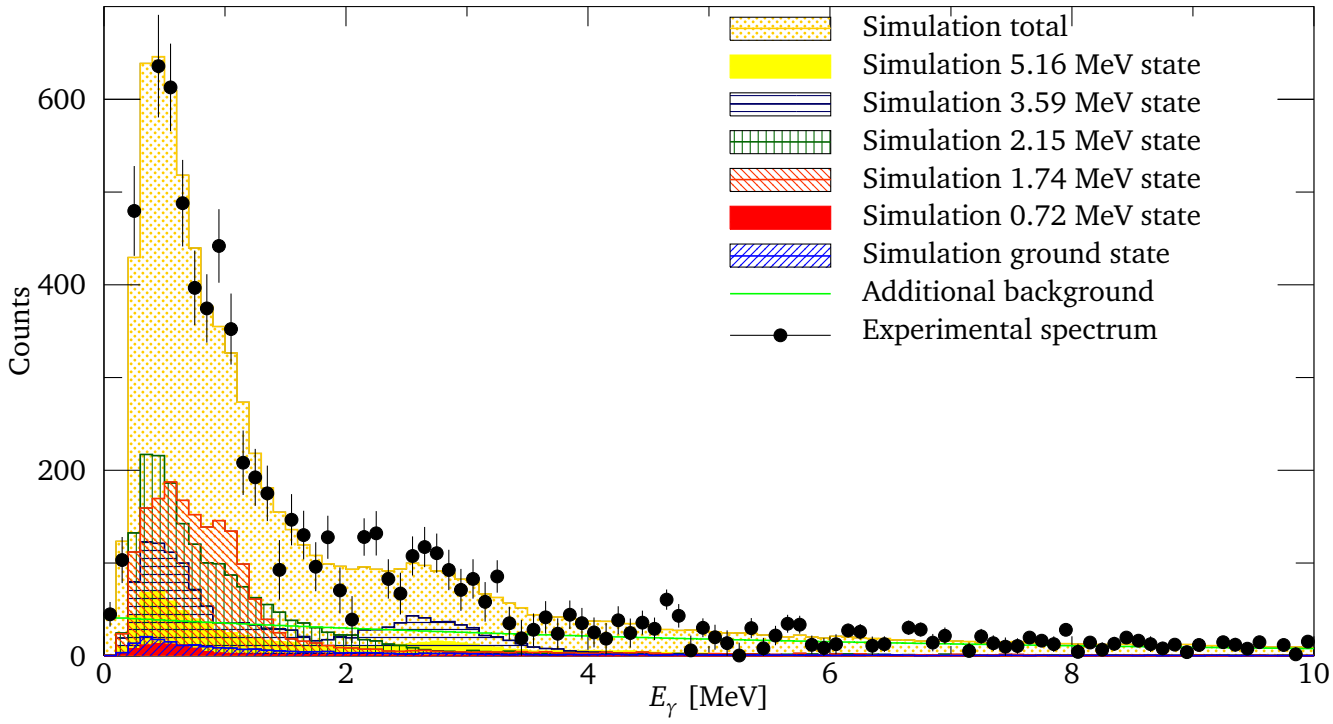

Figure 6.6: Analysis of the γ-energy spectrum measured in coincidence with ^{11}C(p,pn)^{10}C. The excited states have been assumed to decay via the γ-cascades shown in Fig. 6.5. Because of the many states contributing, the fit is quite complicated in this case.

Table 6.1: Obtained populations for the excited states of ^{10}B

E [MeV]	n [%]	σ [mb]]
0.72	< 10	< 1.7
1.74	20(5)	3.4(10)
2.15	18(8)	3.1(14)
3.59	15(6)	2.6(10)
5.16	< 13	< 2.2

The analysis of the γ-spectrum of the produced ^{10}B was attempted as well. The energy levels of ^{10}B are shown in Fig. 6.5 alongside the γ-branching ratios and the particle emission thresholds. It has four excited state below the particle threshold and one slightly above the α-threshold which mainly decays via γ-transistions since the α-decay is isospin forbidden, all of which are single-particle states [53]. Also, the lowest excited state is very long-lived ($T_{1/2} \approx 0.7$ ns) which means that it will not decay inside the target. Consequently the Doppler correction will be distorted and the detection efficiency will be lowered.

Figure 6.6 shows the result of the fit of the simulated spectra to the background subtracted experimental spectrum. In order to reduce the number of fit parameters, offset, bin width and the exponent of the exponential background were assumed to be the same as in case of the (p,pn)-reaction, leaving the height of the 6 simulated spectra and the exponential background as fit parameters. The fit had a reduced χ^2 of $\chi^2_{red} = 1.20$, the resulting populations of the different states are summarized in table 6.1. Due to the large number of states involved in the fit and uncertainties of the branching ratios, the uncertainties are quite large.

Two of the possible breakup channels of an excited ^{10}B nucleus were investigated, ^{10}B$\rightarrow^{6}$Li+α, and ^{9}Be+p. The remaining channels cannot be properly distuingished from the breakup of ^{10}C (^{10}B$\rightarrow^{8}$Be+d,^{10}B$\rightarrow^{9}$B+n), or from ^{7}Be produced in (p,pα) and were not analysed.

Figure 6.7 shows the identification of the α-emission channel, ^{6}Li+α. SST3 was used to identify coincident helium and lithium. A small contribution from ^{7}Li+^{3}He cannot be excluded, however it is expected to play only a minor role, due to its high threshold. The efficiency of the silicon detectors to detect the fragments was $\epsilon_{SST} = 69$ %. The resulting cross sections are $\sigma_{CH2} = 12.9(6)$ mb, $\sigma_C = 4.5(4)$ mb, and $\sigma_H = 4.2(3)$ mb.

The excitation energy of the ^{10}B nucleus before the breakup was reconstructed using the invariant mass technique. The resulting energy spectrum is shown in Fig. 6.8(a). Most strength is concentrated at energies $E^* < 6$ MeV. Four states have been observed in this energy region. Apart from the state at 5.16 MeV, which was already considered in the analysis of the γ-spectrum and whose α-decay is isospin forbidden, these are states at 4.77 MeV, 5.11 MeV, and 5.18 MeV. However, while there are possibly peaks visible slightly above and below 5 MeV the resolution is not sufficient and the statistics are too low to clearly resolve them.

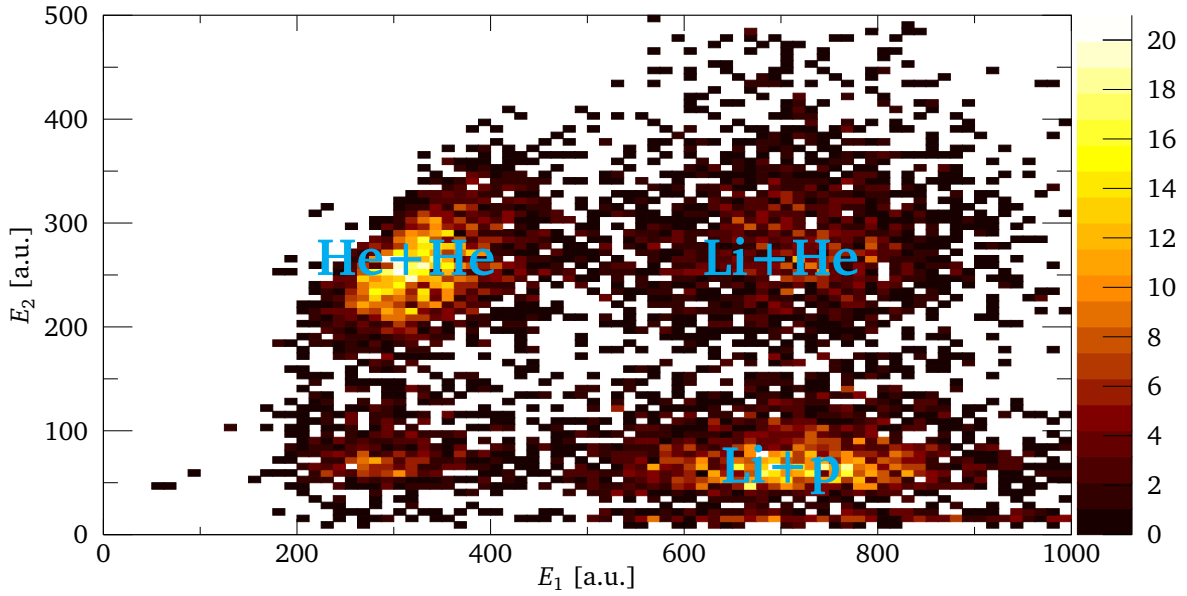

Figure 6.7: Identification of the breakup of ^{10}B into ^{6}Li + α. Plotted is the energy of the cluster with the second-highest energy, E_2 against the highest cluster energy E_1. The identification is done according to section 5.5. The events corresponding to ^{6}Li + α are indicated in the figure. A small contribution from ^{7}Li+^{3}He cannot be excluded, however it is expected to play only a minor role.

In case of the proton emission from an excited ^{10}B reaction fragment, there is only one heavy fragment after the breakup (^{9}Be). The beryllium is therefore identified via tracking, and SST3 is used to identify the protons. A proton efficiency of $\epsilon_p = 75(5)$ % is obtained, and the caclulated cross sections are $\sigma_{CH2} = 3.8(3)$ mb, $\sigma_C = 1.4(2)$ mb, and $\sigma_H = 1.2(2)$ mb. Figure 6.8(b) shows the excitation energy spectrum in this case. It should be noted however, that the protons were assumed to travel with the same velocity as the fragment. Their real velocity distribution can be substantially broader, so that Fig. 6.8(b) should only be seen as an estimate.

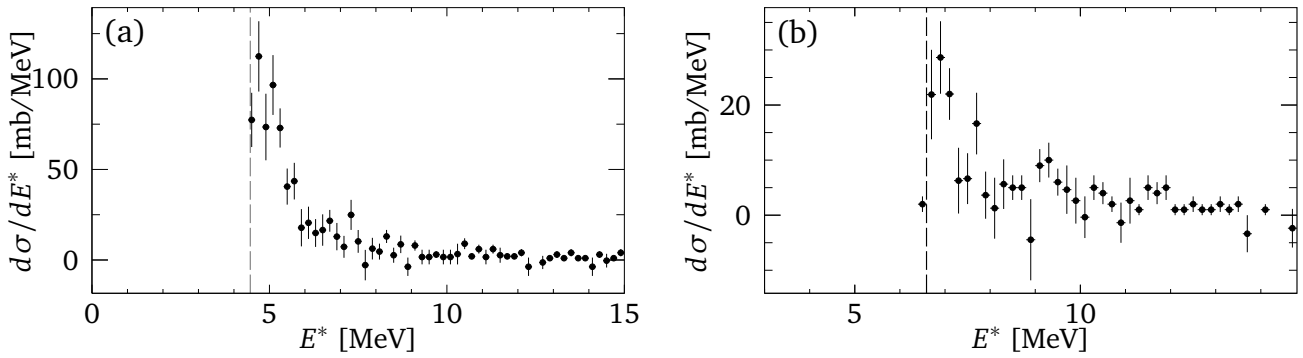

Figure 6.8: Excitation energy of ^{10}B above the particle threshold, reconstructed with the invariant mass method. (a) ^{6}Li+α. (b) ^{9}Be+p. The particle threshold is indicated in both pictures. In both cases it was assumed, that both particles travel with the velocity of the excited ^{10}B after the breakup.

6.3 ^{11}C(p, pα)^{7}Be

The α-removal from ^{11}C has also been studied. The efficiency of the crystal ball in this case is larger, due to the higher energy deposition of the α-particles compared to protons or neutrons, however, this is slightly offset by a lower acceptance, since a significant part of the α-particles will be scattered to polar angles smaller than 8°.

This is illustrated in Fig. 6.9, in which the polar angles generated by the event generator described in section 5.4 are compared to results of the addback algorithm for a r3broot simulation and a experimental data, measured with the CH_2 target. Although the background due to reactions on carbon in Fig. 6.9(c) is large, the slight enhancement of events with ϑ_1 can be seen as an indication for the occurence of quasi-free (p,pα).

The resulting efficiency is $\epsilon = 66.2(8)$ %. This leads to cross sections of $\sigma_{CH2} = 21.7(6)$ mb, $\sigma_C = 10.2(5)$ mb, and $\sigma_H = 5.8(4)$ mb. These values are surprisingly large, the same order of magnitude as the proton or neutron knockout, which might be an indication of a preformed α-particle in ^{11}C. There might be contributions from the breakup of high-lying excited states in ^{10}B and ^{10}C following the proton or neuton knockout. However, these decays only occur at very high excitation energies and their contributions are therefore assumed to be small. In this case, no theoretical calculations are available to compare the obtained cross sections.

^{7}Be has a single bound excited state at 400 keV. However, since this is exactly in the energy region of the highest background, and close to the threshold energy of the Crystal Ball γ-branch, no attempt to disentangle this from the ground state was made.

6.4 ^{10}C(p, pn)^{9}C

The second isotope presented here is ^{10}C, consisting of six protons and four neutrons. The last populated shell in the ground state is the p-shell with four protons and two neutrons. The binding energy of a proton or neutron from this shell is $S_p = 4.0$ MeV and $S_n = 21.3$ MeV, respectively. The isotopes investigated in this experiment were selected using the method described in section 5.1. They were incident on the target with an energy of $E \approx 385$ AMeV, corresponding to a velocity of $\beta \approx 0.71$.

For a quasi-free knockout of a neutron from this isotope, the same analysis as for the knockout-reactions from ^{11}C has been done. Figure 6.10 shows the momentum distributions of the ^{9}C reaction fragments. Again, the agreement between experiment and theory is good.

The Crystal Ball efficiency in this case was determined to be $\epsilon = 12.4(4)$ %, the cross sections for the CH_2 and carbon target were calculated to be $\sigma_{CH2} = 72.2(39)$ mb and $\sigma_C = 32.8(39)$ mb. The QFS cross section, $\sigma_H = 19.7(28)$ mb, was compared to the theoretical cross section for a p-shell knockout, $\sigma_{th} = 18.9$ mb, leading to $\sigma_{sp} = 9.5$ mb, $C^2S = 2.09(30)$ and $R_s = 1.04(15)$.

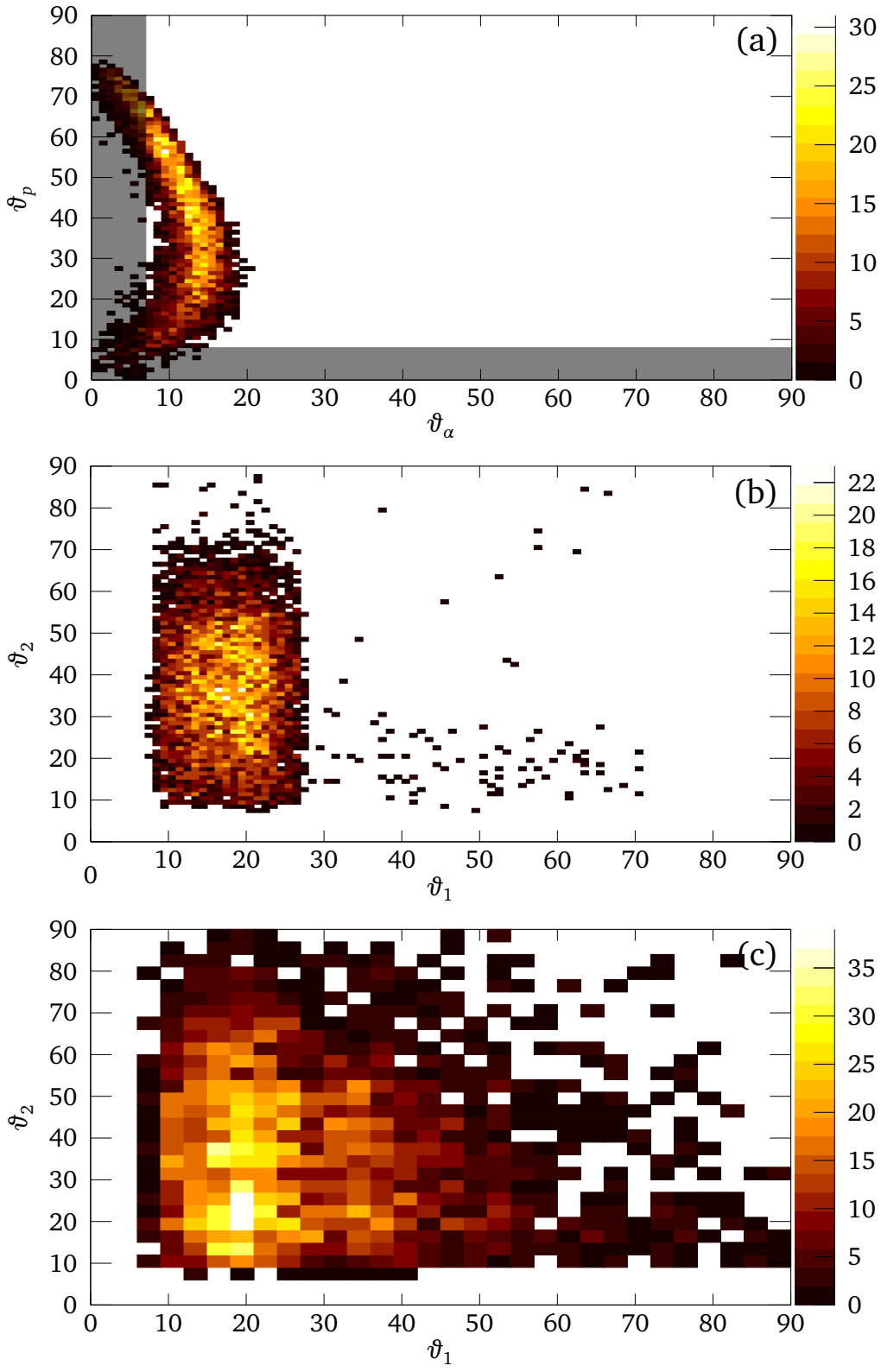

Figure 6.9: Correlation plot of the polar angle ϑ of proton and α-particle. (a) Output of the event generator. The shaded region is outside of the acceptance of the crystal ball. (b) Simulated Crystal Ball response after the addback algorithm. (c) Measured distribution with a CH_2 target. The distribution shows a strong uncorrelated background due to the carbon component of the target, but an enhancement at for low ϑ_1 is visible, indicating the occurence of (p,pα).

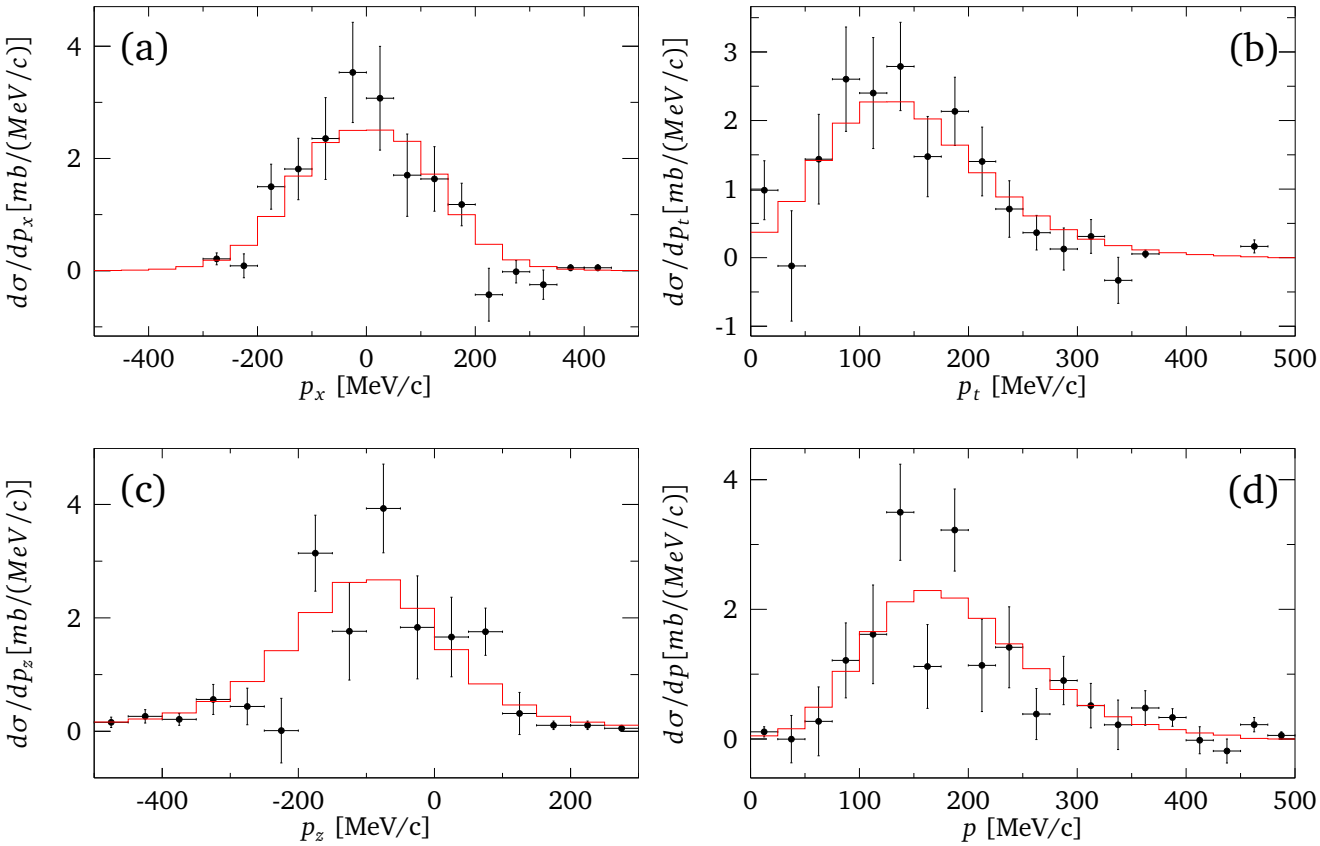

Figure 6.10: Momentum distributions for the ^{9}C reaction fragments in coincidence with the detection of two nucleons in the Crystal Ball. (a) x-component of transverse momentum. (b) Transverse momentum. (c) Longitudinal momentum. (d) Total momentum.

Assuming an isotropic distribution of protons and neutrons, leading to an efficiency of $\epsilon = 15.4(4)$ %, the cross sections then are found to be $\sigma_{CH2} = 58.2(31)$ mb, $\sigma_C = 26.4(31)$ mb, and $\sigma_H = 15.9(22)$ mb, the spectroscopic factor is $C^2S = 1.68(24)$, and the reduction factor $R_s = 0.84(12)$.

In this case, two possible breakups of the ^{9}C fragment were considered ^{9}C→^{8}B+p and ^{9}C→^{7}Be+2p. Most remaining channels involve the emission of a neutron or a compound involving a neutron (d,t), which is unlikely due to the strong neutron deficiency of ^{9}C. These breakups would also go beyond the proton dripline and would be detected as one α particle and several protons, making the detection efficiency extremely low.

Since in both reaction channels only one nucleus should appear in the fragment arm, the identification via tracking was used, as for the bound states. The protons were identified using SST3, cutting on the energy of the second and third cluster on the K-side. The efficiency for the detection of one proton was found to be $\epsilon_{1p} = 65(8)\%$. Since only very few events with proton multiplicity 2 were identified, the effciency was approximated by $\epsilon_{2p} = \epsilon_p^2 = 42(5)\%$. The resulting QFS cross sections are $\sigma_H = 6(2)$ mb for the 1p-channel and $\sigma_H = 23(7)$ mb for the 2p-channel.

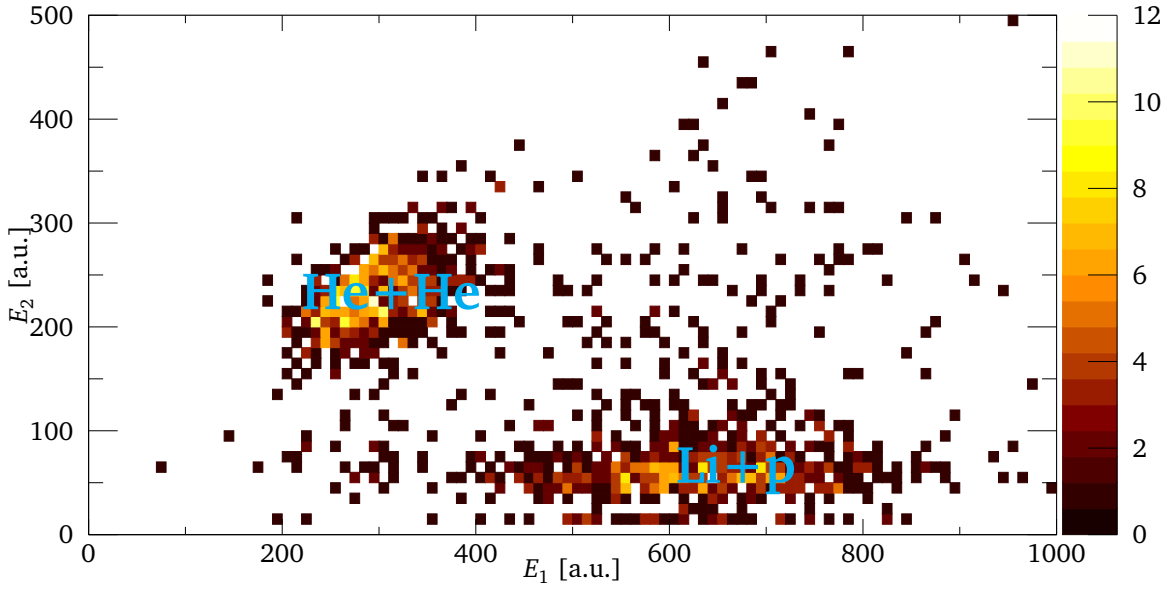

Figure 6.11: Identification of two coincident α-particles for the breakup of ^{9}B into 2α+p. Plotted is the energy of the cluster with the second-highest energy, E_2 against the highest cluster energy E_1. The identification is done according to section 5.5. The events corresponding to 2α are indicated in the figure. Also are events identified as lithium in coincidence with a proton. A large fraction of the lithium in these events is expected to be due to two coincident α-particles as well, misidentified due to small spatial separation on the detector.

While these values seem surprisingly large, they are consistent with the large population of the first excited state of ^{10}C produced in ^{11}C(p,pn)^{10}C. The much larger observed cross section for ^{9}C→^{7}Be+2p can be partly explained by the fact that a fraction of it has been in created in sequential decays via ^{8}B. In a cluster picture of the nucleus, this larger cross section could also be seen as a sign that the ground state of ^{10}C more closely resembles the state ^{8}Be + 2p than ^{9}B+p, i.e. a strong clustering. However, this is in contradiction to observations made in decay studies at lower energies. In ^{10}C(p,n)^{10}B at 1.7 *A*MeV the cross section for a sequential decay via ^{9}B was found to be an order of magnitude higher than for a direct 2p-decay [54, 55]. In fragmentation of ^{12}C at 33 *A*MeV, the cross section for the ^{9}B+p-decay of ^{10}C was found to be a factor 3-4 higher than the one for ^{6}Be+α [56, 57].

6.5 ^{10}C(p, 2p)^{9}B

Since the reaction residue ^{9}B is unbound, decaying into two α-particles and a proton (via ^{8}Be+p), the alternative fragment ID using SST3 was used. This is illustrated in Fig. 6.11. The efficiency to detect the two α-particles was found to be $\epsilon_{2\alpha} = 58(3)$ %, the efficiency for the additional detection of a proton $\epsilon_p = 70(4)$ %. Together with a Crystal Ball efficiency of 58.8(8) %, this leads to cross sections $\sigma_{CH2} = 30(3)$ mb, $\sigma_C = 15(2)$ mb, and $\sigma_H = 7(2)$mb.

The apparent low cross section is due to acceptance cuts in the detection of the α-particles, which already have been mentioned in Sec. 6.1. Figure 6.12(a) shows the excitation energy of the ^{8}Be nuclei produced by proton emission from ^{9}B, reconstructed from the invariant mass of the two measured α-particles. Most beryllium is found in the ground state, i.e. at excitation energies close to 0 MeV.

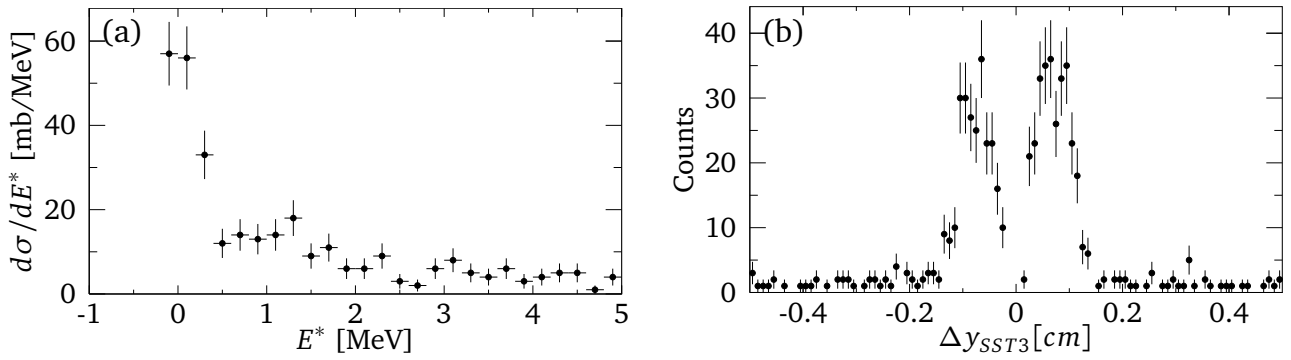

Figure 6.12: Acceptance cuts in the detection of ^{8}Be. (a) E^* of ^{8}Be, reconstructed from the two detected α particles. The spectrum features a peak at very low energies, corresponding to small relative angles between the α-particles. (b) distance of the two αs on the K-side of SST. The rapid drop for $\Delta y < 500\mu$m indicates acceptance losses.

However, as Eq. (5.18) shows, such low energies correspond to small angles between the two particles, and therefore also to a small spatial separation on the silicon detectors. It can therefore lead to the two particles to be detected as one. To illustrate this, Fig. 6.12(b) shows the distance of the two αs on the K-side of SST3. There is a rapid drop for distances of 500-600 μm, corresponding to the average combined width of two strip clusters caused by α-particles.

This observation can also explain the apparent large abundance of lithium in Fig. 6.11, which cannot be produced in a simple direct reaction or in a breakup of either ^{9}B or ^{9}C. To get a better estimate of the ^{10}C(p,2p) cross section, these events have assumed to be largely two α-particles as well. The resulting cross sections are $\sigma_{CH2} = 42(4)$ mb, $\sigma_C = 22(3)$ mb, and $\sigma_H = 9(3)$ mb. However, it is clear that a more detailed analysis is needed to arrive at a reliable value.

6.6 Discussion

To put the results presented in this chapter in relation to previous measurements, Fig. 6.13 shows the reduction factor R_S as a function of the difference in nucleon binding energies, once again. The reduction factors from the current analysis have been added to Fig.2.2.

While the value obtained in ^{11}C(p,2p) agrees well with the previously observed trend, the two values obtained in (p,pn) deviate considerably. Their large values would indicate that not only the dependence of quenching on nuclear binding energy asymmetry is not observed in quasi-free (p,pn)-reactions, but also the quenching in total is smaller than observed in (e,e'p). Future analysis has to show to what extent this is a real feature of quasi-free scattering, and how strongly this result is distorted, e.g., by the neglection of absorption effects in the calculation of the nucleon detection efficiency of the Crystal Ball. The need for further investigations becomes also apparent by the large deviation between the values obtained under the assumption of isotropic and anisotropic angular distributions of the knocked-out nucleons.

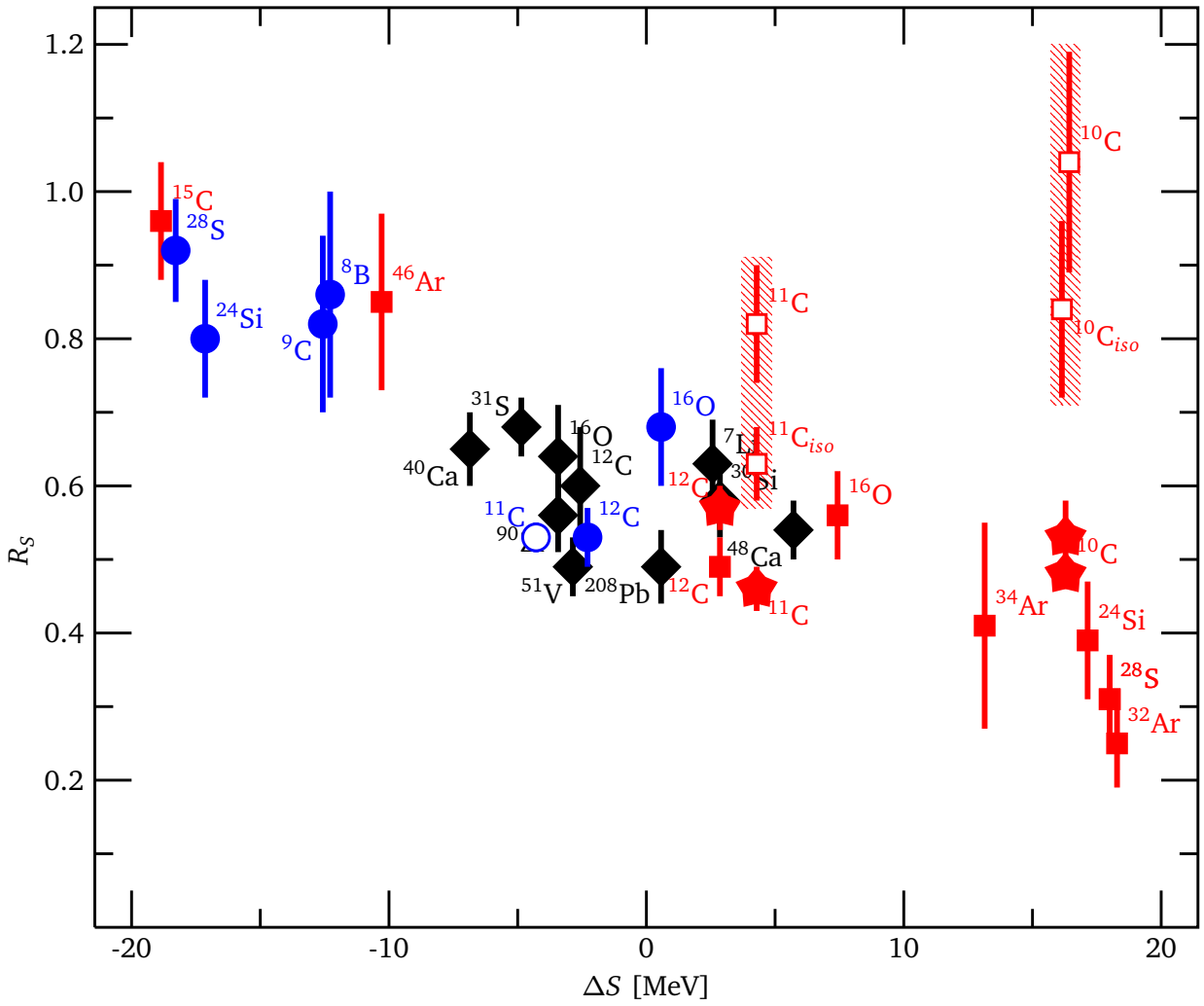

Figure 6.13: Reduction of spectroscopic factors as a function of the difference in nucleon binding energy ΔS [7]. The reduction factors obtained in this work have been added to Fig. 2.2. Shown are the old results for electron scattering (black diamonds), proton-knockout (blue circles), and neutron-knockout(red squares), and the newly obtained values for (p,2p) (open circle) and (p,pn) (open squares). In the case of (p,pn), the values obtained assuming both an anisotropic and a isotropic distribution of the knocked out nucleons are shown.

The measured momentum distributions of the surviving ^{9}C,^{10}C and ^{10}B agree very well with calculations for a p-shell knockout following Ref. [22]. This demonstrates that the framework combining DWIA and eikonal reaction theory described in Ref. [22] is capable of describing QFS for nuclei in this mass region.

The strong population of the low-lying bound excited states, obtained in the analysis of the γ-energy spectra measured in coincidence with ^{11}C(p,pn)^{10}C and ^{11}C(p,2p)^{10}B is surprising. A possible explanation is a strong contribution of particle-hole states to the ground state of ^{11}C. For the one-proton and two-proton emission following ^{10}C(p,pn)^{9}C, whose threshold energy is comparable to the energy of the bound states in ^{10}B and ^{10}C, large cross sections have been obtained as well.

The analysis of knockout to unbound states also shows most strength concentrated at low excitation energies close to the breakup thresholds, implying little contribution of the s-shell knockout. However, the results of these reactions suffer from acceptance cuts for both the fragments and the protons. A more detailed analysis using similar tracking for the protons as for the fragments as well as simulations of the detector response of both the fragment and the proton arm could lead to a better undestanding of these reactions.

7 Development and Testing of New Frontend Electronics for DSSD Prototypes

Silicon detectors represent the most common semiconductor detector type for charged particles. They are produced by bringing silicon doped with acceptor impurities (p-type) in contact with silicon doped with donor impurities (n-type), thus forming a junction [58]. The higher concentration of conduction electrons on the n-side causes a net diffusion of the electrons into the p-type region leaving immobile positive ions behind. The same effect causes holes on the p-side to diffuse to the n-side. This creates an electric field between the two regions. The diffusion stops when the electric field is strong enough to prevent further net diffusion and an equilibrium is reached. The region in which this charge difference exists is called the depletion region, and it is the active volume of the detector. In this region the concentration of electrons and holes is greatly suppressed. For most detectors, an external voltage is applied in a way that it increases the potential difference between the two sides of the junction. This is called reverse biasing. It leads to a stronger electric field, which in turn causes the particles to move more rapidly, and makes a more complete charge collection possible. Applying a reverse bias also makes the depletion region larger. Often a voltage is applied that is large enough to extend the depletion region and its electric field over the entire volume of the detector, creating a fully depleted detector. Apart from increasing the active volume of the detector, a larger depletion zone has also the advantage of lowering the capacitance of the detector and therefore reducing the signal noise [58].

Incoming radiation or particles will create a number of electron-hole pairs proportional to the radiation energy in the depletion region. The average effective energy reqired to create a single electron-hole pair is 3.64 eV. Because of the electric field in the region, electrons and holes move to opposite sides and cause electrical signals. Assuming complete charge collection, these signals are direct measurements of the energy deposited by an ionizing particle in the active volume.

There are several methods to obtain position information from semiconductor detectors. One is the so-called resistive charge method. Here one side of the detector is equipped with high resistive anode, while the other side is equipped with a low-resistivity cathode. If a charged particle hits such a detector, the charge measured by the cathode will only depend on the energy of the particle, while the charge measured by the anode will depend on the energy of the particle as well as the resistance and therefore the distance between the anode and the point of impact. One can therefore obtain the position of the particle by dividing the signal from the anode by the one from the cathode. Using several anodes, one can also obtain two-dimensional position information. An example of a detector using this technique is the PSP, described in section 3.2.1.

Another approach is to segment the electrodes into strips of a few μm width with the strips of one electrode at an angle to the strips of the other. Since the electron-hole pairs that are created when a particle hits the detector travel along the electric field lines to the closest segments, only these segments will generate a significant pulse. It is therefore possible to obtain 2D information on the position of the particle from the readout of a double-sided silicon strip detector [58].

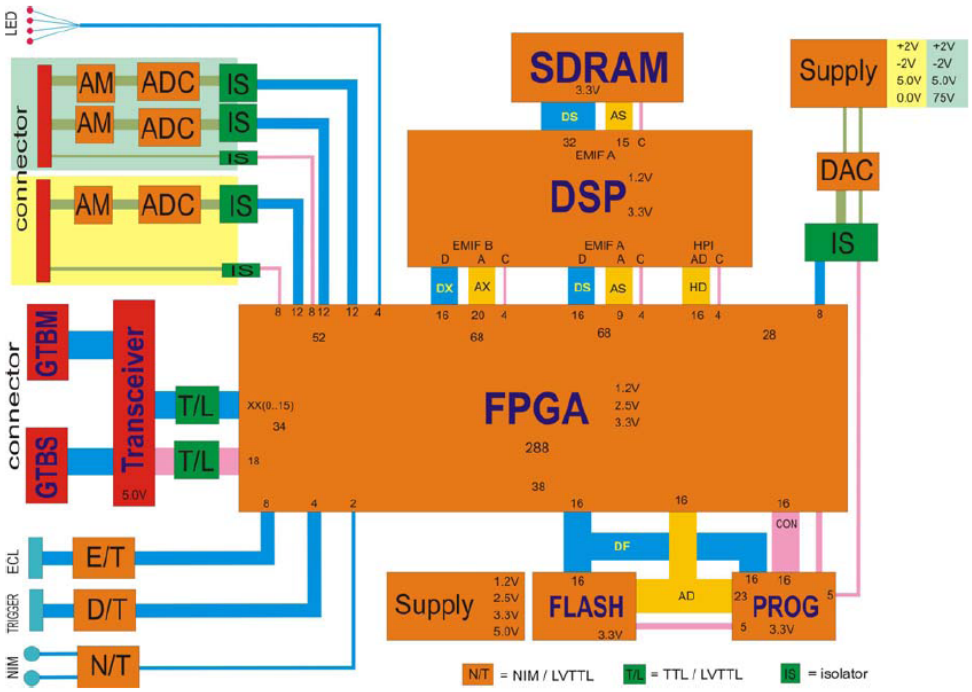

Figure 7.1: Schematic of the SIDEREM module used to read out the DSSDs in the R^{3}B-LAND setup. Its main components are three 12-bit Flash ADCs, two for the S/p-side and one for the K/n-side of the detector, an FPGA controlling the module and making the connection to the GTB, and a DSP processing the data coming from the ADCs before forwarding it to the DAQ. The numbers in the picture denote the number of signals sent between the modules.

As for all detectors, the signals coming from DSSDs have to be digitized using ADCs, and several steps of signal processing can be necessary (amplification, pulse shaping, etc.). However, the often very high density of channels of this kind of detector makes the use of conventional readout electronics difficult. Therefore, over the last decade, this has been increasingly done using ASICs [*], and programmable hardware, e.g. FPGAs[†] are used for the control of this readout.

In the next section examples of currently used and planned DSSDs at GSI and FAIR and their used or proposed solutions for the data readout will be presented. In Sections 7.2 and 7.3 the development of new front-end electronics aimed at a flexible use for varying detector prototypes will be described, and their initial tests will be described.

7.1 Double-Sided Silicon Strip Detectors at GSI and FAIR

An example of DSSDs currently used at GSI are the detectors used for tracking fragments and protons at the R^{3}B-LAND setup, which have been presented in section 3.2.2. Due to their large number of channels (640 readout strips on the S/p-side, 384 on the K/n-side), each of these detectors is read out using sixteen 64-channel VA ASICs produced by Gamma-Medica [35] and their output is sent to the SIDEREM [‡], a module specially developed by GSI for this purpose. A schematic of the SIDEREM

[*] Application-Specific Integrated Circuit
[†] Field Programmable Gate Array
[‡] SIlicon DEtector REadout Module

is shown in Fig. 7.1. Its main components are three 12-bit Flash ADCs, two for the S-side and one for the K-side, an FPGA, and a DSP [*]. The ADCs run in parallel, sampling the signals coming from the ASICs at a rate of 5 MHz. The Virtex4-FPGA controls the functionality of the module and makes the connection to the GTB[†], while the DSP filters the data coming from the ADCs before forwarding it to the DAQ.

This system has been succesfully used in several experiments since 2006. A big advantage of this system is the possibility to set the detector bias and charge collection time via VME. On the other hand, the electronics is incapable of producing a timing or trigger signal. This prevents the calibration of the DSSDs without the involvement of other detectors, e.g. in source runs. Furthermore, without a trigger signal, it is impossible to reduce the large number of readout channels using a sparse readout, making the readout quite slow because the readout time amounts to $T = 384/5\ \text{MHz} \approx 80\ \mu\text{s}$.

Over the next few years, FAIR[‡] will be built as an extension of the present GSI. Figure 7.2 shows an overview of the planned facilities together with the existing ones at GSI. In two of the proposed nuclear structure experiments, R^3B[§] [60] and EXL[¶] [61], DSSDs are planned to play a major role. While R^3B will be located at the high energy branch behind the fragment separator Super-FRS and use the highest beam energies it can provide, EXL is supposed to be located in the planned NESR[||].

[*] Digital Signal Processor
[†] General purpose Token driven Bus
[‡] Facility for Antiproton and Ion Research
[§] Reactions with Relativistic Radioactive Beams
[¶] EXotic nuclei studied in Light-ion induced reactions at the NESR storage ring
[||] New Experimental Storage Ring

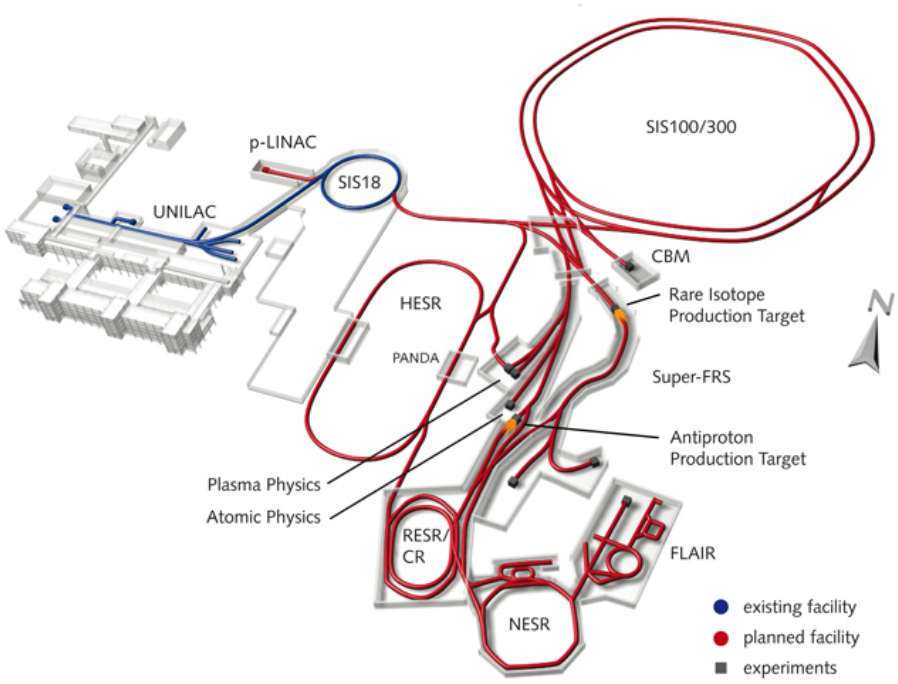

Figure 7.2: Overview of the planned facilities at FAIR, together with the present ones at GSI [59].

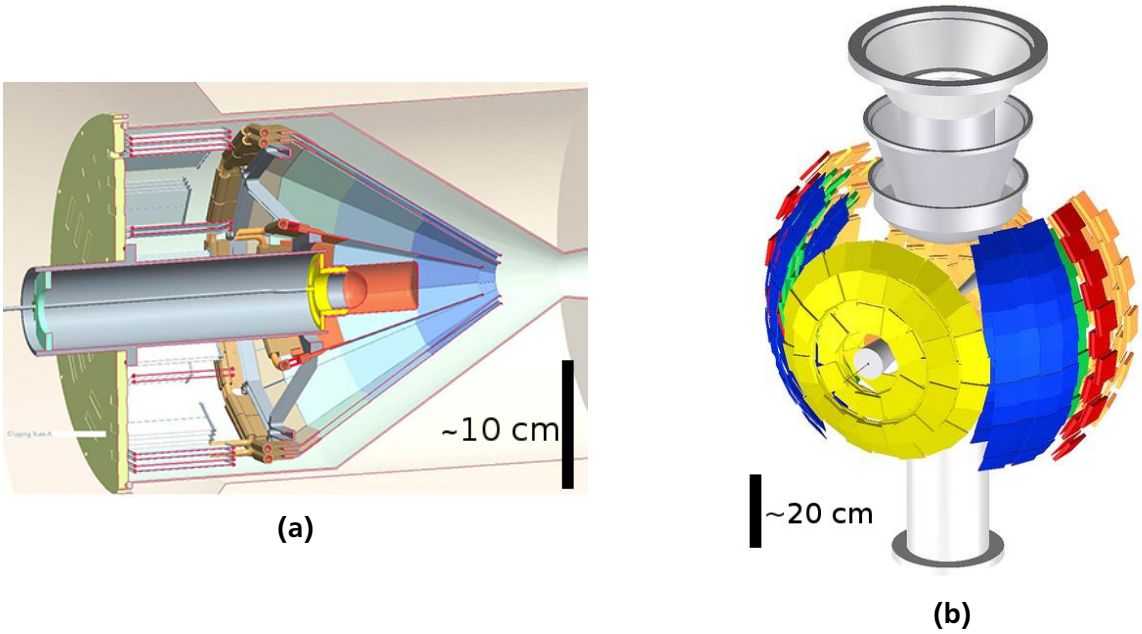

(a) (b)

Figure 7.3: Models of (a) the R^3B silicon tracker and (b) the EXL silicon array.

The Si-Tracker of the R^3B experiment and the ESPA* are desgined for similar purposes. Both are planned to be used for the detection of light charged particles emitted from the reaction target, e.g. the scattered nucleons in a QFS reaction. Both detectors are therefore supposed to surround the target in several layers and to be surrounded themselves by scintillator detectors for the detection of γ-rays and charged particles of energies up to 300 MeV [62]. Their geometry and size, however, differ substantially. While the R^3B tracker consists of 30 detector modules of 100-300 μm thickness which are arranged in three layers in a lampshade design, ESPA is planned to consist of 420 modules, also of 100-300 μm thickness, but arranged in two nearly spherical layers.

In the case of EXL, the development of detector prototypes is done in connection with experiments at the present ESR†. Here, one of the main focuses lies on (α, α')-experiments which require the ability to detect α-particles with energies down to 300 keV. A number of detector prototypes have been built or are under construction for this purpose, varying between 48 and 256 readout channels.

7.2 ASIC-based Readout Electronics

For most detectors described in the previous section, specialized readout electronics either already exists or is in development. However, the detector development in connection with FAIR leads to a large number of smaller-scale detector prototypes and therefore to a demand for more generic readout electronics which can easily be adapted to the different needs for different experiments. Developing such a generic solution and making the first steps towards commisioning it was the purpose of the work described here.

* EXL Silcion Particle Array
† Experimental Storage Ring

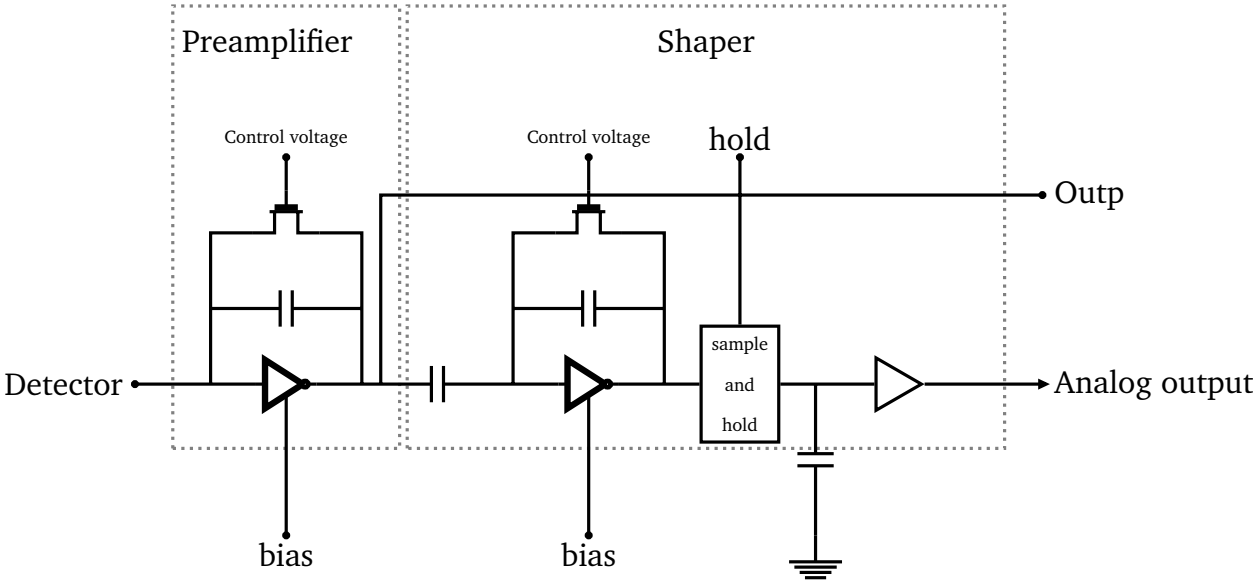

Figure 7.4: Schematic of the front-end of one channel of a VA chip, handling the analog signals coming from the detector. It consists of a preamplifier, a shaper, and a sample-and-hold logic unit. The analog output of all channels is multiplexed, i.e. all channels share the same line, but only one channel appears on the output at one time.

For this purpose the electronics was designed with the aim to keep them as flexible as possible. The design follows a simple scheme and is based on three main modules. The first one is the front-end board, which is directly connected to the detector and which houses two kinds of ASICs, one for the detector readout and one to generate trigger signals. The other modules are an ADC sampling the analog signals coming from the front-end board and a sequencing module, controlling the entire readout. While in case of the ASICs and the ADC commercially available modules were chosen, for the control module an FPGA-based solution was chosen to make adaptations as easy as possible. The initial design and development of this electronics has been described elsewhere [63]. However, the main points will be repeated here, and changes to the initial design which were made during later development stages and testing will be hihlighted.

As readout chips, ASICs of the VA-family by Gamma-Medica were chosen [64]. This chip family offers a wide dynamic range, making the suitable for a variety of different physics cases. Also, their power consumption is low enough to run the electronics in ultra-high vacuum, which is particularly important for the EXL experiment. Most VA chips have either 32 or 64 readout channels which are multiplexed so that always only one channel will appear on the analog output. In this case a 32-channel version was used. Each VA chip consists of a front-end and a back-end. The front-end handles the analog signals coming from the detector. A schematic of the front-end for a single channel is shown in Fig. 7.4. It consists of a preamplifier, a shaper, and a sample-and-hold logic unit. Many of the parameters for these elements are adjustable, including the gain of the preamplifier and the peaking time of the shaper (usually in the range of 1 to 3 μs). After the peaking time has elapsed, an external hold signal has to be applied, causing the chip to keep the charge of the output constant.

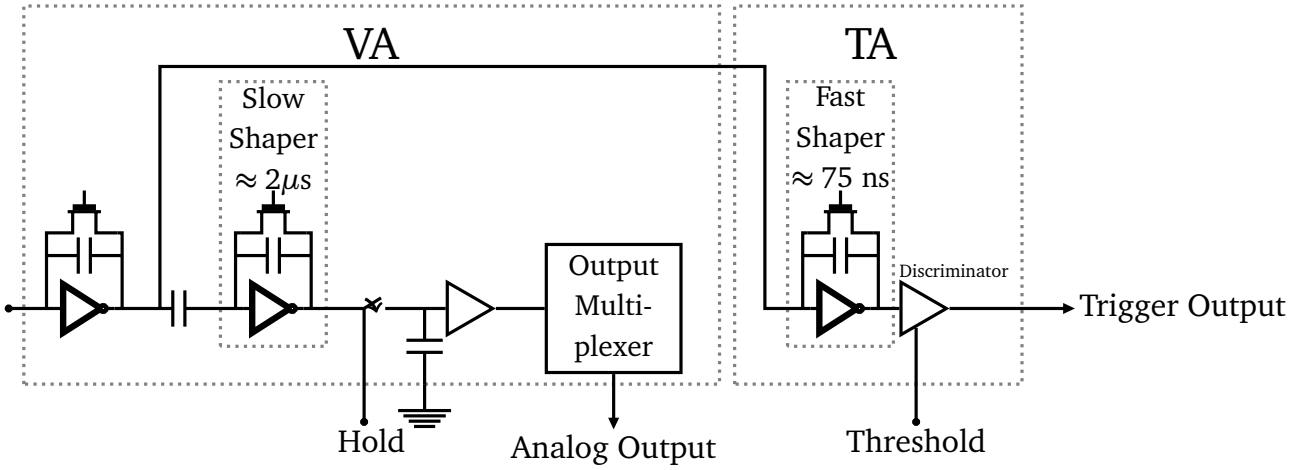

Figure 7.5: Illustration of the trigger generation using a TA ASIC. The signal is divided behind the preamplifier, and one part is sent to the TA, consisting of a fast shaper and a discriminator with adjustable threshold. If the signal coming from the shaper exceeds the threshold of the discriminator a trigger signal is generated.

The back-end is responsible for managing the digital control signals of the readout. The logic levels for each digital signal are +2 V ('1') and −2 V ('0'). Apart from the hold signal, the ASICs are controlled using only two signals. The shift-in signal starts the readout of the multiplexed signals and with each clock signal, the next readout channel appears on the output. Furthermore, an external reset can be applied. The ASICs also have a test mode. When the ASICs are in test mode, a second multiplexer is activated, connecting the channel which appears on the output to a calibration charge which again can be set externally.

The VA chips have been combined with the TA triggering ASICs making it possible to create self-triggering electronics [65]. Figure 7.5 illustrates the principle of operation [66]. The preamplifier is used by both chips. Behind it, the signal gets divided, and one part is sent to the TA. The TA consists of a fast shaper (shaping time ≈ 75 ns) and a discriminator with adjustable threshold. If the signal coming from the shaper exceeds the threshold of the discriminator, which can also be set extrenally, a trigger is generated. This trigger can then be sent e.g. to the data acquisition or a sequencing module which in turn will sent back the hold signal to the VA chips. Similarly to the VA chips, most threshold and bias voltages of the TA chips can be set externally. In addition several settings can be chosen using a 164-bit control register. Values are written to this register by appearing on the register input at the leading edge of a clock signal.

Two PCBs were designed by Peter Schakel at KVI* in Groningen, a front-end board and a converter board. The front-end board is designed to hold eight ASIC pairs which are bonded to it. While each pair has its own shift-in input and trigger output, they share the same hold and clock signal. Also, all TAs have their own calibration register input, but share the same clock for writing to this register. Apart from the ASICs, the board also houses two 8-channel SPI DACs†, providing the biases and thresholds for the ASICs. All ASICs receive the same voltages. The second board houses level converters convert-

* Kernfysisch Versneller Instituut
† Digital-to-Analog Converter

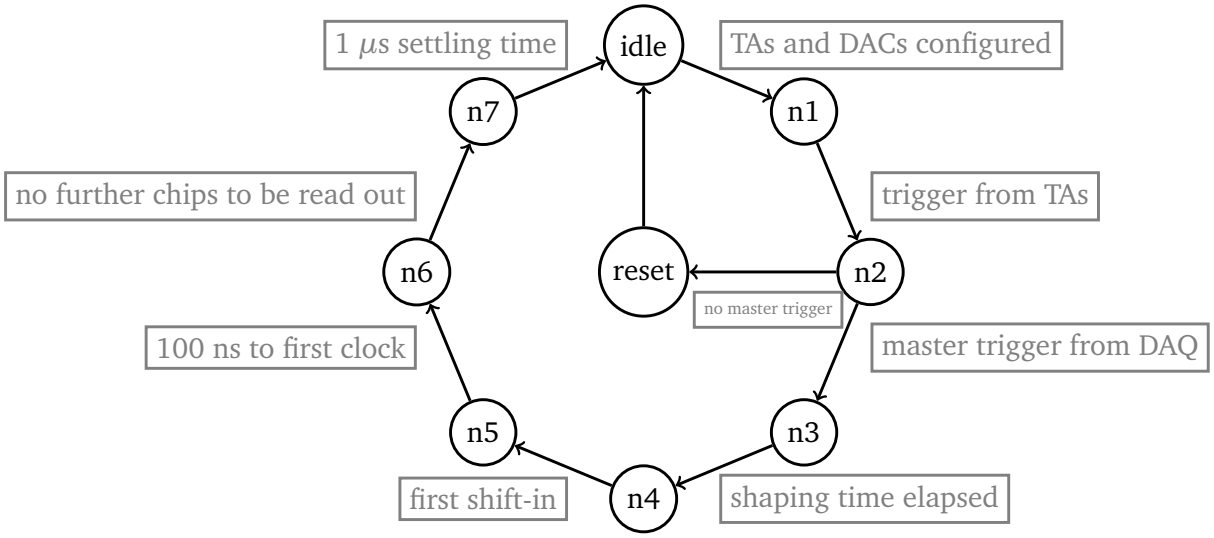

Figure 7.6: The finite state machine implemented in the sequencing module for the readout control. Each of the black circles denotes one state of the FSM, while each gray box denotes the condition to transition from one state to the other.

ing the LVDS signals coming from the VUPROM* to the logical levels required by the ASICs and vice versa.

During the initial development the CAEN module V550 was considered as ADC. However, several problems with the integration of this module into the MBS data acquisition system and the fact that the module is not in production anymore lead to a switch to the SIS3300 module developed by Struck, which proved to be more suitable. In principle, however, the electronics can work with any ADC, which is capable to handle multiplexed signals with a rate of several MHz, and can accept an external clock.

While also sequencing modules designed for the control of VA chips are commercially available (e.g. the CAEN V551), it was decided to develop a custom solution instead. Apart from the demanded flexibility and convenience mentioned before, the main reason was the aim to use the triggering capabilities of the VA-TA combination to create a sparse readout.

Based on these requirements, a VUPROM, a VME module developed at GSI, housing a Xilinx Virtex-4 FPGA, was used. Using a hardware description language, e.g. VHDL, this FPGA can be configured to fulfil various tasks. The corresponding configuration files are stored in a Flash memory also inside the VUPROM and are loaded into the FPGA upon a VME command by a CPLD† on startup. The VUPROM closely resembles the VULOM‡ described in section 3.2.4, differing mainly by the numbers of inputs and outputs available. While the VULOM provides 48 differential ECL level and 4 single level NIM in- or outputs, the VUPROM has 256 differential LVDS level in- or outputs of and two of NIM level. The VUPROM was chosen over the VULOM because of the large number of control signals for the readout. However, some of the initial hardware tests were also done using a VULOM.

* VME Universal PROcessing Module
† Complex Programmable Logic Device
‡ Vme Universal Logic module

The control module has several tasks. First, it handles the triggers, coming from the ASICs and forwards them to the DAQ. It also generates the control signals, i.e. the hold and shift-in signal for the ASICs, the clock signals for both the ASICs and the ADC and, if necessary a gate for the ADC. The test mode of the ASICs can be activated and steered by the module. Finally, the module is also responsible for the slow control of the ASICs. It can be used to set the voltages on the ASICs using DACs programmable via the SPI data bus as well as writing data to the TA control register.

The main tasks of the VUPROM, the handling of the triggers coming from the TAs and the control of the readout sequence, is implemented in the VHDL code in form of a FSM*, which is shown in Fig. 7.6. The sequencer has two modes, the default mode, in which all ASICs are read out and a zero-suppressed mode, in which only the ASICs that sent a trigger are read out. Also, there is the possibility to deactivate individual ASICs via VME, so that their triggers are ignored.

If the initialization is complete, i.e. the TAs and the DACs have been configured, the FSM will leave the `idle` state and enter state `n1`. In this state, the module is able to receive triggers coming from the TAs.

The module will forward the first trigger it receives to the DAQ and wait for validation (`n2`). If it receives the validation, i.e., the master trigger from the DAQ, it will initialize the readout by asserting the hold signal once the shaping time, which is adjustable via VME, has elapsed (`n3`). Otherwise, the module will enter the `reset` state, aborting the charge collection in the ASICs, and return to the `idle` state. The `reset` state can also be accessed at any time of the readout by accessing a dedicated VME register.

In state `n4` the shift-in signal is sent to the first VA to be read out. Whether a chip is to be read out is controlled using a Boolean variable s_0, whose value is calculated using

$$s_0 = (t \wedge a) \vee f. \tag{7.1}$$

The first chip in the chain with $s_0 = 1$ will receive the shift-in signal. The symbol t denotes whether an ASIC sent a trigger or not, a whether it is activated. Using f it is possible to force the readout of an ASIC, regardless of triggers. In general, $f = 1$ is set in the default mode and $f = 0$ in zero-suppressed mode. 100 ns after the shift-in signal was pulled high, the first clock signal is made active as well, the overlap of the two signals activating the multiplexer of the ASIC (`n5`). The clock signal is also, after an adjustable delay, sent to the ADC. After 32 channels, the next shift-in signal is sent, provided there is an ASIC with

$$s = s_0 \neg r = 1, \tag{7.2}$$

where the variable r denotes whether the chip was already read out (`n6`). If there is no further ASIC to be read out, the module enters state `n7`, releases the hold signal and waits for 1 μs for the VAs to settle

* Finite State Machine

before returning to the `idle` mode. If no changes to the configuration were done, it will return to state `n1`, ready to accept the next trigger.

Parts of the control of the test mode, e.g. the generation of clock and hold signal, works similarly, however this mode does not depend on any triggers. Instead, the ASIC and the channel that one wants to inspect at the output is selected using a VME register. This mode can be used with or without activating the calibration input of the VA ASICs.

7.3 Tests

Initial tests of the control module functionality were done via simulations using the program ISim which is part of the Xilinx Webpack software package. To do so, both a testbench program and a model of the front-end board were written in VHDL, reacting to the signals sent by the control logics. Details and results of these simulations can be found in Ref. [63].

In a second step, two VULOMs were configured, one using a version of the control module modified to use less outputs and one using the front-end board model, adapted so that it could be implemented in hardware. These two module were then put in a VME crate with a RIO3 processor running the MBS data acquisition system, a TRIVA trigger module and an ADC, initially of the type CAEN V550, later on replaced by a Struck SIS3300. In addition the setup consisted of a pulse generator, whose output was connected to the ADC analog input, and an oscilloscope for monitoring.

The VULOM model generated trigger signals at a fixed rate, which were sent to both the sequencing module and the trigger input of the pulser. The aim was to test the VME access to the different registers

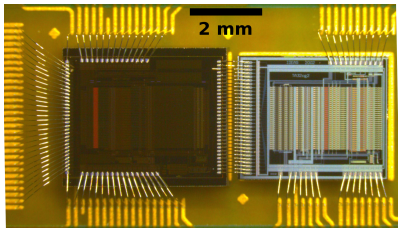

(a)

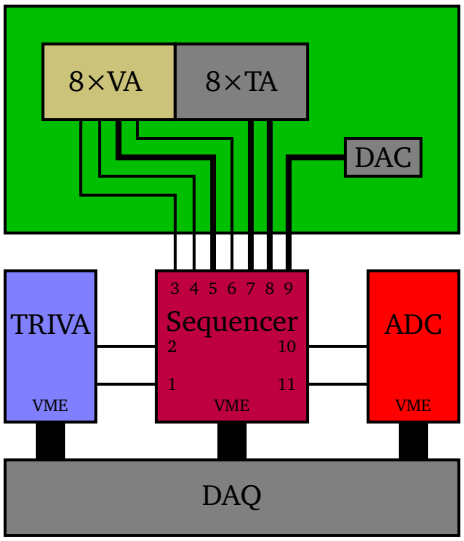

1 Trigger to TRIVA
2 Master Trigger from TRIVA
3 Hold to VA
4 Shift-in to VA (8×)
5 Clock to VA
6 Reset to VA
7 Trigger from TA (8×)
8 TA Control Register (2×)
9 SPI Signals (3×)
10 Clock to ADC
11 Gate to ADC

(b)

Figure 7.7: (a) Closeup of an ASIC pair bonded to the frontend board. (b) Wiring diagram of the test setup. Level converters have been omitted for clarity.

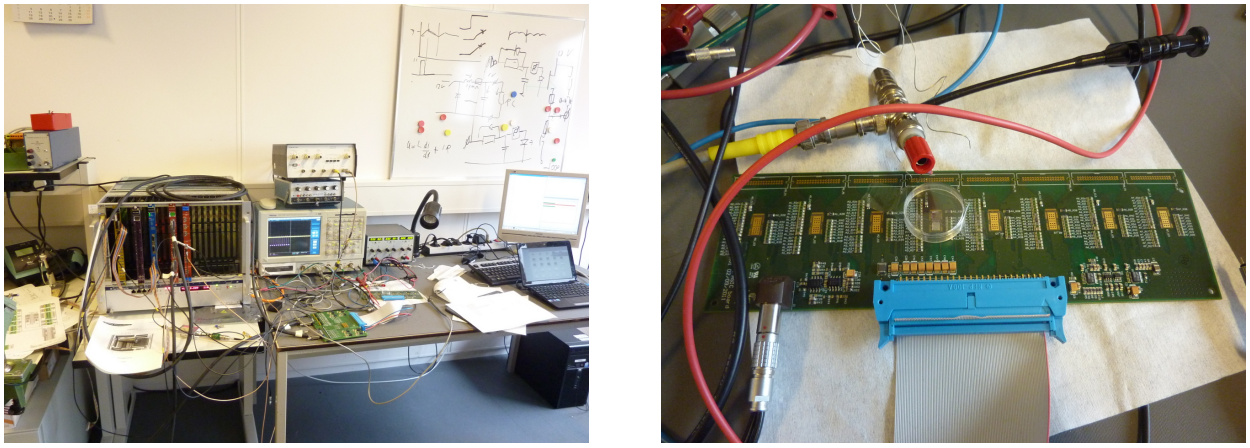

(a) (b)

Figure 7.8: (a) The Test setup at KVI. (b) Closeup of the front-end board with one pair of ASICs bonded on it and the pulser signal connected to one of its inputs using a capacitor.

of the control module, its communication with the ADCs, and to check whether timing issues occur, e.g., due to cable delays which were not taken into account in the simulations.

The first test using the real front-end board was done in February 2013 at KVI in Groningen. The purpose of this test was to check whether the control module can communicate with the ASICs and the DACs as assumed. A single ASIC pair was bonded on the board. A picture taken with the microscope is shown in Fig. 7.7(). The VA type VA32HDR14.2 suited for positive charges, and the TA type TACG32 were used. Some of their characteristics are listed in Table 7.1. Apart from the from the front-end and converter board, a similar setup as described above was used. Its wiring diagram is shown in Fig. 7.7(a) and a picture is shown in Fig. 7.8(a). A VUPROM was used instead of the VULOM, and the CAEN ADC was used. The output of the pulser was connected to the VA input with a capacitor, as is shown in Fig. 7.8(b). For most of the test, the readout clock was set to 500 kHz.

The slow control could be shown to work, both the TA control register and the configuration registers of the DACs could be configured. Figure 7.9(a) shows the trigger signal and the clock signal sent to the ADC. The time difference between the trigger and the first clock is $\approx 3.5\mu s$ which corrsponds to the sum of the selected shaping time (3 μs) and the set delay of the ADC clock (0.5 μs).

Table 7.1: Comparison of VA and TA ASIC characteristics

	VA32HDR14.2	VA32HDR14.3	TA32CG2
Shaping time	adjustable, $\approx 2\mu s$	adjustable, $\approx 2\mu s$	75 ns
Charge type	positive	negative	both
Gain preamplifier	5 mV/pC	115 mV/pC	-
Gain current output	0.16 μA/pC	77 μA/pC	-
Dynamic range	$\approx$ 13 pC	$\approx$ 20 pC	-

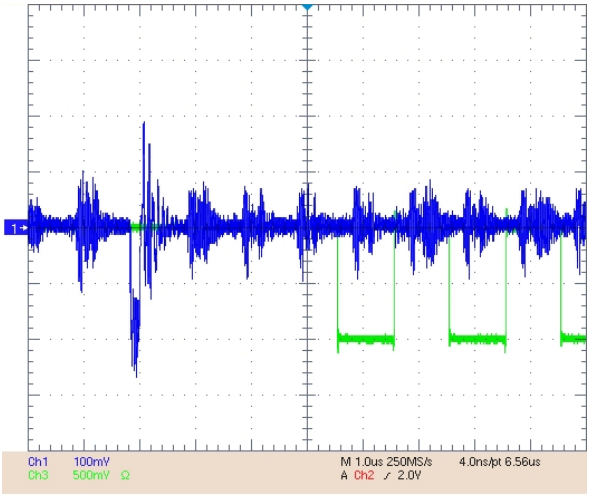

(a)

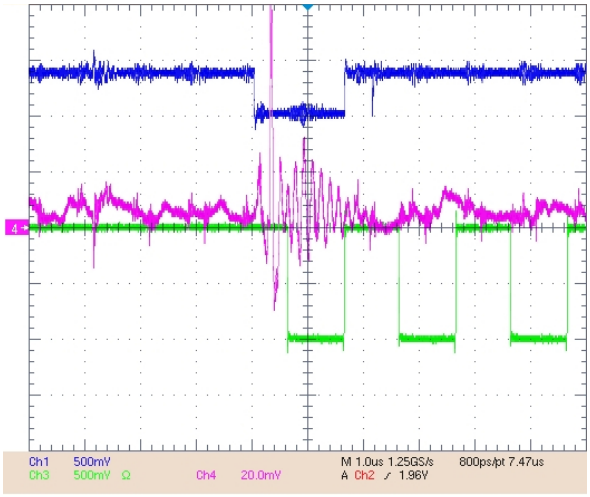

(b)

Figure 7.9: (a) Trigger signal (blue) and first clock (green). (b) Additional noise on output for the first channel. Shown is the shift-in signal (blue), the clock (green) and the VA output (pink).

The output of the first channel of the ASIC was found to be subject to additional noise, shown in Fig. 7.9(b). Because of that the clock signal of the first channel was extended, giving the output additional time to settle in. Also it was found that the ASICs need a 33rd clock signal to correctly finish their read-out cycle. Problems with the CAEN ADC were observed throughout the test and led to its replacement by the Struck module as mentioned before.

Figure 7.10 shows the VA output for optimized bias and threshold values in both test and multiplexed mode. Again, the used shaping time was 3 μs. The pulser was connected to two of the VA inputs.

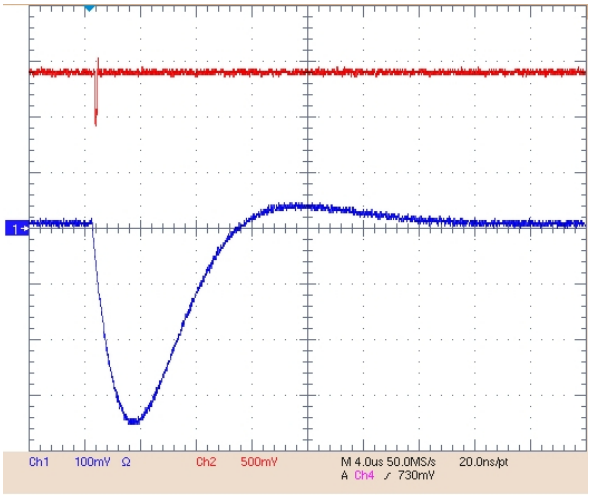

(a)

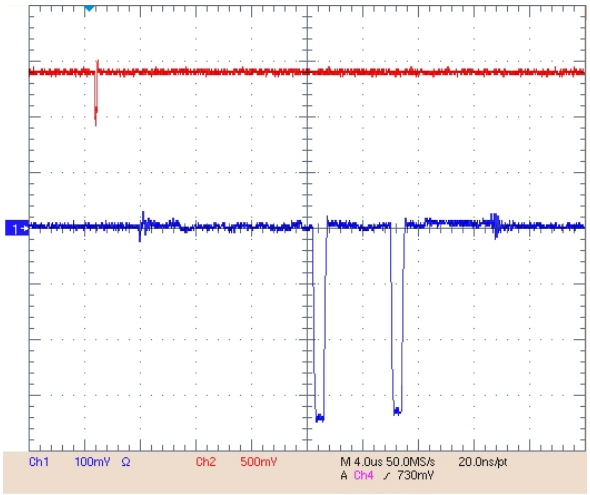

(b)

Figure 7.10: VA output (blue), and trigger (red). (a) VA output in (single-channel) test mode. The shaping time was set to 3 μs (b) VA output in normal (multiplexed) mode. The pulser signal was connected to two input pads via a capacitor.

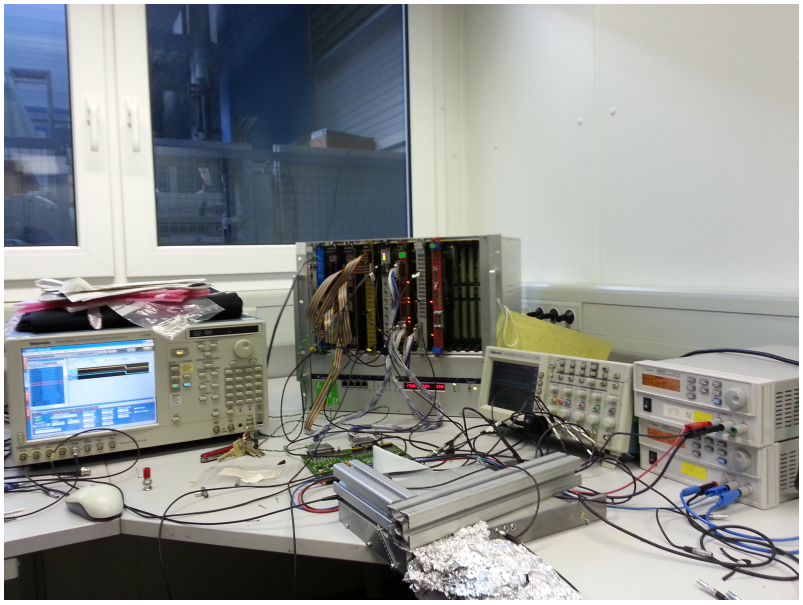

Figure 7.11: The test setup at GSI.

The completely assembled front-end board was tested for the first time in November 2013 at GSI. Two different types of VA chips were bonded, 5× VA32HDR14.2 one of which had been used during the test at KVI, and 3× VA32HDR14.3. Apart from checking the general functionality of the ASICs in combination with the VUPROM and the SIS 3301 ADC, the aim of these tests was to see if the chosen VA chips are suitable for use in upcoming (α, α') experiments planned by the EXL collaboration at the ESR which will require the detection of 300 keV α-particles.

Again, a similar setup as in the previous tests, shown in Fig. 7.11 was used. In the first part of the test, the pulser was again connected to the input of the ASICs to test the general functionality of ASICs, VUPROM, and ADC.

Since no shielding was used during the tests, the TAs were all very sensitive to noise, so that longer sequences of wrong triggers were sent out frequently. Because of this, for most of the test only two of the eight ASICs were activated. This minimized the problem but did not completely avoid it. Another issue was that, unlike for the VAs, only the common or-signal of all channels is accessible and it is not possible to have a look at the output signal of a single TA channel, making setting the right thresholds difficult. Therefore it was not possible to get triggers for signals below 200 mV during the test.

The VA chips funcioned well during the test and responded to the input as previously observed. However, it became clear that the two types of VAs need different biases and especially that their TAs need to have thresholds of opposite polarities, which makes their connection to the same DACs problematic.

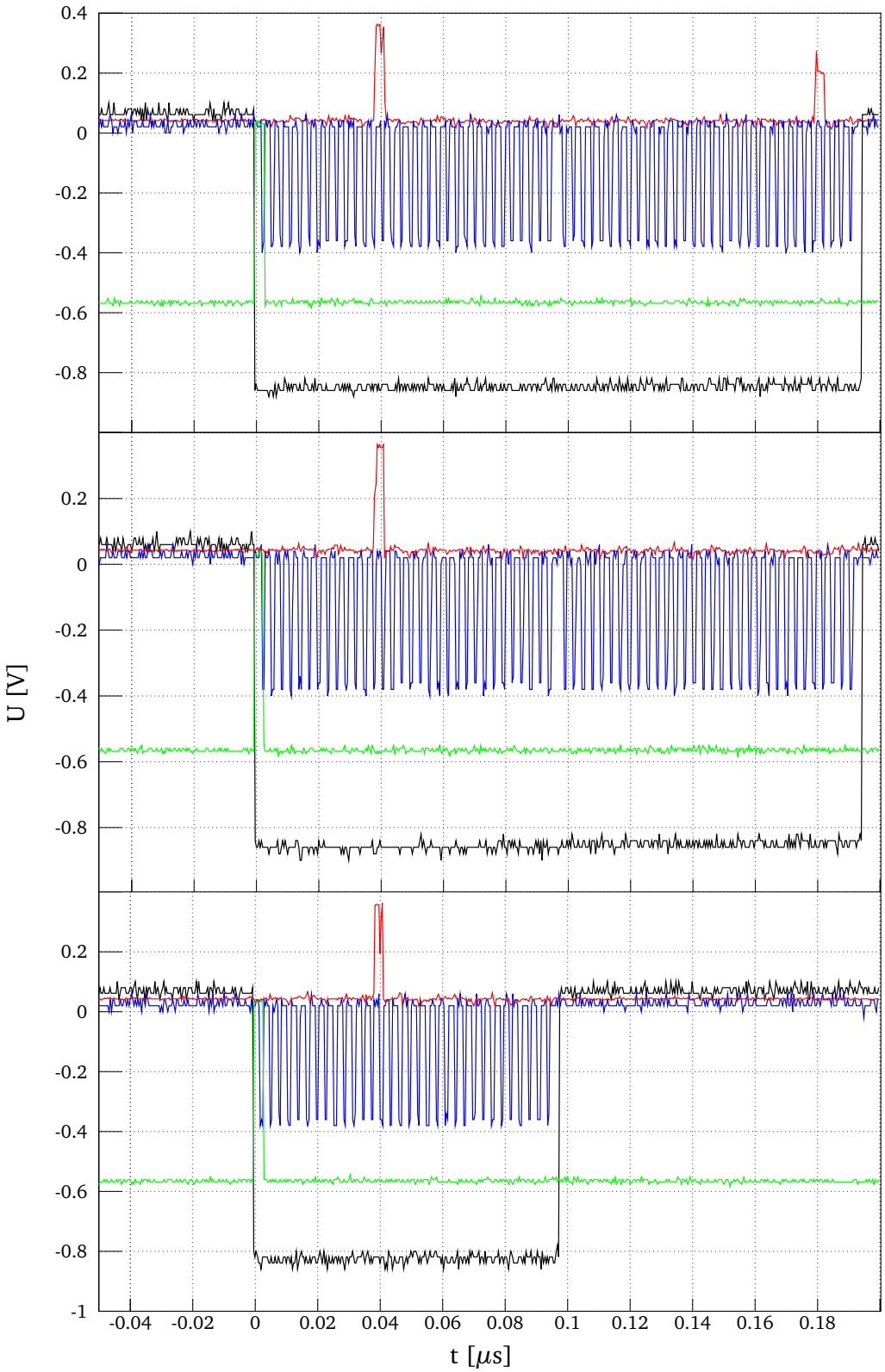

Figure 7.12: Comparison of default and zero-suppressed mode, shown for two activated ASIC pairs. Shown are VA output (red), clock (blue), the first shift-in signal (green), and the hold signal (black). Upper panel: The pulser is connected to both ASICs. All 64 channels are read out. Middle panel: Only one ASIC receives the input and the default readout mode is activated. All 64 channels are read out. Lower panel: Only one ASIC receives the input and the zero suppression is active. Only the ASIC with a signal is read out.

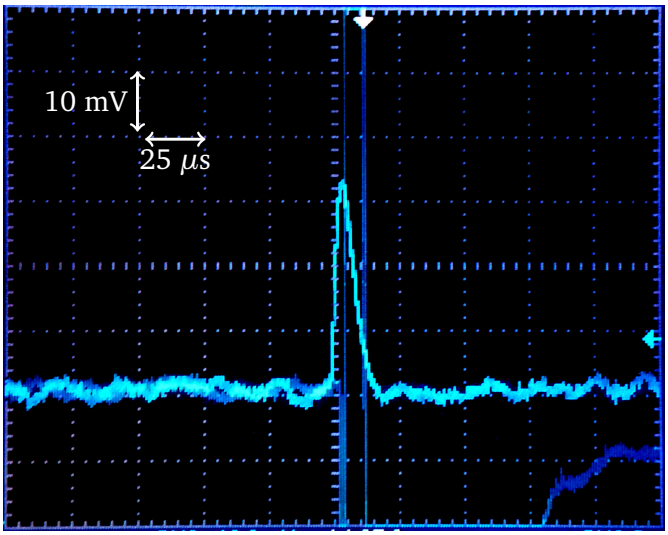

Figure 7.13: Sampler output of a VA chip for a 5.5 MeV α emitted by a ^{241}Am source.

Since it could not be tested with just one ASIC pair, to see whether the default and the zero-suppressed readout mode work as expected was of special interest. Figure 7.12 shows that this is the case. Shown are the VA output, the clock, and the hold signal The signals were obtained with only two of the eight pairs activated. The upper panel shows the case of the pulser being connected to both ASICs. The different pulse height is due to different capacitors used to connect the input. All 64 channels are read out. The middle and lower panels show the case, that only one ASIC receives the input. In the middle panel, the default readout mode is activated, so all 64 channels get read out anyway. In the lower panel the zero suppression is active, so only the ASIC with a signal gets read out.

In the second part of the tests, the inputs of one of the ASIC pairs were connected to a pin diode, and an ^{241}Am source was placed in front of this detector in a small vacuum chamber. Auxiliary modules for this detector, i.e. a voltage supply were place in an additional NIM crate. Figure 7.13 shows the VA output for a 5.5 MeV α measured by the pin diode. This signal was measured with one of the VA32HDR14.2 ASICs in the single channel test mode described above. An amplified signal was applied to a different channel to get a trigger signal despite the TA problems mentioned before. While the signal is clearly visible, the amplitude is only $\approx$ 30 mV, which makes it clear that with this kind of VA chip it will not possible to observe 300 keV α-particles.

More sensitive types of VA chips are available from Gamma-Medica. Together with effective shielding against electronic noise, these could be used to build suitable frontend electronics for the upcoming EXL experiments.

8 Conclusion and Outlook

The main part of the work presented here was aimed at a quantitative understanding of spectroscopic factors of the neutron-deficient carbon isotopes ^{10}C and ^{11}C. To investigate this, quasi-free scattering in inverse kinematics of these isotopes was used. Combining measurements with a CH_2 and a carbon target, the cross sections corresponding to quasi-free scattering on hydrogen was reconstructed. Table 8.1 summarises the cross sections for both targets and for the reconstructed hydrogen target for the three reactions ^{11}C(p,2p)^{10}B, ^{11}C(p,pn)^{10}C, and ^{10}C(p,pn)^{9}C.

Theoretical cross sections from DWIA calculations as well as spectroscopic factors and their quenching factors, obtained by comparing the experimental and theoretical cross sections, are also given in Tab. 8.1. The values strongly contradict the trend previously observed in knockout reactions using beryllium and carbon targets which show a stronger quenching for the removal of the more deeply bound nucleon in nuclei with a large difference in binding energy. The quenching obtained in (p,pn) is also less severe than the one observed in electron scattering of stable nuclei.

These values are not yet final. Improving them would, e.g., require studying and in detail absorption effects of QFS nucleons in the nucleus and including them into the event generator which is used for deriving the detector response of the Crystal Ball. Comparing the final results with the ones obtained in a recent experiment on ^{12}C, as well as with those for the neutron-rich isotopes, which are also under analysis at the moment, could enhance the understanding of the phenomenon of quenching significantly. The measured momentum distributions for the fragments of these three reactions show good agreement with DWIA-calculations for a p-shell knockout. The analysis of the γ-energy spectra measured in coincidence with ^{11}C(p,pn)^{10}C and ^{11}C(p,2p)^{10}B reveals a strong population of the low-lying excited states in both cases, indicating a strong contribution of particle-hole states to the ground state of ^{11}C. Also, the low-lying unbound states are populated with a large cross section in both ^{10}C and ^{11}C. No indication of knockout from the s-shell, expected to occur at excitation energies $E^* \gtrsim 20$ MeV has been observed in the present analyis. However, these invariant mass analysis employed suffers from acceptance cuts for both the fragments and the protons and assumptions about the proton velocity. A more detailed analysis using similar tracking for the protons as for the fragments as well as simulations of the detector response of both the fragment and the proton arm could lead to a better undestanding of these reactions.

Table 8.1: Summary of obtained cross sections, spectroscopic factors, and reduction factors for (p2,p) and (p,pn).

Reaction	σ_{CH2} [mb]	σ_C [mb]	σ_H [mb]	σ_{th} [mb]	σ_{sp} [mb]	C^2S	R_S
^{11}C(p,2p)^{10}B	56.3(15)	21.6(8)	17.3(8)	32.0	8.0	2.16(10)	0.53(2)
^{11}C(p,pn)^{10}C	77.2(32)	34.8(23)	21.2(20)	25.8	8.6	2.47(23)	0.82(8)
^{10}C(p,pn)^{9}C	72.2(39)	32.8(39)	19.7(28)	18.9	9.5	2.09(30)	1.04(15)

The cross section for the reaction ^{11}C(p,pα)^{7}Be has been determined to be $\sigma_H = 5.8(4)$ mb, differing from the nucleon knockout only by a factor 3-4. Such a large cross section is unlikely to be caused by multiple knockouts of single nucleons, and decays of excited ^{10}B or ^{10}C resulting in ^{7}Be can be excluded due to the large excitation energy needed. Thus, it is indication of a preformed α-particle in the ^{11}C ground state.

Due to the small spatial separation of the decay products of the unbound ^{9}B on the silicon detectors and limited acceptance of the proton drift chambers, no reliable cross section could be determined for the reaction ^{10}C(p,2p)^{9}B. Similar to the analysis of unbound excited state, this analysis could benefit a lot from both proton tracking and detailed simulations of the detector responses, especially concerning the silicon strip detectors behind the target.

In the second part of this work the development of new front-end electronics for double-sided silicon strip detectors based on the VA and TA ASICs by Gamma-Medica and the Struck SIS3300 ADC has been presented. A custom sequencing module for handling trigger signals, controlling the readout and managing the slow control of the ASICs has been developed for this purpose, implementing the required functionality in the FPGA of the VUPROM module developed at GSI.

The correct functionality of the sequencing module could be shown in initial tests. However, due to the extreme sensitivity of the ASICs to noise, these could not yet be characterized. Proper shielding of the ASICs inpud pads, together with a better understanding of the trigger generation in the TA ASICs, will be key to commissioning the electronics and using it in experiments.

Bibliography

[1] M. Goeppert-Mayer. On closed shells in nuclei. *Physical Review*, 74:235, 1948.

[2] O. Haxel, J.H.D. Jensen, and H. Suess. On the Magic Numbers in Nuclear Structure. *Physical Review*, 75:1766, 1949.

[3] P.G. Hansen and J.A. Tostevin. Direct Reactions With Exotic Nuclei. *Annual Review of Nuclear and Particle Science*, 53(1):219–261, December 2003.

[4] G.J. Kramer, H.P. Blok, and L. Lapikás. A consistent analysis of (e,ep) and (d,3He) experiments. *Nuclear Physics A*, 679(3-4):267–286, January 2001.

[5] G. Jacob and T.A.J. Maris. Quasi-Free Scattering and Nuclear Structure. *Reviews of Modern Physics*, 38(1):121–142, 1966.

[6] A.N. Antonov, M.K. Gaidarov, M.V. Ivanov, D.N. Kadrev, M. Aïche, G. Barreau, S. Czajkowski, B. Jurado, G. Belier, A. Chatillon, T. Granier, J. Taieb, D. Doré, A. Letourneau, D. Ridikas, E. Dupont, E. Berthoumieux, S. Panebianco, F. Farget, C. Schmitt, L. Audouin, E. Khan, L. Tassan-Got, T. Aumann, P. Beller, K. Boretzky, A. Dolinskii, P. Egelhof, H. Emling, B. Franzke, H. Geissel, A. Kelic-Heil, O. Kester, N. Kurz, Y. Litvinov, G. Münzenberg, F. Nolden, K.-H. Schmidt, Ch. Scheidenberger, H. Simon, M. Steck, H. Weick, J. Enders, N. Pietralla, A. Richter, G. Schrieder, A. Zilges, M.O. Distler, H. Merkel, U. Müller, A.R. Junghans, H. Lenske, M. Fujiwara, T. Suda, S. Kato, T. Adachi, S. Hamieh, M.N. Harakeh, N. Kalantar-Nayestanaki, H. Wörtche, G.P.A. Berg, I.A. Koop, P.V. Logatchov, A.V. Otboev, V.V. Parkhomchuk, D.N. Shatilov, P.Y. Shatunov, Y.M. Shatunov, S.V. Shiyankov, D.I. Shvartz, A.N. Skrinsky, L.V. Chulkov, B.V. Danilin, A.A. Korsheninnikov, E.A. Kuzmin, A.A. Ogloblin, V.A. Volkov, Y. Grishkin, V.P. Lisin, A.N. Mushkarenkov, V. Nedorezov, A.L. Polonski, N.V. Rudnev, A.A. Turinge, A. Artukh, V. Avdeichikov, S.N. Ershov, A. Fomichev, M. Golovkov, A.V. Gorshkov, L. Grigorenko, S. Klygin, S. Krupko, I.N. Meshkov, A. Rodin, Y. Sereda, I. Seleznev, S. Sidorchuk, E. Syresin, S. Stepantsov, G. Ter-Akopian, Y. Teterev, A.N. Vorontsov, S.P. Kamerdzhiev, E.V. Litvinova, S. Karataglidis, R. Alvarez Rodriguez, M.J.G. Borge, C. Fernandez Ramirez, E. Garrido, P. Sarriguren, J.R. Vignote, L.M. Fraile Prieto, J. Lopez Herraiz, E. Moya de Guerra, J. Udias-Moinelo, J.E. Amaro Soriano, A.M. Lallena Rojo, J.A. Caballero, H.T. Johansson, B. Jonson, T. Nilsson, G. Nyman, M. Zhukov, P. Golubev, D. Rudolph, K. Hencken, J. Jourdan, B. Krusche, T. Rauscher, D. Kiselev, D. Trautmann, J. Al-Khalili, W. Catford, R. Johnson, P.D. Stevenson, C. Barton, D. Jenkins, R. Lemmon, M. Chartier, D. Cullen, C.A. Bertulani, and A. Heinz. The electronion scattering experiment elise at the international facility for antiproton and ion research (fair)a conceptual design study. *Nuclear Instruments and Methods in Physics Research Section A: Accelerators, Spectrometers, Detectors and Associated Equipment*, 637(1):60 – 76, 2011.

[7] A. Gade, P. Adrich, D. Bazin, M. D. Bowen, B. A. Brown, C. M. Campbell, J. M. Cook, T. Glasmacher, P. G. Hansen, K. Hosier, S. McDaniel, D. McGlinchery, A. Obertelli, K. Siwek, L. A. Riley, J. A.

Tostevin, and D. Weisshaar. Reduction of spectroscopic strength: Weakly-bound and strongly-bound single-particle states studied using one-nucleon knockout reactions. *Physical Review C*, 77(4):044306, April 2008.

[8] J. Lee, M.B. Tsang, D. Bazin, D. Coupland, V. Henzl, D. Henzlova, M. Kilburn, W. Lynch, A. Rogers, A. Sanetullaev, Z. Sun, M. Youngs, R. Charity, L. Sobotka, M. Famiano, S. Hudan, D. Shapira, P. OMalley, W. Peters, K. Chae, and K. Schmitt. Neutron spectroscopic factors of 34Ar and 46Ar from (p,d) transfer reactions. *Physical Review C*, 83(1):014606, January 2011.

[9] W.H. Dickhoff and C. Barbieri. Self-consistent Green's function method for nuclei and nuclear matter. *Progress in Particle and Nuclear Physics*, 52(2):377–496, 2004.

[10] G. Jacob and T.A.J. Maris. Quasi-Free Scattering and Nuclear Structure. II. *Reviews of Modern Physics*, 45(1):6–21, 1973.

[11] T. Aumann. Prospects of nuclear structure at the future GSI accelerators. *Progress in Particle and Nuclear Physics*, 59(1):3–21, July 2007.

[12] V. Panin. *Fully Exclusive Measurements of Quasi-Free Single-Nucleon Knockout Reactions in Inverse Kinematics*. Dissertation, Technische Universität Darmstadt, 2012.

[13] M. Yosoi, H. Akimune, I. Daito, H. Ejiri, H. Fujimura, M. Fujiwara, T. Ishikawa, M. Itoh, T. Kawabata, M. Nakamura, T. Noro, E. Obayashi, H. Sakaguchi, H. Takeda, T. Taki, A. Tamii, H. Toyokawa, N. Tsukahara, M. Uchida, T. Yamada, and H.P. Yoshida. Structure and decay of the s-hole state in 11B studied via the 12C(p,2p)11B* reaction. *Physics Letters B*, 551:255–261, 2003.

[14] G. F. Grinyer, D. Bazin, A. Gade, J. A. Tostevin, P. Adrich, M. D. Bowen, B. A. Brown, C. M. Campbell, J. M. Cook, T. Glasmacher, S. McDaniel, P. Navrátil, A. Obertelli, S. Quaglioni, K. Siwek, J. R. Terry, D. Weisshaar, and R. B. Wiringa. Knockout Reactions from p-Shell Nuclei: Tests of Ab Initio Structure Models. *Physical Review Letters*, 106(16):162502, April 2011.

[15] V. Volkov. private communication.

[16] J. Enders, T. Baumann, B. A. Brown, N. H. Frank, P. G. Hansen, P. R. Heckman, B. M. Sherrill, A. Stolz, M. Thoennessen, J. A. Tostevin, E. J. Tryggestad, S. Typel, and M. S. Wallace. Spectroscopic factors measured in inclusive proton-knockout reactions on 8B and 9C at intermediate energies. *Physical Review C*, 67:064301, June 2003.

[17] B. Brown, P. Hansen, B. Sherrill, and J. Tostevin. Absolute spectroscopic factors from nuclear knockout reactions. *Physical Review C*, 65(6):061601, May 2002.

[18] N. K. Timofeyuk. Spectroscopic factors and asymptotic normalization coefficients for 0p-shell nuclei: Recent updates. *Physical Review C*, 88(4):044315, October 2013.

[19] A. M. Mukhamedzhanov and A. S. Kadyrov. Unitary correlation in nuclear reaction theory: Separation of nuclear reactions and spectroscopic factors. *Physical Review C*, 82(5):051601, November 2010.

[20] N.S. Chant and P.G. Roos. Distorted-wave impulse-approximation calculations for quasifree cluster knockout reactions. *Physical Review C*, 15(1):57–68, 1977.

[21] N.S. Chant and P.G. Roos. Spin orbit effects in quasifree knockout reactions. *Physical Review C*, 27(3):1060–1072, 1983.

[22] T. Aumann, C. A. Bertulani, and J. Ryckebusch. Quasifree (p,2p) and (p,pn) reactions with unstable nuclei. *Physical Review C*, 88:064610, December 2013.

[23] W. von Oertzen, M. Freer, and Y. Kanada'Enyo. Nuclear clusters and nuclear molecules. *Physics Reports*, 432(2):43–113, September 2006.

[24] M. Freer. The clustered nucleuscluster structures in stable and unstable nuclei. *Reports on Progress in Physics*, 70(12):2149–2210, December 2007.

[25] Y. Kanada-En'yo and H. Horiuchi. Structure of light unstable nuclei studied with antisymmetrized molecular dynamics. *Progress of Theoretical Physics Supplement*, (142):205–262, 2001.

[26] H. Feldmeier, K. Bieler, and J. Schnack. Fermionic molecular dynamics for ground states and collisions of nuclei. *Nuclear Physics A*, 586(3):493–532, April 1995.

[27] M. Chernykh, H. Feldmeier, T. Neff, P. von Neumann-Cosel, and A. Richter. Structure of the Hoyle State in C12. *Physical Review Letters*, 98(3):032501, January 2007.

[28] Y. Kanada-En'yo, F. Kobayashi, and T. Suhara. Structures of ground and excited states in C isotopes. *Journal of Physics: Conference Series*, 445:012037, July 2013.

[29] T. Kobayashi, K. Ozeki, K. Watanabe, Y. Matsuda, Y. Seki, T. Shinohara, T. Miki, Y. Naoi, H. Otsu, S. Ishimoto, S. Suzuki, Y. Takahashi, and E. Takada. (p,2p) Reactions on 916C at 250 MeV/A. *Nuclear Physics A*, 805(1-4):431c—-438c, June 2008.

[30] https://www.gsi.de/forschung_beschleuniger/beschleunigeranlage.htm.

[31] K. Blasche. The heavy ion synchrotron SIS. In *EPAC 92: Third European Particle Accelerator Conference*, pages 9–13, 1992.

[32] H. Geissel, P Armbruster, KH Behr, and A Brunle. The GSI projectile fragment separator (FRS): a versatile magnetic system for relativistic heavy ions. *Nuclear Instruments and Methods in Physics Reseach B*, 1992.

[33] S. Altstadt. *13,14B(n,g) via Coulomb Dissociation to Constrain the Astrophysical r-Process*. Dissertation, Johann Wolfgang Goethe-Universität, Germany, 2014.

[34] B. Alpat, G. Ambrosi, Ph. Azzarello, R. Battiston, P. Bene, B. Bertucci, S. Bizzaglia, M. Bizzarri, S. Blasko, M. Bourquin, Ph. Bouvier, W.J. Burger, M. Capell, C. Cecchi, Y.H. Chang, E. Cortina, N. Dinu, G. Esposito, E. Fiandrini, D. Haas, H. Hakobyan, M. Ionica, R. Ionica, A. Kounine, V. Koutsenko, A. Lebedev, C. Lechanoine-Leluc, C.H. Lin, F. Masciocchi, M. Menichelli, S. Natale, M. Paniccia, A. Papi, M. Pauluzzi, E. Perrin, M. Pohl, D. Rapin, J.P. Richeux, W. Wallraff, M. Willenbrock, and

P. Zuccon. Charge determination of nuclei with the AMS-02 silicon tracker. *Nuclear Instruments and Methods in Physics Research Section A: Accelerators, Spectrometers, Detectors and Associated Equipment*, 540(1):121–130, March 2005.

[35] E. Nygaard, P. Aspell, P. Jarron, P. Weilhammer, and K. Yoshioka. CMOS low noise amplifier for microstrip readout Design and results. *Nuclear Instruments and Methods in Physics Research Section A: Accelerators, Spectrometers, Detectors and Associated Equipment*, 301(3):506–516, 1991.

[36] V. Metag, D. Habs, and K. Helmer. The Darmstadt-Heidelberg-Crystal-Ball. In *Lecture Notes in Physics*, volume 178, pages 163–178. 1983.

[37] J. Cub, G. Stengel, A. Grünschloß, K. Boretzky, T. Aumann, W. Dostal, B. Eberlein, Th.W. Elze, H. Emling, G. Ickert, J. Holeczek, R. Holzmann, J.V. Kratz, R. Kulessa, Y. Leifels, H. Simon, K. Stelzer, J. Stroth, A. Surowiec, and E. Wajda. A large-area scintillating fibre detector for relativistic heavy ions. *Nuclear Instruments and Methods in Physics Research Section A: Accelerators, Spectrometers, Detectors and Associated Equipment*, 402(1):67–74, January 1998.

[38] Th. Blaich, Th.W. Elze, H. Emling, H. Freiesleben, K. Grimm, W. Henning, R. Holzmann, G. Ickert, J.G. Keller, H. Klingler, W. Kneissl, R. König, R. Kulessa, J.V. Kratz, D. Lambrecht, J.S. Lange, Y. Leifels, E. Lubkiewicz, M. Proft, W. Prokopowicz, C. Schütter, R. Schmidt, H. Spies, K. Stelzer, J. Stroth, W. Walus, E. Wajda, H.J. Wollersheim, M. Zinser, and E. Zude. A large area detector for high-energy neutrons. *Nuclear Instruments and Methods in Physics Research Section A: Accelerators, Spectrometers, Detectors and Associated Equipment*, 314(1):136–154, April 1992.

[39] D.M. Rossi. *Investigation of the Dipole Response of Nickel Isotopes in the Presence of a High-Frequency Electromagnetic Field*. Dissertation, Johannes Gutenberg-Universität Mainz, Germany, 2009.

[40] C. Caesar. *Beyond the Neutron Drip-Line: Superheavy Oxygen Isotopes*. Dissertation, Technische Universität Darmstadt, Germany, 2012.

[41] F. Wamers. *Quasi-Free-Scattering and One-Proton-Removal Reactions with the Proton-Dripline Nucleus 17 Ne at Relativistic Beam Energies*. Dissertation, Technische Universität Darmstadt, Germany, 2011.

[42] H.G. Essel and N. Kurz. GSI Multi-Branch System Reference Manual, 2010.

[43] http://web-docs.gsi.de/˜rplag/land02/.

[44] R. Brun and F. Rademakers. ROOT An object oriented data analysis framework. *Nuclear Instruments and Methods in Physics Research Section A: Accelerators, Spectrometers, Detectors and Associated Equipment*, 389(1-2):81–86, April 1997.

[45] K. Mahata, H.T. Johansson, S. Paschalis, H. Simon, and T. Aumann. Position reconstruction in large-area scintillating fibre detectors. *Nuclear Instruments and Methods in Physics Research Section A: Accelerators, Spectrometers, Detectors and Associated Equipment*, 608(2):331–335, September 2009.

[46] J. Alcaraz, B. Alpat, G. Ambrosi, Ph. Azzarello, R. Battiston, B. Bertucci, J. Bolmont, M. Bourquin, W.J. Burger, M. Capell, F. Cardano, Y.H. Chang, V. Choutko, E. Cortina, N. Dinu, G. Esposito, E. Fiandrini, D. Haas, S. Haino, H. Hakobyan, M. Ionica, R. Ionica, A. Jacholkowska, A. Kounine, V. Koutsenko, G. Lamanna, A. Lebedev, C. Lechanoine-Leluc, C.H. Lin, M. Menichelli, S. Natale, A. Oliva, M. Paniccia, M. Pauluzzi, E. Perrin, M. Pohl, D. Rapin, M. Sapinski, I. Sevilla, W. Wallraff, P. Zuccon, and C. Zurbach. The alpha magnetic spectrometer silicon tracker: Performance results with protons and helium nuclei. *Nuclear Instruments and Methods in Physics Research Section A: Accelerators, Spectrometers, Detectors and Associated Equipment*, 593(3):376–398, August 2008.

[47] http://ralfplag.de/tracker/.

[48] A. J. Hartzler and R. T. Siegel. 400-mev neutron-proton scattering. *Physical Review*, 95:185–192, July 1954.

[49] A. J. Hartzler, R. T. Siegel, and W. Opitz. Small-angle neutron-proton scattering at 400 mev. *Physical Review*, 95:591–592, July 1954.

[50] D. Bertini. R3broot, simulation and analysis framework for the r3b experiment at fair. *Journal of Physics: Conference Series*, 331(3):032036, 2011.

[51] S. Agostinelli, J. Allison, K. Amako, J. Apostolakis, H. Araujo, P. Arce, M. Asai, D. Axen, S. Banerjee, G. Barrand, F. Behner, L. Bellagamba, J. Boudreau, L. Broglia, A. Brunengo, H. Burkhardt, S. Chauvie, J. Chuma, R. Chytracek, G. Cooperman, G. Cosmo, P. Degtyarenko, A. Dell'Acqua, G. Depaola, D. Dietrich, R. Enami, A. Feliciello, C. Ferguson, H. Fesefeldt, G. Folger, F. Foppiano, A. Forti, S. Garelli, S. Giani, R. Giannitrapani, D. Gibin, J.J. Gómez Cadenas, I. González, G. Gracia Abril, G. Greeniaus, W. Greiner, V. Grichine, A. Grossheim, S. Guatelli, P. Gumplinger, R. Hamatsu, K. Hashimoto, H. Hasui, A. Heikkinen, A. Howard, V. Ivanchenko, A. Johnson, F.W. Jones, J. Kallenbach, N. Kanaya, M. Kawabata, Y. Kawabata, M. Kawaguti, S. Kelner, P. Kent, A. Kimura, T. Kodama, R. Kokoulin, M. Kossov, H. Kurashige, E. Lamanna, T. Lampén, V. Lara, V. Lefebure, F. Lei, M. Liendl, W. Lockman, F. Longo, S. Magni, M. Maire, E. Medernach, K. Minamimoto, P. Mora de Freitas, Y. Morita, K. Murakami, M. Nagamatu, R. Nartallo, P. Nieminen, T. Nishimura, K. Ohtsubo, M. Okamura, S. O'Neale, Y. Oohata, K. Paech, J. Perl, A. Pfeiffer, M.G. Pia, F. Ranjard, A. Rybin, S. Sadilov, E. Di Salvo, G. Santin, T. Sasaki, N. Savvas, Y. Sawada, S. Scherer, S. Sei, V. Sirotenko, D. Smith, N. Starkov, H. Stoecker, J. Sulkimo, M. Takahata, S. Tanaka, E. Tcherniaev, E. Safai Tehrani, M. Tropeano, P. Truscott, H. Uno, L. Urban, P. Urban, M. Verderi, A. Walkden, W. Wander, H. Weber, J.P. Wellisch, T. Wenaus, D.C. Williams, D. Wright, T. Yamada, H. Yoshida, and D. Zschiesche. Geant4a simulation toolkit. *Nuclear Instruments and Methods in Physics Research Section A: Accelerators, Spectrometers, Detectors and Associated Equipment*, 506(3):250 – 303, 2003.

[52] C. Bertulani. private communication.

[53] D.R. Tilley, J.H. Kelley, J.L. Godwin, D.J. Millener, J.E. Purcell, C.G. Sheu, and H.R. Weller. Energy levels of light nuclei. *Nuclear Physics A*, 745(3-4):155–362, December 2004.

[54] R. Charity, K. Mercurio, L. Sobotka, J. Elson, M. Famiano, A. Banu, C. Fu, L. Trache, and R. Tribble. Decay of C10 excited states above the 2p+2α threshold and the contribution from democratic two-proton emission. *Physical Review C*, 75(5):051304, May 2007.

[55] R. J. Charity, T. D. Wiser, K. Mercurio, R. Shane, L. G. Sobotka, A. H. Wuosmaa, A. Banu, L. Trache, and R. E. Tribble. Continuum spectroscopy with a 10C beam: Cluster structure and three-body decay. *Physical Review C*, 80(2):024306, August 2009.

[56] N. Curtis, N. Achouri, N. Ashwood, H. Bohlen, W. Catford, N. Clarke, M. Freer, P. Haigh, B. Laurent, N. Orr, N. Patterson, N. Soić, J. Thomas, and V. Ziman. Breakup reaction study of the Brunnian nucleus C10. *Physical Review C*, 77(2):021301, February 2008.

[57] N. Curtis, N. L. Achouri, N. I. Ashwood, H. G. Bohlen, W. N. Catford, N. M. Clarke, M. Freer, P. J. Haigh, B. Laurent, N. A. Orr, N. P. Patterson, N. Soić, J. S. Thomas, and V. Ziman. Erratum: Breakup reaction study of the Brunnian nucleus 10C [Phys. Rev. C 77, 021301 (2008)]. *Physical Review C*, 82(2):029907, August 2010.

[58] W.R. Leo. *Techniques for Nuclear and Particle Physics Experiments: A How-to Approach*. Springer Berlin Heidelberg, 1994.

[59] https://www.gsi.de/en/start/fair/aufbau_der_fair_beschleunigeranlage.htm.

[60] Technical Proposal for the Design, Construction, Commissioning and Operation of R3B, 2005.

[61] Update of the Technical Proposal for the Design, Construction, Commissioning and Operation of the EXL Project (Exotic nuclei studied in light-ion induced reactions at the NESR storage ring), 2006.

[62] Technical Report for the Design, Construction and Commissioning of the CALIFA Barrel, 2011.

[63] M. Holl. *Ladungsaustauschreaktionen an relativistischen Kohlenstoffkernen und Entwicklung einer Frontend-Elektronik für Silizium-Streifen-Detektoren an FAIR Master-Thesis von Matthias Holl November 2010*. Master thesis, Technische Universität Darmstadt, Germany, 2010.

[64] Gamma Medica-Ideas. *Va32HDR14.2 Documentation*.

[65] Gamma Medica-Ideas. *TA32CG2 Description*.

[66] Gamma Medica-Ideas. *The VA-TA ASIC(s) - principle*.

Acknowledgements

"The Univeral Label", http://xkcd.com/1123. Licensed under CC BY-NC 2.5

On the one hand, the list above is an absolutely correct description of this thesis, as it is a correct description of everything else. On the other hand, it could not be a less accurate description, since it neglects all the small struggles, victories, disappointments and laughs which were part of the creation of this thesis. More importantly it neglects all the the people who helped me in various ways to finish this work and I would like to thank some of them at this point.

First of all, I would like to thank Joachim Enders for giving me the opportunity for writing this thesis and for the many valuable discussions. I thank Haik Simon for his advice and eternal optimism ("Dann wird ja alles gut!"). I also thank Tom Aumann for taking the task of second referee and for his input, especially in the final phase of this thesis.

I am also indebted to a lot of members of the R^3B collaboration, both at GSI and elsewhere, who provided their help in analysing the data through calibrations, explanations and discussions. Trying to name all of them could only lead to failure so I just want to mention two of them. The first one is Ralf Plag for continuously improving the tracker to make the life of those who analyse data easier and for patiently answering the questions of those who feel he hasn't made life easy enough. The second one is Valerii Panin who created a lot of the tools necessary for the analysis of QFS and the discussions with whom I always enjoyed due to his seemingly endless enthusiasm.

I also thank Carlos Bertulani from Texas A&M for providing the theoretical calculations for the (p,2p) and (p,pn) reactions. The development and testing of the PCB boards would not have been possible without the work of Peter Schakel from KVI in Groningen.

I would also like to thank all members of the LAND group at GSI for giving me a desk when I suddenly showed up in the beginning of 2010 and for creating a relaxed yet productive atmosphere in which I enjoyed working a lot. For the latter I especially thank my office mates for several years, Christoph Cäsar, Philipp Schrock and Marcel Heine.

I would like to thank my friends, especially Anna Constantinescu, Paul Görgen, Nico Formanek and Florian Steinberg for walks, talks, runs, beers, barbecues, movies and much more. Finally, I'd like to thank my parents for their everlasting support not only over the last three years.

Curriculum Vitae

Personal Data

Name:	Matthias Holl
Birthdate:	10.06.1986
Birthplace:	Frankfurt am Main
Nationality:	German

Education

1992-1996	Primary School: Grundschule Falkenstein, Königstein im Taunus
1996-2005	Secondary School: Bischof-Neumann-Schule, Königstein im Taunus
2005-2009	Bachelor of Science in Physics Technische Universität Darmstadt
2007-2008	Stay abroad within the Erasmus programme Norwegian University of Science and Technology, Trondheim
05 / 2009	Bachelor Thesis Two-Nucleon Knockout Reactions from ^{11}C at Relativistic Energies Supervising professor: Prof. Dr. Joachim Enders
2009-2010	Master of Science in Physics Technische Universität Darmstadt
11 / 2010	Master Thesis Charge Exchange Induced by Relativistic Carbon Nuclei and Development of Frontend Electronics for Silicon Strip Detectors at FAIR Supervising professor: Prof. Dr. Joachim Enders
since 12 / 2010	PhD student at Technische Universität Darmstadt

Lebenslauf

Persönliche Angaben

Name:	Matthias Holl
Geburtsdatum:	10.06.1986
Geburtsort:	Frankfurt am Main
Staatsangehörigkeit:	Deutsch

Ausbildung

1992-1996	Grundschule Falkenstein, Königstein im Taunus
1996-2005	Bischof-Neumann-Schule, Königstein im Taunus
2005-2009	Bachelor of Science in Physik Technische Universität Darmstadt
2007-2008	Auslandsaufenthalt im Rahmen des Erasmusprogramms Norwegian University of Science and Technology, Trondheim
05 / 2009	Bachelor Thesis Zwei-Nukleonen Knockout-Reaktionen von ^{11}C bei relativistischen Energien Betreuender Professor: Prof. Dr. Joachim Enders
2009-2010	Master of Science in Physik, Technische Universität Darmstadt
11 / 2010	Master Thesis: Ladungsaustauschreaktionen an relativistischen Kohlenstoffkernen und Entwicklung einer Frontend-Elektronik für Silizium-Streifen-Detektoren an FAIR Betreuender Professor: Prof. Dr. Joachim Enders
since 12 / 2010	Promotionsstudent an der Technischen Universität Darmstadt

Erklärung zur Dissertation

Hiermit versichere ich, die vorliegende Dissertation ohne Hilfe Dritter nur mit den angegebenen Quellen und Hilfsmitteln angefertigt zu haben. Alle Stellen, die aus Quellen entnommen wurden, sind als solche kenntlich gemacht. Diese Arbeit hat in gleicher oder ähnlicher Form noch keiner Prüfungsbehörde vorgelegen.

Darmstadt, den 10.2.2014

(Matthias Holl)